POLITECNICO DI MILANO

DEPARTMENT OF AEROSPACE SCIENCE AND TECHNOLOGY

DOCTORAL PROGRAMME IN AEROSPACE ENGINEERING

FINITE ELEMENTS FOR ACTUATION OF COMPOSITE SHELL STRUCTURES THROUGH SHAPE MEMORY ALLOYS

Doctoral Dissertation of:
Daniela Rigamonti

Supervisor:
Prof. Giuseppe Sala
Dr. Elena Villa

Tutor:
Prof. Luca Di Landro

The Chair of the Doctoral Program:
Prof. Luigi Vigevano

XXX Cycle

ABSTRACT

Shape memory alloys (SMA) represent an important class of multi-phase smart materials that have the ability to recover huge deformations. This is source of two main mechanical properties: Pseudoelasticity, which is the intrinsic aptitude to recover deformation dissipating energy through a hysteresis cycle, and Shape Memory, which is the capability of a SMA component to return from a deformed state to its original shape under an applied heating. Thanks to such unique properties – along with high energy to weight ratio, high corrosion resistance and biocompatibility – SMA are proposed as smart components in a wide range of innovative applications in the area of biomedical, robotic, automation, automotive as well as aerospace. Many applications involve Pseudoelasticity to provide constant stress (e.g. the widely used orthodontic wires), to withstand high deformations without damage, or to absorb and dissipate mechanical or thermal energy (so acting as dampers or heat absorbers, respectively). In aerospace field, most applications are based on Shape Memory involving the use of SMA as components in smart systems, especially for *actuation* purpose.

The increasing number of SMA-based applications and the consequent growing involvement of industrial players in the field have motivated researchers to formulate *constitutive models* able to catch the complex thermo-mechanical behavior of these materials and to develop robust computational tools for advanced design purposes. However, such a research field is still under progress, especially in the prediction of several important effects characterizing SMA. One of these effects is the change in the transformation behavior with increasing number of cycles, which leads to reduced performance in terms of recoverable deformation, generated force and mechanical hysteresis. This effect is named *functional fatigue*, which differs conceptually from conventional metals fatigue that is still present in SMA, and the development of a technique to design reliable components against this effect is still an open subject in scientific literature. Another effect that is still an open issue in constitutive modeling research is the simulation of different *microstructural conditions*. The macroscopic properties of SMA can be widely tailored changing the material microstructure through proper actions (chemical alloy composition changes or specific thermal and mechanical treatments), but the influence of microstructural aspects as modeling parameters can be considered through very different solutions.

Motivated by the described framework, the thesis is dedicated to introduce the functional fatigue or microstructural changes as the reduction of performance for an actuator into a design tool such as a finite element model.

Concerning the *constitutive modeling*, the present thesis proposes to start from an already robust model to implement modifications that allow evaluating the two effects of functional fatigue and microstructural conditions. *Numerical implementation* is going to be pursued using commercial

software commonly used by engineers to design SMA actuators. This choice is driven by the aim of being effective in exploiting the model for practical purposes.

Since several approaches to constitutive modeling of SMA exist and each of them can have useful features, the thesis starts with introducing a critical analysis of three constitutive approaches for SMA in order to investigate the different models available and select the most suitable to be implemented with the new approach proposed.

The constitutive and numerical modeling activities are completed by *experimental characterization* of NiTi SMA. Indeed, the design of SMA components is strictly related to the knowledge of their metallurgical aspects and the experimental characterization is not only devoted to model calibration, but is an indispensable means to understand the mechanisms driving the transformation and thus also determine the functional properties of the component that is under design. Moreover, the comparison between numerical predictions and experimental data allows quantitatively validating the proposed modifications to the constitutive model.

Finally, regarding the *aerospace smart system application*, the thesis focuses on the use of SMA actuators for the design of morphing skins based on corrugated shell geometries applied to composite materials.

Keywords: shape memory alloys, constitutive modeling, experimental characterization, functional fatigue, aerospace applications, smart systems, shell composite structures, SMA actuators

THESIS ORGANIZATION

The thesis is divided into six chapters.

Chapter 1 is devoted to a brief dissertation on the fundamental concepts regarding SMA and on the research background concerning the key aspects investigated in the thesis by recalling the historical background, material properties, and applications. In the same chapter, also a literature review on shape memory alloy constitutive modeling is presented, in order to prepare the framework for the following study.

Then, motivated by the need to select an already developed constitutive model that serves as a robust basis for the proposed modifications, Chapter 2 describes in detail three constitutive models. The first model selected is based on (Tanaka, 1986), modified using a sigmoidal function as transformation kinetics law; the second model considered is the well-known (Boyd and Lagoudas, 1996) macroscopic free energy model; the last model is also a free-energy model developed by Müller and Seelecke (2001). These models are analyzed and then verified on the experimental results of a uniaxial tensile test.

Chapter 3 formalize a qualitative comparison between the same models presented in previous chapter but basing on more complex applications object of research both in ICMATE research unit of National Research Council and in DAST department of Polytechnic University of Milan. This comparison leads to the selection of the third model as a constitutive basis, in the following referred with the acronym MAS.

Chapter 4 presents an experimental characterization of a typical SMA commercial wire for actuation, with the aim to calibrate some fundamental parameters of the MAS model. A detailed description an analysis is presented to define also to the recommended procedures for thermomechanical characterization.

The experimental characterization is completed in Chapter 5 through the measurement of the transformation-triggering stress as a function of the fractional volume of martensite in different microstructural conditions. This is obtained thanks to in situ X-ray diffraction experiment performed during mechanical cycling. Such experiments allow investigating the effects of microstructural changes on the stress-induced phase transition mechanism in polycrystalline NiTi. The chapter concludes with the proposed modification to the formulation of the MAS model to include functional fatigue aspects.

Finally, the results obtained in Chapter 5 are used to simulate an aerospace application in Chapter 6. The application consists in the use of SMA as actuators for an aerodynamic morphing skin based on corrugated shell geometries made by composite materials and it is simulated in two conditions of the wire one representing the properties at begin of life and the other after some cycles of shape modification.

TABLE OF CONTENTS

SYMBOLS AND ABBREVIATIONS

2.1 List of Symbols

ξ	Volumetric fraction
σ	Stress
ε	Strain
T	Temperature
E	Elastic modulus

2.2 List of Abbreviations

SMA, SMAs	Shape Memory Alloy, –s
A, M, R	Austenite, Martensite, Rhombohedral phases
X→Y	Transformation from phase X to phase Y
Rcs, Rcf	Start and finish temperatures of rhombohedral direct transformation (A→R)
Ms, Mf	Start and finish temperatures of martensitic transformation (A/R →M)
Rhs, Rhf	Start and finish temperatures of rhombohedral reverse transformation (M→R)
As, Af	Start and finish temperatures of austenitic transformation (M/R →A)
PE	Pseudoelasticity
SME	Shape Memory Effect
TT	Thermal Treatment

Chapter 1
INTRODUCTION

1.1 Background and motivations

Shape memory alloys (SMAs) belong to a class of smart materials exhibiting very interesting and peculiar properties (Thermoelastic martensitic transformation, shape memory effect, pseudo elasticity, high corrosion resistance, and biocompatibility) that have enabled them to find many engineering applications. In particular, a most widely explored application for SMAs is that of *smart actuators* that provides an excellent technological opportunity to replace conventional actuators such as electrical, pneumatic and hydraulic. Due to their unique properties and their ability to react directly to environmental stimuli, SMAs can lead to simple devices with a significant reduction in mechanical complexity and size and an improved reliability of the system. Furthermore, in case of mini/micro devices, high power-to-weight ratio and low driving voltages are added to these benefits. Another interesting possibility is the employ of SMAs in microgravity condition, using them as *pseudoelastic components* for mechanical damping, via the conversion of the work absorbed in each cycle thanks to its hysteresis loop or via the changing of the resonance frequencies by activation of SMA elements or even using the intrinsic dissipation of mechanical energy of the martensite microstructure. All these aspects make SMAs ideal materials for applications where there is need for high stress-strain rate, union of features of self-sensing and self-actuation, fine calibration of actuation and low frequencies, for example in the fields of application such as biomedical, aerospace, micro-electronics, robotic and automotive.

Focusing on the aerospace filed, since the success of the SMA coupling for hydraulic lines in the F-14 fighter jets in the 1970s (Melton, 1998), the unique properties of SMAs have gathered greater interest in aerospace applications, which are subjected to high dynamic loads and geometric space constraints. Few examples of these applications are actuators, structural connectors, vibration dampers, sealers and valves, release or deployment mechanisms, inflatable structures,

manipulators. In the 1990s, aerospace researchers focused on active structures with morphing capability, intended to be adaptive structures with system–level optimization under various flight conditions. Leading the way in morphing wing technology was the Defense Advanced Research Projects Agency (DARPA) program for aircraft 'smart wings', that addressed the development and demonstration of smart material–based concepts to improve the aerodynamic and aeroelastic performances of military aircraft (Kudva, 2004). The second of the most known fixed–wing projects of the past is the Smart Aircraft and Marine Propulsion System Demonstration (SAMPSON) program for jet engines, that was designed to demonstrate the usefulness of active materials in tailoring the inlet geometry and orientation of various propulsion systems (Pitt et al., 2001). Boeing has developed an active serrated aerodynamic device with SMA actuators, which is also known as a variable geometry chevron (VGC) and has been installed on the jet engine of the Boeing 777-300 ER commercial aircraft. This device has proven to be very effective in reducing noise during take-off by maximizing the chevron deflection, and also increasing the cruise efficiency by minimizing the chevron deflection during the flight (Hartl et al., 2010). Following, a huge number of other programs and research lines arose, focusing on different types of structural components and many of them have been also patented, such as a telescopic wing system (Knowles and Bird, 2004), a retractable landing gear (Kutlucinar, 2005), a deployable flap edge fence (Larssen and Calkins, 2010), a SMA actuator coupled between an airfoil and a deployable device (Mabe et al., 2011), jet engine components (Song and Ma, 2012; Wood and Dunne, 2012) and high stiffness aero-structures (Richard D. Widdle et al., 2013).

There has also been significant research in rotor technology (rotorcraft) with SMAs conducted by several researchers, including rotor blade actuators, rotor blade twisting, and rotor blade tip morphing (Kennedy et al., 2004; Prahlad and Chopra, 2001; Singh et al., 2003; Testa et al., 2005).

SMAs have been used for many years in spacecraft as low-shock release mechanisms, because they can be actuated slowly by gradual heating, they can efficiently absorb vibration and can be integrated in simple and compact designs, which are most suitable for small sized spacecraft (i.e. mini-micro actuator for microsatellite). A few samples of small devices with SMA are the QWKNUT (Peffer et al., 2000), Frangibolt® (Johnson, 1992), Micro-Sep-Nut (Willey et al., 2001), and Rotary Latch (Bokaie et al., 1998).

As mentioned earlier, SMAs are suitable for vibration damper/isolator applications due to their unique behavior. Considerable new research has been performed to study this in detail, and a few patents have been filed to exploit these advantages.

From these examples, it is evident that the most part of innovation proposed in aerospace field is related to the use of SMA in actuator devices. Through this, shape memory effect actuation is commonly applied to the problem of adaptable morphing of the wing structure. The reviews of (Barbarino et al., 2014, 2011) and (Sofla et al., 2010) have presented a large number of morphing solutions, which have been classified according to the type of shape variation they are designed to accomplish. A variable-sweep wing controlled by SMA ribbons on the spar has been

investigated by (Galantai et al., 2012). In several other studies, SMA wire was used to create a morphing trailing edge to enhance lift (Kang et al., 2012; Karagiannis et al., 2014; Ko et al., 2014). Several segmented morphing trailing-edge concepts, which produce a larger trailing-edge angle, have been investigated (Ameduri et al., 2012; Wang et al., 2013). A similar approach can be used in the leading edge to increase the lift-to-drag ratio (Abdullah et al., 2011). Cornell University designed a Hyper-Elliptic Cambered Span (HECS) wing using SMA actuators (Manzo et al., 2005). This morphing wingtip can markedly improve maneuverability by enhancing yaw control while in the furled state. (Strelec et al., 2003) carried on a global optimization study incorporating a coupled structural, thermal ad aerodynamic analysis to determine the necessary placement of the SMA wire actuators within a compliant wing. (Icardi and Ferrero, 2009) designed morphing wing with SMA torsion tubes and SMA wires for camber variation. The application studied in the present work relies in this category too, since it is focused on the analysis of composite shell structures designed for adaptive variation of the geometry of aerodynamic surfaces.

Until 2014, over 20,000 worldwide patents, more than 10,000 of them in the United States, have been issued on SMAs applications (Mohd Jani et al., 2014). Nonetheless, the percentage of commercially successful SMA applications is still low and the realization of viable products from all this intellectual property has thus far been limited. Many promising areas and topics of research have been proposed on SMAs, among which the mainstream of the research is focused on the metallurgical properties. The rather complex thermo-mechanical interactions and microstructural behavior of shape memory alloys can present serious difficulties to the engineer interested in turning a novel device, e.g. a new smart actuator with SMA component, into a product with longevity, reliability and repeatability suitable for commercial use. The main design instruments for SMA actuators are: (1) find simplified design methods to guide the engineer in dimensioning the actuator and (2) obtain a simple and reliable material model that can be integrated in an efficient continuum model and computational tool such as finite element method.

To make an efficient use of these novel applications resulting from research on SMA and successfully improve their design, it is necessary to model the complex, non-linear hysteretic and thermo-mechanically coupled material behavior of SMA. In this context, FE modeling could play a key role to speed up the development process, especially for preliminary studies and validations of high risk and/or expensive projects. The importance of incorporating modern computer design and analysis tools such as finite element into developing innovative and reliable SMA applications has led to an interest in more accurate constitutive models. A large number of constitutive models have been developed. In this context, this PhD project concerns the improvement of a numerical tool (i.e. a material constitutive model) for the design of actuation devices based on shape memory alloys (SMAs), to facilitate their industrial transfer and large-scale applicability.

A large number of SMAs have been discovered since the mid-1900s to late 1900s, and the list continues to grow. Many of these alloys, while scientifically interesting, consist of precious metals

or only exhibit useful properties as single crystals, which do not lend them to practical use in commercial applications. A few alloys, however, have emerged as commercially viable for novel devices. These include certain copper alloys (CuAlZn and CuAlNi) and nickel–titanium–based alloys, such as near–equiatomic NiTi, known as Nitinol (first discovered in the early 1960s) and some ternary alloys such as NiTiCu and NiTiNb. To date, it is fair to say that NiTi-based SMAs have the best memory and superelasticity properties of all the known polycrystalline SMAs. The NiTi family of alloys can withstand large stresses and can recover strains near 8% for low cycle use or up to about 2.5 % strain for high cycle use. This strain recovery capability can enable the design of novel devices in either a thermally active mode or an isothermal energy absorption mode. NiTi SMAs have other advantages in terms of corrosion resistance, fatigue resistance, and biocompatibility, thereby making them the preferred material system for most SMA applications being considered today. (Shaw et al., 2008) For this reason, in the present work the focus will be always on NiTi samples.

All SMA properties (in particular shape memory effect and superelasticity) arise from the reversible thermoelastic martensitic transformation between two solid phases. The parent phase stable at high temperature is called austenite, which has a high-symmetry crystal structure usually based on a cubic lattice. The product phase stable at low temperature is called martensite, which has a crystal structure with lower symmetry, such as tetragonal, rhombohedral, orthorhombic, monoclinic, or triclinic, depending on the particular alloy. In Nitinol (near-equiatomic NiTi), the austenite has an ordered B2 crystal structure, which can be viewed as two interpenetrating simple cubic lattices of Ni and Ti, respectively. (It is often incorrectly called a bodycentered cubic structure, which would only be accurate if the material were monoatomic.) The martensite has an ordered B19’ crystal structure, where B19 denotes an orthorhombic structure resulting from unequal normal strains relative to the (110) directions of the austenite structure, and the prime (’) indicates that it has additionally been distorted by a shear strain, resulting in monoclinic symmetry. Another intermediate phase that often appears is called the R phase, which is a rhombohedral distortion of the B2 structure. Since the crystal lattice of martensite has a lower symmetry, 24 orientations called variants can coexist: in a state without load, all of them are present. The transformation is based on a twinning-detwinning accommodation process, which allows the reversibility.

The design of SMA components is strictly related to the knowledge of the metallurgic aspects of this class of materials. In fact, the actuation action is driven by the martensitic transformation and the consequent variation of the macroscopic mechanical properties when the temperature changes. The intrinsic thermomechanical properties of the material can be tuned by means of thermomechanical processes (preliminary treatments, stabilizing training or lifelong cycling), and then this determines the actuator performance. The comprehension of the functional properties of these classes of materials is related to material science, but the design of the SMA

components is mostly related to engineering aspects, such as how much is the maximum work that a SMA actuator can perform in terms of maximum force and stroke, and in which temperature range it is able to achieve that force/stroke (Stortiero, 2014). To design SMA applications, closer collaboration between material scientists and engineering designers is essential: the challenges in designing SMA actuators are related not only to the materials limitations, but also to the success in conveying effectively the information between these two groups.

Consequently to the statement above, the importance of a reliable characterization the thermomechanical properties of the SMA is easy understandable. In this PhD work, the activities performed at CNR-ICMATE were mainly focused on the material characterization and the deepening of the understanding of the material. Both this aspects are critical elements for the development of a computational tool able to reproduce the behavior of such a complex material. Different techniques have been used and will be reported focusing on the characteristics useful for the material modelling.

Thinking of a future growing use of SMA components in different engineering applications, the issue of material performance (e.g. changes in its properties) resulting from an application of cyclic loads over its designed life (i.e. functional fatigue) is of great concern to product engineering. The fatigue life of the semi-finished product is commonly guaranteed, but in the case of a specific application, the working conditions affect significantly the performance of the SMA, then the functional fatigue may not coincide with the structural one, requiring a case-by-case basis evaluation. The operational guarantee can be given only if the fundamental aspects specific to the application are evaluated. Then, the target of the PhD project is the improvement of a constitutive model to take into account the functional fatigue of a SMA actuator and the prediction through modeling of the performances during its life.

1.2 Constitutive and numerical modeling of shape memory alloys

Then, the approach is to start from an already robust model that is adequate to take into consideration this aspect. To select this model, a literature review on shape memory alloy constitutive modeling is needed and is presented in this chapter. A very large number of models exist for a variety of purposes, among which can be distinguished between:

1) Understand the underlying physics and mechanisms that cause the observed effects (explanation of the observed phenomena).
2) Identify the material properties or processing parameters that can yield desired effects in terms of SME, SE and other functional properties (material development).
3) Predict the material response in conjunction with the smart device or the system that is under investigation (application development).

Linked to this distinction, there is the most diffused categorization of the constitutive models of SMAs is the one that distinguishes between the dimension of the physical domain.

The first aim (understand the underlying physics and mechanisms) can be fulfilled with micromechanical models, which start from the crystallographic modelling of a single crystal. Then, the polycrystalline response of the SMA can be obtained averaging the results over a representative volume element. The advantage of the microscopic approach is the ability to predict the material response with high precision and sophistication; however, the high computational cost required is an important drawback that reduces their application for modelling structural response.

As an example, one of these models was presented by (Patoor et al., 1988). In the early model, a simplified interaction matrix was used to formulate the interaction energy and an averaging scheme was subsequently invoked to model the polycrystalline behavior. This model can describe SE; however, the simplified form of interaction energy chosen prevents it from modeling temperature induced transformation.

The other two purposes (material development and application development) are consequence of the spread in the applications of SMA and of the resulting need of a design-tool. Then, they lead to models having the advantage of being easily integrated into existing structural modelling system based, for example, on the finite element method. For this reason, models at macroscopic domain are the most suitable. These models are mainly divided in two categories: phenomenological and thermodynamic. Phenomenological models draw heavily on the observed exhibition of the functional properties of the material and are suitable for engineering practice, because they make use of measurable quantities as parameters and are often relatively simple. Thermodynamic models are based on the free energy description of the material behavior and then rely on more sophisticated mathematical formulations.

In the field of the model based on a phenomenological approach, one of the first is (Tanaka, 1986; Tanaka and Nagaki, 1982). It uses the fraction of martensite as an internal variable and gives a phenomenological equation of state for its dependence on stress and temperature in the form of an exponential function. It is a clear example of the use of stress-temperature phase diagram based on the stress–influence (Clausius–Clapeyron) coefficients to identify appropriate transformation bands. Based on this approach, many other models have been developed modifying the form of the state equation. Most remarkable examples are (Liang and Rogers, 1997), who used a cosine law for the martensite fraction, and (Brinson, 1993), who used a cosine law too and who is credited with having first introduced a decomposition of the martensite fraction between stress-induced (detwinned) martensite and temperature-induced (twinned) martensite. Indeed, the major shortcoming of both Tanaka and Liang and Rogers models is that they can only be applicable to the high temperature case of pseudoelasticity (from austenite to martensite), while Brinson describes as well the pseudoplastic behavior (shape memory effect, i.e. detwinning of martensite) at lower temperatures.

Remaining in the field of phenomenological models, a more consistent thermodynamic description relates the rate of entropy production to the growth rate of martensite fraction, rather than to the fraction itself. Thus, some models assume a functional form for the kinetics in the rate form of martensite fraction that is a generalization from the notion of flow rule in rate independent plasticity. (Lubliner and Auricchio, 1996) present a generalized plasticity based model for single variant transformation, capable of simulating PE. (Auricchio and Lubliner, 1997) extended this by considering two internal variables representing multi-variant (similar to twinned martensite) and single variant (similar to stress-induced) martensite. (Auricchio and Taylor, 1997) consider multi-axial state of stress through several case studies for superelastic response. To facilitate the implementation of this constitutive model in a displacement based finite-element approach, (Auricchio and Sacco, 1999) give a strain based flow-rule with linear kinetics. (Auricchio et al., 2014) developed a refined and general three-dimensional phenomenological constitutive model following what introduced by (Auricchio and Bonetti, 2013) in a more theoretical context, taking into account several physical phenomena.

Further, to account for stress multi-axiality, (Brocca et al., 2002) proposed a model based on the habit plane or microplane theory. Using the notion of microplanes at a macroscopic level, they deduce a form for macroscopic transformation strain due to 3-D loading employing a modified 3-D transformation onset criteria.

Phenomenological models probably are the most popular in the literature, due to their approach that allows easy developments without considering the underlying physics of the transformation kinetic.

Martensitic transformation can be defined using appropriate free-energy function and additional thermodynamic notions for dissipative processes. In this approach, a more consistent attempt is

made to identify a suitable form of free energy or potential that represents the state of the system and introduce the phase transformation related effects through either the changes in free energy itself or generalized constitutive function like dissipation potential. The choice of field or state variables determines the type of free energy like, Gibbs, Helmholtz, or phenomenological Landau-Devonshire forms.

Using the "maximum dissipation postulate" of classical plasticity, an analogy between the dissipation potential and the rate-independent yield function can be established. Macroscopic free energy models inspired from plasticity utilize this fact. (Boyd and Lagoudas, 1996), (Bo and Lagoudas, 1999), (Qidwai and Lagoudas, 2000) were one of the first to propose and utilize this idea. (Auricchio and Petrini, 2002) have used a generalized solution algorithm for thermomechanically coupled Boundary Value Problem and have further extended this approach to solve a coupled thermomechanical problem on SMA based hybrid composites.

(Achenbach and Müller, 1982) had derived a form for free energy based on statistical thermodynamics ideas and on the theory of thermally activated processes. (Huo and Müller, 1993) were one of the first to discuss the importance of dissipative processes and use the notion of dissipation potential to describe the kinetics in SMAs. Building on these works, (Müller and Seelecke, 2001) postulate that the interfacial energy arising out of coherency mismatch is responsible for the hysteresis. It has been shown that the model is able to simulate qualitatively the behavior of SMAs over the whole range of temperatures (both PE and SME). Through the introduction of the Helmholtz free energy as the effective potential energy, (Seelecke and Müller, 2004) has been able to make quantitative predictions.

The reader is referred also to (Cisse et al., 2016), (Khandelwal and Buravalla, 2009), (Lagoudas et al., 2006), (Bernardini and Pence, 2002)for an overview on shape memory alloy modeling.

References

Abdullah E.J., Bil C., Watkins S., 2011. Performance of Adaptive Airfoil Control System Using Shape Memory Alloy Actuators for UAV, in: AIAA Aviation Technology, Integration and Operations Conference. pp. 1–12. doi:10.2514/6.2011-6849

Achenbach M., Müller I., 1982. A model for shape memory. J. Phys. Colloq. 43, C4--163-C4--167. doi:10.1051/jphyscol:1982418

Ameduri S., Brindisi A., Tiseo B., Concilio A., Pecora R., 2012. Optimization and integration of shape memory alloy (SMA)-based elastic actuators within a morphing flap architecture. J. Intell. Mater. Syst. Struct. 23, 381–396. doi:10.1177/1045389X11428672

Auricchio F., Bonetti E., 2013. A new "flexible" 3D macroscopic model for shape memory alloys. Discret. Contin. Dyn. Syst. - Ser. S 6, 277–291. doi:10.3934/dcdss.2013.6.277

Auricchio F., Bonetti E., Scalet G., Ubertini F., 2014. Theoretical and numerical modeling of shape memory alloys accounting for multiple phase transformations and martensite reorientation. Int. J. Plast. 59, 30–54. doi:10.1016/j.ijplas.2014.03.008

Auricchio F., Lubliner J., 1997. A uniaxial model for shape-memory alloys. Int. J. Solids Struct. 34, 3601–3618. doi:10.1016/S0020-7683(96)00232-6

Auricchio F., Petrini L., 2002. Improvements and algorithmical considerations on a recent three-dimensional model describing stress-induced solid phase transformations. Int. J. Numer. Methods Eng. 55, 1255–1284. doi:10.1002/nme.619

Auricchio F., Sacco E., 1999. A temperature-dependent beam for shape-memory alloys: Constitutive modelling, finite-element implementation and numerical simulations. Comput. Methods Appl. Mech. Eng. 174, 171–190. doi:10.1016/S0045-7825(98)00285-0

Auricchio F., Taylor R.L., 1997. Shape-memory alloys: modelling and numerical simulations of the finite-strain superelastic behavior. Comput. Methods Appl. Mech. Eng. 143, 175–194. doi:10.1016/S0045-7825(96)01147-4

Barbarino S., Bilgen O., Ajaj R.M., Friswell M.I., Inman D.J., 2011. A Review of Morphing Aircraft. J. Intell. Mater. Syst. Struct. 22, 823–877. doi:10.1177/1045389X11414084

Barbarino S., Saavedra Flores E.I., Ajaj R.M., Dayyani I., Friswell M.I., 2014. A review on shape memory alloys with applications to morphing aircraft. Smart Mater. Struct. 23, 63001. doi:10.1088/0964-1726/23/6/063001

Bernardini D., Pence T.J., 2002. Models for one-variant shape memory materials based on dissipation functions. Int. J. Non. Linear. Mech. 37, 1299–1317. doi:10.1016/S0020-7462(02)00020-3

Bo Z., Lagoudas D.C., 1999. Thermomechanical modeling of polycristaline SMAs under cyclic loading, Part I: theroretical derivations. Int. J. Eng. Sci. 37, 1089–1140.

Bokaie M.D., Busch J.D., Johnson A.D., Petty B., 1998. Release device for retaining pin.

Boyd J.G., Lagoudas D.C., 1996. A thermodynamical constitutive model for shape memory materials. 1: The monolithic shape memory alloy. Int. J. Plast. 12, 805–842.

Brinson L.C., 1993. Dimensional Constitutive Behavior of Shape Memory Alloys: Thermomechanical Derivation With Non-Constant Material Functions and Redefined Martensite Internal Variable. J. Intell. Mater. Syst. Struct. 4, 229–242. doi:10.1177/1045389X9300400213

Brocca M., Brinson L.C., Bazant Z.P., 2002. Three-dimensional constitutive model for shape memory alloys based on microplane model. Philos. Mag. A 82, 1051–1078.

Cisse C., Zaki W., Zineb T. Ben, 2016. A review of modeling techniques for advanced effects in shape memory alloy behavior. Smart Mater. Struct. 25, 103001. doi:10.1088/0964-1726/25/10/103001

Galantai V.P., Sofla A.Y.N., Meguid S.A., Tan K.T., Yeo W.K., 2012. Bio-inspired wing morphing for unmanned aerial vehicles using intelligent materials. Int. J. Mech. Mater. Des. 8, 71–79. doi:10.1007/s10999-011-9176-0

Hartl D.J., Lagoudas D.C., Calkins F.T., Mabe J.H., 2010. Use of a Ni60Ti shape memory alloy for active jet engine chevron application: I. Thermomechanical characterization. Smart Mater. Struct. 19, 15020. doi:10.1088/0964-1726/19/1/015020

Huo Y., Müller I., 1993. Nonequilibrium thermodynamics of pseudoelasticity. Contin. Mech. Thermodyn. 5, 163–204. doi:10.1007/BF01126524

Icardi U., Ferrero L., 2009. Preliminary study of an adaptive wing with shape memory alloy torsion actuators. Mater. Des. 30, 4200–4210. doi:10.1016/j.matdes.2009.04.045

Johnson A.D., 1992. Non-explosive separation device.

Kang W., Kim E., Jeong M., Lee I., 2012. Morphing Wing Mechanism Using an SMA Wire Actuator. Int. J. Aeronaut. Sp. Sci. 13, 58–63. doi:10.5139/IJASS.2012.13.1.58

Karagiannis D., Stamatelos D., Spathopoulos T., Solomou A., Machairas T., Chrysohoidis N., Saravanos D., Kappatos V., 2014. Airfoil morphing based on SMA actuation technology. Aircr. Eng. Aerosp. Technol. 86, 295–306. doi:10.1108/AEAT-10-2012-0194

Kennedy D.K., Straub F.K., Schetky L.M., Chaudhry Z., Roznoy R., 2004. Development of an SMA Actuator for In-flight Rotor Blade Tracking. J. Intell. Mater. Syst. Struct. 15, 235–248. doi:10.1177/1045389X04042794

Khandelwal A., Buravalla V., 2009. Models for Shape Memory Alloy Behavior: An overview of modeling approaches. Int. J. Struct. Chang. Solids 1, 111–148.

Knowles G., Bird R.W., 2004. Telescopic wing system. US Pat. 6834835B1.

Ko S.-H., Bae J.-S., Rho J.-H., 2014. Development of a morphing flap using shape memory alloy actuators: the aerodynamic characteristics of a morphing flap. Smart Mater. Struct. 23, 74015. doi:10.1088/0964-1726/23/7/074015

Kudva J.N., 2004. Overview of the DARPA Smart Wing Project. J. Intell. Mater. Syst. Struct. 15, 261–267. doi:10.1177/1045389X04042796

Kutlucinar I., 2005. Aircraft with shape memory alloys for retractable landing gear. US Pat. 6938416B1.

Lagoudas D.C., Entchev P.B., Popov P., Patoor E., Brinson L.C., Gao X., 2006. Shape memory alloys. 2: Modeling of polycrystals. Mech. Mater. 38, 430–462.

Larssen J. V, Calkins F.T., 2010. Deployable Flap Edge Fence. US Patents 2010/0219288A1.

Liang C., Rogers C.A., 1997. One-Dimensional Thermomechanical Constitutive Relations for Shape Memory Materials. J. Intell. Mater. Syst. Struct. 8, 285–302. doi:10.1177/1045389X9700800402

Lubliner J., Auricchio F., 1996. Generalized plasticity and shape memory alloys. Int. J. Solids Struct. 33, 991–1003. doi:10.1016/0020-7683(95)00082-8

Mabe J.H., Calkins F.T., Bushnell G.S., Bieniawski S.R., 2011. Aircraft systems with shape memory alloy (SMA) actuators, and associated methods. US Pat. 7878459B2.

Manzo J., Garcia E., Wickenheiser A., Horner G.C., 2005. Design of a shape-memory alloy actuated macro-scale morphing aircraft mechanism, in: SPIE 5764, Smart Structures and Materials 2005: Smart Structures and Integrated Systems. pp. 232–240. doi:10.1117/12.601372

Melton K.N., 1998. General applications of SMA's and smart materials, in: Otsuka, K., Wayman, C.M. (Eds.), Shape Memory Materials. Cambridge University Press, pp. 220–239.

Mohd Jani J., Leary M., Subic A., Gibson M.A., 2014. A review of shape memory alloy research, applications and opportunities. Mater. Des. 56, 1078–1113. doi:10.1016/j.matdes.2013.11.084

Müller I., Seelecke S., 2001. Thermodynamic aspects of shape memory alloys. Math. Comput. Model. 34, 1307–1355.

Patoor E., Eberhardt A., Berveiller M., 1988. Thermomechanical behaviour of shape memory alloys. Arch. Mech. 40, 775–794.

Peffer A., Denoyer K., Fosness E., Sciulli D., 2000. Development and transition of low-shock spacecraft release devices, in: IEEE Aerospace Conference Proceedings. pp. 277–284.

doi:10.1109/AERO.2000.878439

Pitt D.M., Dunne J., White E., Garcia E., 2001. SAMPSON Smart Inlet SMA Powered Adaptive Lip Design and Static Test. Proc. 42nd AIAA Struct. Structrual Dyn. Mater. Conf. Seattle, WA, 16-20 April 2001 1–11. doi:10.2514/6.2001-1359

Prahlad H., Chopra I., 2001. Design of a variable twist tiltrotor blade using shape memory alloy (SMA) actuators. Proc. SPIE - Int. Soc. Opt. Eng. 4327, 46–59. doi:10.1117/12.436559

Qidwai M. a, Lagoudas D.C., 2000. Numerical implementation of a shape memory alloy thermomechanical constitutive model using return mapping algorithms. Int. J. Numer. Methods Eng. 47, 1123–1168. doi:10.1007/978-0-387-47685-8

Richard D. Widdle J., Grimshaw M.T., Crosson-Elturan K.S., Mabe J.H., Calkins F.T., Gravatt L.M., Shome M., Us I.N., Mabe J.H., 2013. High stiffness shape memory alloy actuated aerostructure.

Seelecke S., Müller I., 2004. Shape memory alloy actuators in smart structures: Modeling and simulation. Appl. Mech. Rev. 57, 23. doi:10.1115/1.1584064

Shaw J.A., Churchill C.B., Iadicola M.A., 2008. TIPS AND TRICKS FOR CHARACTERIZING SHAPE MEMORY ALLOY WIRE: PART 1—DIFFERENTIAL SCANNING CALORIMETRY AND BASIC PHENOMENA. Exp. Tech. 32, 55–62. doi:10.1111/j.1747-1567.2008.00410.x

Singh K., Sirohi J., Chopra I., 2003. An Improved Shape Memory Alloy Actuator for Rotor Blade Tracking, in: Journal of Intelligent Material Systems and Structures. pp. 767–786. doi:10.1177/104538903039134

Sofla A.Y.N., Meguid S.A., Tan K.T., Yeo W.K., 2010. Shape Morphing of Aircraft Wings: Status and challenges. Mater. Des. doi:10.1016/j.matdes.2009.09.011

Song G., Ma N., 2012. Shape memory alloy actuated adaptive exhaust nozzle for jet engine. US Patents 8245516.

Stortiero F., 2014. Design and Industrial Manufacturing of SMA Components, in: Shape Memory Alloy Engineering: For Aerospace, Structural and Biomedical Applications. pp. 215–244. doi:10.1016/B978-0-08-099920-3.00008-5

Strelec J.K.J.J.K., Lagoudas D.C.D., Khan M.M.A., Yen J., 2003. Design and Implementation of a Shape Memory Alloy Actuated Reconfigurable Airfoil. J. Intell. Mater. Syst. Struct. 14, 257–273. doi:10.1177/104538903034687

Tanaka K., 1986. Thermomechanical Sketch of Shape Memory Effect: One-Dimensional Tensile Behavior. Res Mech. Int. J. Struct. Mech. Mater. Sci. 18, 251–263.

Tanaka K., Nagaki S., 1982. A thermomechanical description of materials with internal variables in the process of phase transitions. Ingenieur-Archiv 51, 287–299. doi:10.1007/BF00536655

Testa C., Leone S., Ameduri S., Concilio A., 2005. Feasibility study on rotorcraft blade morphing in hovering 5764, 171–182. doi:10.1117/12.600975

Wang Q., Xu Z., Zhu Q., 2013. Structural design of morphing trailing edge actuated by SMA. Front. Mech. Eng. 8, 268–275. doi:10.1007/s11465-013-0261-y

Willey C., Huettl B., Hill S., 2001. Design and Development of a Miniature Mechanisms Tool-Kit for Micro Spacecraft, in: Proceedings of the 35{th} Aerospace Mechanisms Symposium, Ames Research Center, 9-11 May. pp. 1–14.

Wood J.H., Dunne J.P., 2012. Morphing Structure and Method. US8397485.

Chapter 2
COMPARISON OF THREE SIMULATION METHODS

Metal fatigue generally refers to the progressive and localized structural damage that manifests with microscopic cracks forming at the stress concentrators (e.g. surface, slip bands or grain interfaces) when a material is subjected to cyclic loading. Eventually, when a micro–crack reaches a critical size, it suddenly propagates causing the fracture of the structure. In SMA, a different type of fatigue can be defined in addition to the conventional one for metals. Functional fatigue arise from the application of cyclic loads (thermal and/or mechanical) that introduces microstructural defects that change material performance (e.g. expected stroke, force and mechanical hysteresis). This leads to the classical change in the shape of the hysteresis cycle that passes from a so-called "flag–shape", to a more narrow profile that can be named "leaf–shape". This type of hysteresis cycle can be obtainable in SMA also if treated at low temperature, revealing that different

materials can have very different initial behaviors and so responses to fatigue life. NiTi derives its unique mechanical behavior from the coordinated atomic movements manifesting in the phase transformations from the cubic austenite to monoclinic martensite. Therefore, any significant alignment of the atomic planes attributed to crystallographic grain orientation distribution (crystallographic texture) or microstructural defects (slips or precipitates) or grain boundary distribution (grain size) in the polycrystalline material can have a marked influence on the mechanical response of the material.

The interest here is focused on the computational consideration of the effect of these microstructural aspects – namely individual microstructural defects, crystallographic texture and grain size – on mechanical and fatigue behavior with application to NiTi actuation devices. Then, a qualitative comparison between some models is useful to select the model from which start to introduce these characteristics.

Most morphing applications make use of thin wires that, despite developing a lower strength, allow for faster action and lower energy consumption. For this type of component, which mainly works in uniaxial tensile configuration, a one-dimensional model is actually sufficient to represent the macroscopic action of the actuator, so this was not a selection condition.

Three interesting models were identified for their different peculiarities (see also Chapter 1).

Phenomenological models based on the phase diagram are among the most popular in the literature, due to their approach that allows easy developments. For this reason, the first model selected is based on (Tanaka, 1986) and modified using a sigmoidal function as transformation kinetics law (Zhu and Zhang, 2007). It has been further adapted in (Rigamonti et al., 2017) and its differential formulation has been implemented in Matlab. This model result very flexible and easy to implement but limited in actual applications since it is limited to a mono-dimensional problem and has the same drawback of the Tanaka model of being actually restricted to the stress-induced martensite phase transformation only.

The second model considered is the (Boyd and Lagoudas, 1996) macroscopic free energy model that is inspired from plasticity concepts. This is of interest also because a routine is already developed and made available. It is a FORTRAN code that implements the unified constitutive model presented by (Bo and Lagoudas, 1999), which unifies and generalizes to three dimensions the constitutive models presented by (Tanaka, 1986), (Boyd and Lagoudas, 1996) and (Liang and Rogers, 1997). Its current implementation follows the specifications for user-material subroutines by ABAQUS and it is intended primarily for use with this software, then it is largely used in the ABAQUS–users' community.

The model by Müller and Seelecke (2001) is a so-called free-energy model and its derivation is completely from classical and statistical thermodynamics. This makes it particularly interesting and can take advantage of the characteristics of a multiphysics software like Comsol. Indeed, it is widely appreciated in the Comsol-users' community. The attractiveness of the model is that the complete thermomechanical hysteretic behavior is derived from the energy function alone without any additional loading/unloading criteria. It uses a limited number of parameters to

determine the free energy and they are clearly interpretable and easily obtainable. Together with a convenient mathematical structure in the form of an ODE system, allowing for robust numerical integration, these features make the model an attractive candidate for the simulation of SMA actuators and their control behavior.

In the present chapter, uniaxial tensile tests are used to explore the possibilities of these models, whilst in the following chapter real applications are used as validation of the same three models.

2.1 Tanaka-based model

The first model considered is a uniaxial phenomenological model, based on the one by Zhu and Zhang (Zhu and Zhang, 2007), which has the one by Tanaka (Tanaka, 1986) as a basis and introduces the use of a sigmoidal function as transformation kinetics law. In the present work, this function still describes the evolution of the phase fraction as a function of stress and temperature, but a phenomenological parameter in its argument has been introduced so that the model is adaptable to different mechanical trends. This makes the model suitable for wires with lower or higher content of residual cold-worked material, respectively expressing the previously called flag- and leaf-shaped hysteresis cycles. To examine the effectiveness of the model, two samples have been prepared, treated one at 450 °C (HT wire) and the other at 320 °C (LT wire) and experimental uniaxial stress-strain tensile tests at different temperatures have been used to calibrate and validate the model.

Alongside, an in-depth analysis of the intermediate rhombohedral phase was possible modifying the same model to add this phase. Because of its small mechanical relevance, macroscopic R-phase is often neglected in modeling, although it affects considerably the mechanical behavior of structures sensitive to small strain (e.g. springs, stents, textiles). Two of the first models comprising the R-phase have been (Ikuta et al., 1991) and (Lexcellent et al., 1994), whereas more recent are (Sedlak et al., 2012) and (Chan et al., 2012). An example of a micromechanical model considering R-phase is (Heinen and Miro, 2012). As for the condition of high content of residual cold-worked fraction, it has been widely studied in the works that focus on the effect of thermal aging and annealing, but few examples of models can be found (Wang et al., 2015; Zheng et al., 2008). Originally, the model by Zhu and Zhang does not consider even R-phase, which is instead present in the prepared samples, so it has been modified to include it and simulate all the three phases (austenite, rhombohedral and martensite).

A third aspect is that the two types of annealed wires present different peculiarities: the first has a wide hysteresis loop, while the other reaches high forces. Therefore, the interest is also to explore the possibility to use this two types of wires coupled and to use the model to simulate their joined behavior. Hence, in addition to the tests on single wires, the same experimental tests have been performed to the combination of the two of them, again in order to identify the phenomenological parameters of the model (calibration) and to compare experimental and predicted results (validation).

2.1.1 Appearance of R-phase at different temperatures

The mechanical appearance of the R-phase under a uniaxial tensile test in different range of temperatures has been studied in many works. In particular, one of the first is (Miyazaki and Otsuka, 1986). An extensive study has been done by (Helbert et al., 2014) by realizing tensile tests at different strain amplitudes and temperatures in all the A-to-R transformation range from below R_F^C to above R_S^C. (Olbricht et al., 2011) and (Duerig and Bhattacharya, 2015) studied the behavior of the R-phase in similar temperature ranges and particularly the last performed many tests every 5 °C. The outcomes of their analysis as regards the mechanical behavior of R-phase are described below, where the letters in brackets refer to the same letters in Figure 2-1.

(a) Temperatures below R_F

In this temperatures range, in addition to the stress-induced martensite (SIM) plateau, also that of the stress-detwinned rhombohedral (SDR) appears. The stress at which this plateau triggers, decreases with increasing temperature or at most remains constant. This corresponds, in the phase diagram, to a transformation line with negative or zero slope (Miyazaki and Otsuka, 1986; Olbricht et al., 2011). It is equivalent to that of martensite detwinning (transformation from twinned to detwinned martensite, i.e. reorientation of the martensite variants) at temperatures below Mf. Depending on the temperature, the SDR plateau may appear coupled with a pseudo-plastic behavior (non-recovered residual deformation) or with a pseudo-elastic one (flag shaped appearance).

(b, c) Temperatures comprised between R_F and R_S

Here there is no elastic initial field and the SDR plateau is replaced by a curved section, a bulge shaped “pseudo-plateau”. (Duerig and Bhattacharya, 2015) (Duerig and Bhattacharya, 2015) presented tensile tests every 5 °C in the range of the A to R transformation ($R_F = 0$ °C to $R_S = 50$ °C). Initially increasing temperature from R_F to R_P (roughly 30 °C), the loading path appears with constant curvature and the end of the curved section marks the end of the transformation and the start of a short elastic field before the SIM-plateau. Besides, when surpassing the peak temperature, the curvature of the “pseudo-plateau” starts decreasing while the end of the curved section moves to greater stresses (consistently with the Clausius-Clapeyron). Eventually, the “pseudo-plateau” almost disappears (at 50 °C it is quite a straight line) and the whole path before SIM-plateau seems to be an elastic field, even if the conditions of temperature-stress are in the transformation range. Indeed, in the temperature range above R_P, the starting condition is inside the transformation band with primarily Austenite and it rapidly becomes more difficult to stress induce R (Duerig and Bhattacharya, 2015).

(d) Temperatures above R_S

At temperatures above Rs, the loading path begins with an elastic region of pure austenite and stress-induced rhombohedral (SIR) appears with a reduction of the slope, i.e. with a “pseudo-plateau” with opposite curvature compared to the previous (a hump shaped pseudo-plateau). Even in this case, the clarity of the transformation gradually disappears, because the

superelasticity associated with the SIM coexists with and include the part of deformation associated with the R-phase. Eventually, M is directly stress induced from A and there is apparently no trace of R.

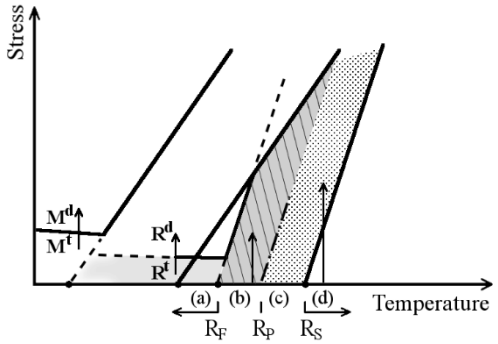

Figure 2-1 - Schematic phase diagram for A to R and R to M transformation. R_S, R_P, R_F are the start, peak and finish temperatures in the A to R transformation. The four temperature ranges are (a) below R_F, (b) between R_F and R_P, (c) between R_P and R_S, (d) above R_S.

It is worth to notice that most of the descriptions found in literature are referred to flag-shaped pseudoelastic trends. Of the two samples presented here instead, the one treated at lower temperature presents the "leaf-shaped" narrow hysteresis and the related transformations are not so clearly distinguishable, because the SIM and SIR are distributed all along the curve.

The behavior described in this section affects then the parameters of the sigmoid for the R-phase transformation, that is to say the kinetic rule, and how to identify the start/finish transformation stresses, i.e. the phase diagram.

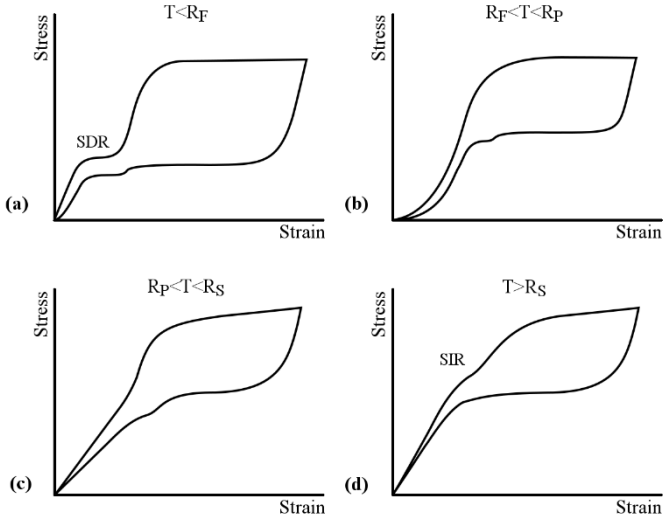

Figure 2-2 - Schematic representation of the mechanical behavior for the R-phase in superelastic wires, in the four temperature ranges. (a) A plateau of the stress-detwinned rhombohedral (SDR) appears before that of SIM. (b) There is no elastic initial field and the stress-induced rhombohedral (SIR) plateau is replaced by a curved section. (c) The curvature of the "pseudo-plateau" decreases while the end of the curved section moves to greater stresses. (d) The loading path begins with an elastic region of pure austenite and SIR appears with a reduction of the slope.

2.1.2 Constitutive model

In short, the model developed by Zhu and Zhang and here modified consists in a mechanical law governing the stress-strain behavior, an energy balance equation that reflects the rate-dependent thermal effect and a transformation kinetics law that describes the evolution of the phase fraction as a function of stress with a sigmoidal law.

2.1.2.1 Stress-strain relation

Following (Brinson, 1993), in the case of small deformation, the strain is no more considered as a whole, but has to be divided between its contributions. Here the strain of the SMA is divided into two parts: ε_{EL}, that is the elastic strain due to the stretching of the material, and ε_{IN}, that is the inelastic strain due to phase transformation (i.e. martensite detwinning). The inelastic strain can be expressed in function of the volumetric phase fraction by means of a parameter (here two: ε_M, ε_R) that can be found in many models with different definitions. It is the maximum residual strain, i.e. a measure of the maximum deformation obtainable only by the detwinning of the multiple-variant martensite and it is regarded as a material constant. Its definition is immediately clear by looking at the Figure 2-3, which represents a uniaxial tensile test that completely detwins martensite (i.e. that reaches the martensite elastic region).

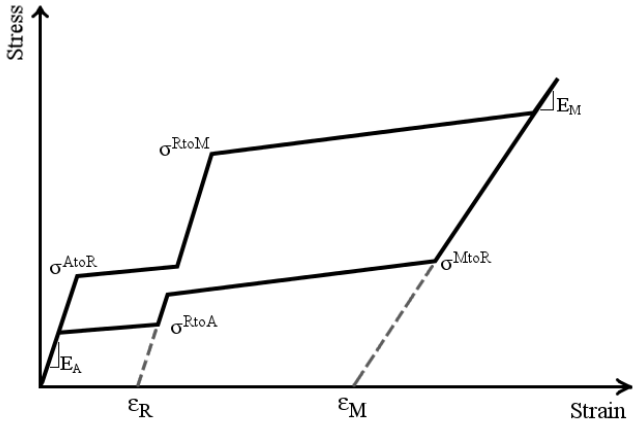

Figure 2-3 - Sketch of a pseudo-elastic uniaxial tensile test; outlined the most important parameters.

In the present case, there are two inelastic contributes due to the detwinning of both martensite and R-phase. The total strain is than defined in equation (2-1), where the pure thermal expansion can be neglected, because it is much smaller and negligible compared with the other three effects.

$$\varepsilon = \varepsilon_{EL} + \varepsilon_M \xi_M + \varepsilon_R \xi_R \tag{2-1}$$

The elastic part of the strain can be then expressed depending on volumetric fractions:

$$\varepsilon_{EL}(\xi) = \varepsilon - \varepsilon_M \xi_M - \varepsilon_R \xi_R \tag{2-2}$$

For the martensitic detwinning, the value assumed for ε_M is 0.07. The A to R and backward transformations occur only at strains below 1 %, contributing to the total deformation with a transformation strain between 1/6 and 1/10 of the one involving martensite, so ε_R is taken in this case equal to 0.008.

The dependence of the Young modulus E from the volumetric fractions is taken in the Voigt form, modified to include R-phase, using the phase fraction as weight for the modulus of the phase itself:

$$E(\xi) = E_A\xi_A + E_M\xi_M + E_R\xi_R = E_A + (E_M - E_A)\xi_M + (E_R - E_A)\xi_R \tag{2-3}$$

2.1.2.2 Thermodynamic relations

From the first and second law of thermodynamics, the energy balance and the differential form of the Clausius–Duhem inequality can be expressed as:

$$\rho\left(\dot{\psi} + \dot{T}\eta + T\dot{\eta}\right) - \sigma\dot{\varepsilon} + \frac{\partial q_S}{\partial x} - \rho q_V = 0 \tag{2-4}$$

$$\rho\dot{\eta} - \rho\frac{q_V}{T} + \frac{\partial}{\partial x}\left(\frac{q_S}{T}\right) \geq 0 \tag{2-5}$$

The Helmholtz free-energy density ψ of superelastic SMAs assumes here the following form, which refers to the expression that has been extensively used in the formulations following Tanaka model:

$$\begin{aligned}\psi \;= (E/2\rho_0){\varepsilon_{EL}}^2 \;+\; (L_h/T_{cr})(T \;-\; T_{cr})\xi_M \;+\; (L_{hR}/T_{crR})(T \;-\; T_{crR})\xi_R \\ - C_pT\; ln(T/T_0)\end{aligned} \tag{2-6}$$

Equation (2-6) is a function of state variables (ε, T, ξ_M, ξ_R) and the terms represent in order the dependence by the strain energy, the latent heat of the two transformations and the specific heat. E and ε_{EL} are both function of ξ_M and ξ_R as stated in equations (2-3) and (2-2). Substituting (2-4) in (2-5) and making explicit the dependence from the state variables, the inequality (2-5) becomes:

$$\left(\sigma - \rho\frac{\partial\psi}{\partial\varepsilon}\right)\dot{\varepsilon} - \left(\eta + \frac{\partial\psi}{\partial T}\right)\dot{T} - \frac{\partial\psi}{\partial\xi_M}\dot{\xi_M} - \frac{\partial\psi}{\partial\xi_R}\dot{\xi_R} - \frac{1}{\rho T}q_S\frac{\partial T}{\partial x} \geq 0 \tag{2-7}$$

From the thermodynamics of continuous media, the coefficients of $\dot{\varepsilon}$ and $\dot{T}$ should vanish in equation (2-7). Thus, the above inequality provides the constitutive equations and the driving force of transformation function of the phase fraction as:

$$\begin{cases}\sigma = \rho\dfrac{\partial\psi}{\partial\varepsilon} \\ \eta = -\dfrac{\partial\psi}{\partial T} \\ \mathrm{A}_x = -\rho\dfrac{\partial\psi}{\partial\xi_x}\end{cases} \tag{2-8}$$

Substituting the expression of Ψ in the above system, the three terms assumes the forms:

$$\sigma^{A,R} = \sigma^{R,M} = \rho \frac{\partial \psi}{\partial \varepsilon} = E\varepsilon_{EL} \tag{2-9}$$

$$\eta^{A,R} = \eta^{R,M} = -\frac{L_h}{T_{cr}}\xi_M - \frac{L_{hR}}{T_{crR}}\xi_R + C_p\left[1 + ln\left(\frac{T}{T_0}\right)\right] \tag{2-10}$$

$$\begin{cases} A_R^{A\leftrightarrows R} = -\rho\dfrac{\partial \psi}{\partial \xi_R} = E\varepsilon_R\varepsilon_{EL} - \dfrac{1}{2}E_R\varepsilon_{EL}^2 - \rho L_{hR}\dfrac{\Delta T}{T_{cr}} \\ A_M^{R\leftrightarrows M} = -\rho\dfrac{\partial \psi}{\partial \xi_M} = E\varepsilon_M\varepsilon_{EL} - \dfrac{1}{2}E_M\varepsilon_{EL}^2 - \rho L_h\dfrac{\Delta T}{T_{cr}} \end{cases} \tag{2-11}$$

2.1.2.3 Transformation Kinetics rule

Different transformation kinetics rules have been proposed to describe the evolution of the phase volumetric fraction of SMAs, however, according to [1], using the sigmoid function reduces the sharp transition at the critical stress, resembling more closely experimental results. Here the kinetics is led by a fully phenomenological expression. This means that it can be tuned empirically to 'resemble' the experimental data. The expression of the sigmoid function is:

$$sig(x) = \frac{1}{1 + e^{-x}} \tag{2-12}$$

The argument x is defined in function of stress and temperature for each of the four transformations:

$$x = -\frac{\ln(\mathrm{P})}{T_S - T_F}\left(T - T_P - \frac{\sigma}{C}\right) \tag{2-13}$$

In the argument expression, T_S, T_F, T_P are the start, finish and peak temperatures respectively, C is the Clausius-Clapeyron stress/temperature ratio and P is a phenomenological parameter that can be modified to better accommodate the experimental behavior.

Considering for each transformation from a parent phase *X* to a product one *Y*, the product volumetric fraction expression becomes:

$$\xi_Y^{X\to Y} = \xi_Y^0 + \xi_X^0 sig_Y \tag{2-14}$$

The superscript zero indicates the value of the fraction at the previous step, while sig_Y means that all the variables (T_S, T_F, T_P and C) are referred to the phase *Y*. In Figure 2-4, the trends and the expressions of the volumetric fractions of the three phases in the four transformations are reported. A feature to pay attention to is the time step of integration Δt. In fact, due to the product of the sigmoid and the fraction ξ_X^0 at the previous step, if Δt is changed, then the rate of growth of the fraction $\xi_Y^{X\to Y}$ changes. In the present case, Δt was equal to the step of data acquisition of the experimental test (0.1 s) and, consequently, the value of the fraction reaches 1 around the peak temperature, when the value of the sigmoid is still 0.5.

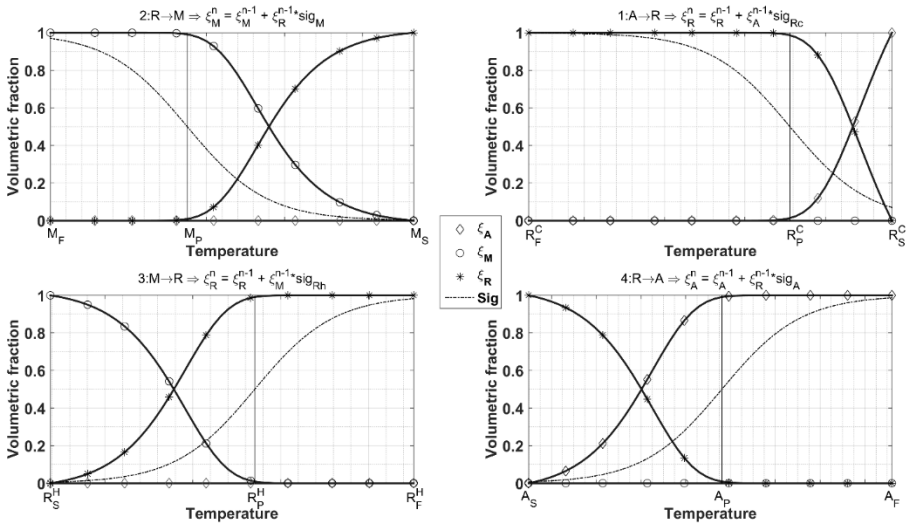

Figure 2-4 - Developments and expressions of the volumetric fractions of the three phases, for the four transformations.

2.1.2.4 Derivation of differential forms

Deriving equation (2-9) with respect to the time, the expression of the ratio of the stress is obtained.

$$\dot{\sigma} = E\dot{\varepsilon} + [(E_M - E_A)\varepsilon_{EL} - E\varepsilon_M]\dot{\xi}_M + [(E_R - E_A)\varepsilon_{EL} - E\varepsilon_R]\dot{\xi}_R - E(\xi)\alpha(\xi)\dot{T} \qquad (2\text{-}15)$$

Starting from (2-4), and substituting $\dot{\eta}$ and $\sigma\dot{\varepsilon}$ we have:

$$\dot{T} = \frac{1}{\rho C_p}\left[E\varepsilon_M\varepsilon_{EL} - \frac{1}{2}E_M\varepsilon_{EL}^2 - \rho L_h\right]\dot{\xi}_M + \frac{1}{\rho C_p}\left[E\varepsilon_R\varepsilon_{EL} - \frac{1}{2}E_R\varepsilon_{EL}^2 - \rho L_{hR}\right]\dot{\xi}_R - \frac{1}{\rho C_p v}\left[\frac{V^2}{R} - k\Delta T\right] \qquad (2\text{-}16)$$

The derivative form of the phase fraction expression comprises the derivative of Temperature, Stress and sigmoid.

$$\frac{\partial sig}{\partial t} = \frac{e^{-x}}{(1+e^{-x})^2} = g \qquad (2\text{-}17)$$

$$x = -\frac{ln(P)}{T_{YS} - T_{YF}}\left(T - T_{YP} - \frac{\sigma}{C_Y}\right) \qquad (2\text{-}18)$$

$$\dot{\xi}_Y^{X\to Y} = \xi_X^0\left[-\frac{ln(P)}{T_{YS} - T_{YF}}\left(\dot{T} - \frac{\dot{\sigma}}{C_Y}\right)\right]\cdot g(x) \qquad (2\text{-}19)$$

The differential equations (2-17), (2-18) and *(2-19)* form the system that has to be implemented in the integration algorithm and solved in the variables $\dot{T}, \dot{\sigma}$ and $\dot{\xi}$.

2.1.3 Implementation

The model described has been implemented in Matlab® with a sequence of nested functions. In the main routine the material data are defined, the experimental test data are uploaded for being compared with the simulation results, the initial conditions are set and the displacement is defined for the whole cycle as control variable. From this routine, all the others are called in cascade. The two lowest levels are the core of the routine. In the four internal functions, the increases of the output quantities are calculated using the differential equations described.

At the next higher level, there is the function that 'chooses' which of the four functions call. The definition of the phase diagram generates four transformation bands (A to R, R to M, M to R, R to A); having different C coefficients, these bands can intersect one with the other and in the superposition areas, more than one transformation per time is possible. At each step of integration, according to the current and previous step values of stress and temperature, it is automatically determined which transformation is in progress. First, using the C coefficients of the four transformations, the start and finish temperatures scaled to the actual level of stress are calculated. Then, it is checked whether the temperature in the previous step falls within one or more ranges of transformation. Finally, depending on the slope of the ratio dσ/dT, it is determined whether the transformation is proceeding in the direction 'from start to finish' or not (Figure 2-5). This condition is verified for every transformation at each step, in this way, the routine examines whether there is more than one valid condition and then settle the uncertainty. Because the range of manifestation of the R-phase is under the 1 % strain, this condition has been added to the triggering of the transformation stress.

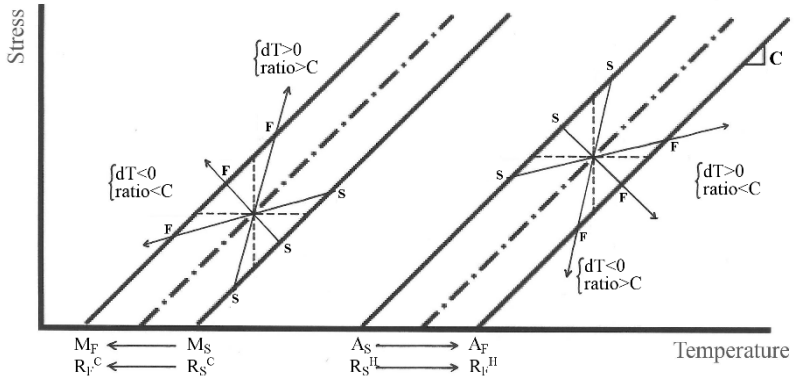

Figure 2-5 - Rules to determine whenever the transformation is proceeding. The rules base on the values of stress and temperature at the current and previous step of integration ($d\sigma = \sigma^n - \sigma^{n-1}$ and $dT = T^n - T^{n-1}$) and their ratio=$d\sigma/dT$

Hence, the correct equations are solved for the ongoing transformation and then integrated with the fourth order Runge-Kutta algorithm.

2.1.4 Model calibration: sigmoid effect

As stated in Section 2.2, in the argument expression of the sigmoid law, P is a phenomenological parameter that can be modified to better accommodate the experimental behavior. In fact, the more P is small, more the sigmoid increment is gradual and the stress-strain plateau slope is

greater. Conversely, with great values of P, the leap of the sigmoid is more concentrated in the neighborhood of the peak temperature, causing a greater curvature both of the sigmoid itself and of the initial part of the plateau, which becomes flatter. The trend of the sigmoid function for different values of P is shown in Figure 2-6 and the corresponding effect on the stress-strain behavior of the transformation is reported in Figure 2-7. Another effect of increasing P is that the sigmoid value at its extremes gets closer to le limit values zero and one (e.g. the sigmoid varies between 0.01 and 0.99 for P 1e+4 and between 0.0001 and 0.9999 for P 1e+8), while it has a constant inflexion point in 0.5 at the peak temperature. This anyway does not influence the limits of the fractions of the phases, calculated incrementally, which are however comprised between zero and one and the sum of which is always 1.

Varying the parameter P allows using it to adjust the shape of the mechanical behavior. For example, a limit of the previous model (Zhu and Zhang, 2007) is that increasing temperature, the hysteresis cycle moves upwards, but without changing shape. Instead, the experimental behavior shows that for higher temperatures, the hysteresis loop becomes tapered, with greater slope of the plateaux. To represent the almost vertical trend of the rhombohedral transformations, a lower value of P equal to 50 has been used for both the wire types, while a value varying from 10.000 to 1000.000 has been used to represent the increasing in the slope of the plateau of R to M and M to R transformations.

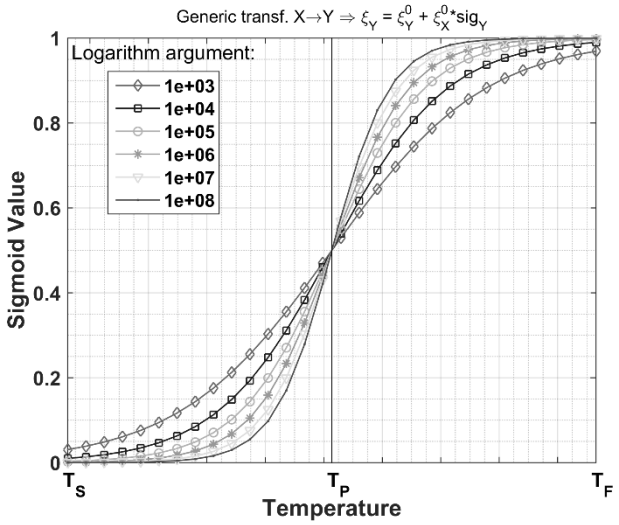

Figure 2-6 - Trend of the sigmoid function between T_S and T_F with different values of the sigmoid logarithm argument P

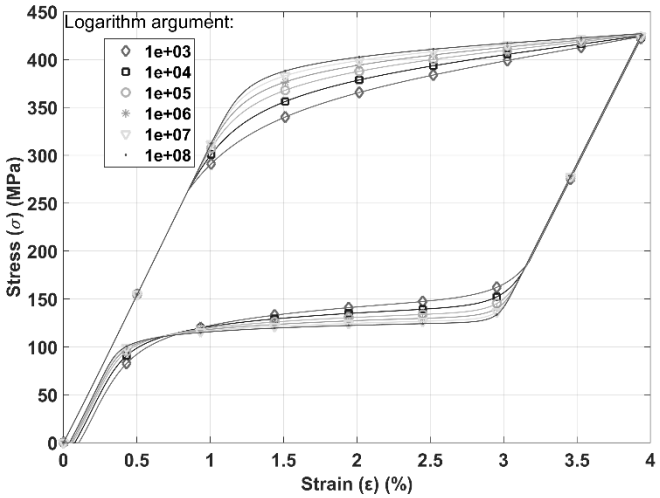

Figure 2-7 - Generic representation of the stress-strain behavior with different values of the sigmoid logarithm argument P

2.1.5 Model validation on tensile test

Quasi-static tensile tests were used to evaluate the mechanical response of the HT and LT NiTi wires. The electromechanical MTS 2\M (MTS Systems) used has a 10kN load cell that grants the forces needed for the LT type. A pair of pneumatic grippers (10 kN gripping force) and a thermal chamber cooled with liquid nitrogen allow controlling the clamping force of the sample and the temperature in the range [-90 °C, +250 °C]. The machine is also equipped with an axial extensometer with 25 mm gage length. The tests on the individual wires were performed on long 50 mm specimens at a controlled displacement rate of 0.5 mm/min. Samples of the same length but different type were coupled and tested through a setup designed specifically for the parallel combination of wires, whose details are described in (Nespoli et al., 2016).

The tests were carried out on the HT sample at four temperatures (reached heating from room temperature) in the range of the R-phase transformation: at 23 °C (between R_F^C and R_P^C), at 34 °C (near the peak temperature), 44 °C (between R_P^C and R_S^C), at 50 °C (little above R_S^C). The second cycle of new specimens was always considered, so the cycling effect is excluded. In Figure 2-8, the comparison of experimental and simulated mechanical behaviors is reported for HT sample and a detail of the trend at low strains, i.e. of the range of interest of the R-phase transformations, is in Figure 2-11.

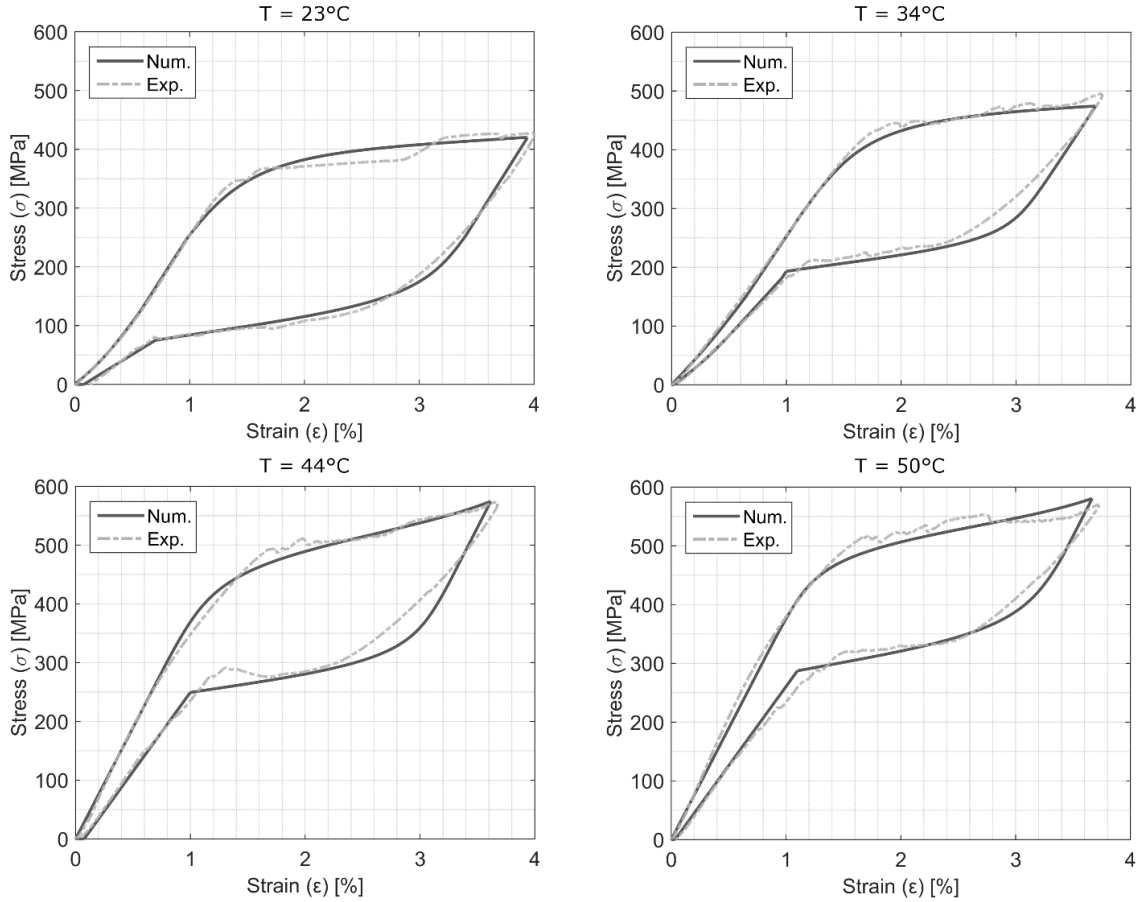

Figure 2-8 - HT tests, experimental vs. simulation comparison for four different test temperatures.

The simulation does not reproduce the fluctuations and leaps in the plateaux due to local effects, but the overall trend is well represented. The simulated global mechanical behavior of the HT sample has a good agreement with the corresponding experimental results, as can be seen in Figure 2-8.

In reference to the loading phase, the two tests below R_P match correctly the behavior presented in the introduction (see Figure 2-2.b), that is, they both have an initial part with an upward concavity. The curvature of the R-phase transformation in these two cases is well approximated, even if it is a little overestimated as can be noticed in Figure 2-11, which shows the range of interest of the R-phase transformations. The last test, the one at 50 °C that is above R_S^C, has a curvature opposite to the first two, as was expected (see Figure 2-2.d). The tests at 44 °C, instead does not agree with the provisions from the literature, because it has a curvature similar to that for higher temperatures. In both these two last cases, the curvature is underestimated, and so the simulation results less precise in the temperature range above R_P.

Some aspects in the unloading phase are however not explained nor reproduced by the model. For example, the beginning of the unloading plateau, is generally worse than the loading one, because the simulation keeps a symmetrical appearance of the hysteresis cycle, whereas, experimentally, the backward transformation begins with a very pronounced curve, as already been observed by other authors (Morin et al., 2011). Moreover, at the beginning of the R to A

transformation, the experimental curves show a stepped curve, due to the discontinuous proceeding of the transformation, while the model correctly considers it as a continue transformation and so with a continue curvature. Another aspect not considered by the simulation is the amount of residual martensite that not re-transforms at the end of the cycle. It could be fixed adding a further parameter in the model that is the fraction of residual martensite, but this was not done in the present simulations and the resulting strain at the end of the cycle is a result of the parameter P in the sigmoid argument. Greater is its value, faster the transformation proceeds and lower is the amount of residual martensite at the end of the cycle.

Moreover, the model allows following the evolution of the other internal variables. Figure 2-9 reports the evolution of martensitic fraction and temperature during transformation. The figure also reports the value of the parameter H that is used to determine whether the transformation is proceeding and in which direction as described in Section 2.1.3. Figure 2-10 shows the self–heating and cooling during direct and reverse transformations.

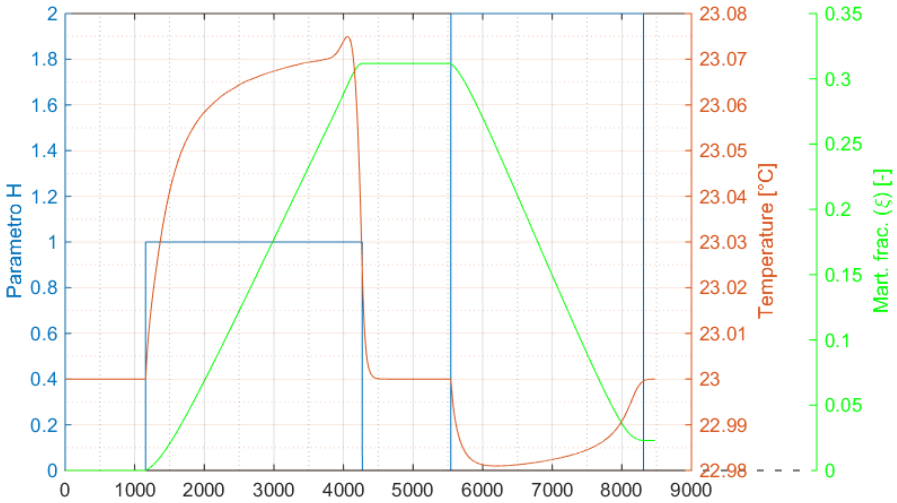

Figure 2-9 - Evolution of martensitic fraction and temperature with the step index.

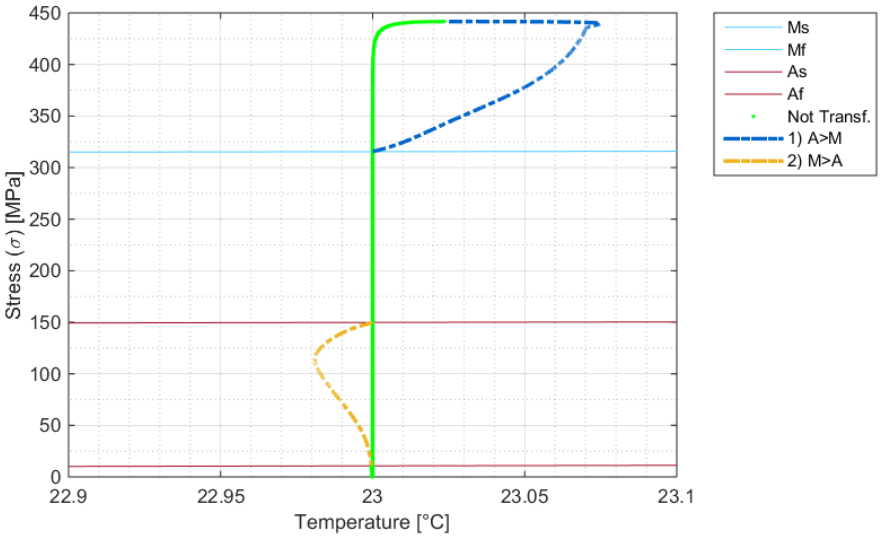

Figure 2-10 - Evolution of temperature and stress during transformation

As said, the two wires annealed at high and low temperature present a wide hysteresis loop and high forces, respectively. Therefore, the interest is also to explore the possibility to use this two types of wires coupled and to use the model to simulate their joined behavior. For this reason, in view of their coupling, the tests on LT and on the pair were at the same temperatures of the HT sample. Considering that the test temperatures were reached starting from room temperature, for the tests on the LT the first two test temperatures (23 °C and 34 °C) fall in the range of the R-to-A peak between A_P (+0.7 °C) and A_S (+41.4 °C) and the last two (44 °C and 50 °C) are above A_S. The results for the LT sample can be seen in Figure 2-12.

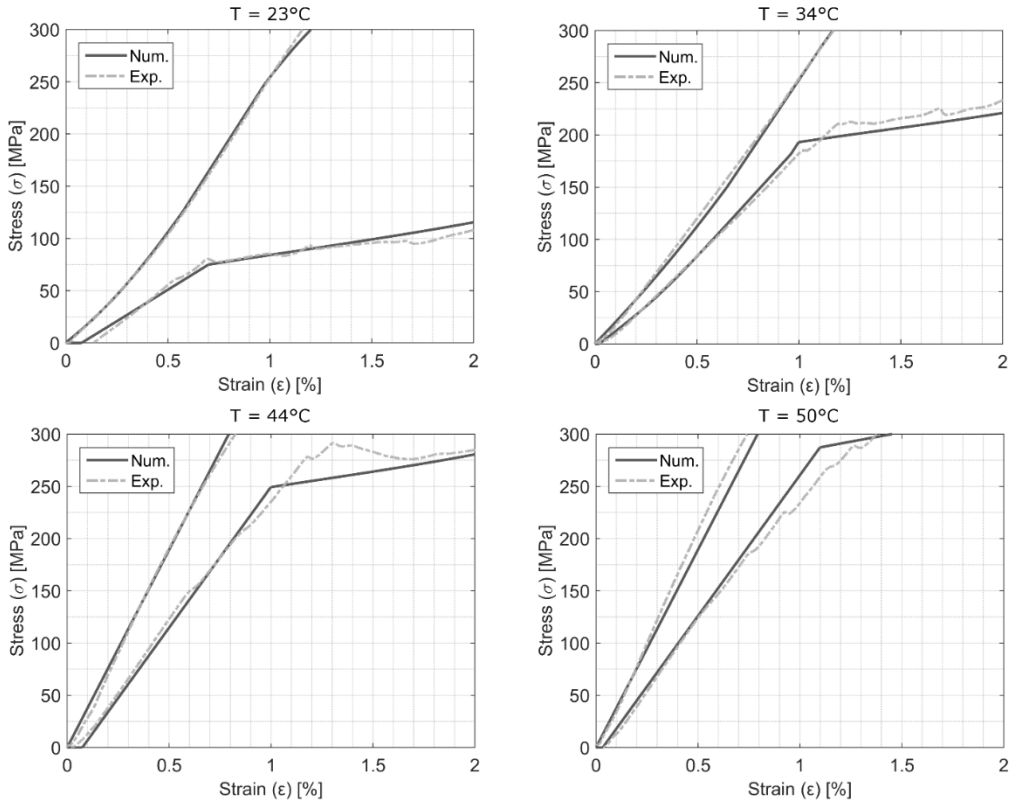

Figure 2-11 - HT, zoom out of the trend of the experimental vs. simulation comparison for four different test temperatures at low strains.

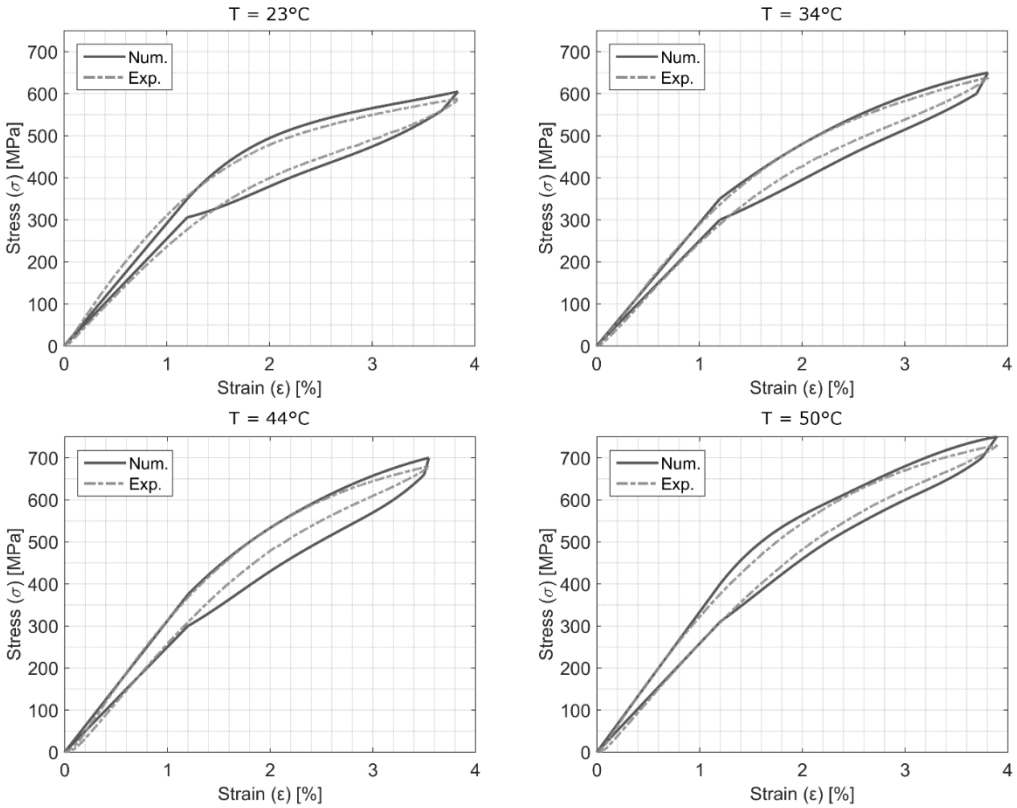

Figure 2-12 - LT tests, experimental vs. simulation comparison for four different test temperatures.

The descriptions of the R-phase behavior found in literature and depicted in Figure 2-2 are all referred to flag-shaped pseudoelastic trends, typical of HT samples. For the LT one, the experimental trend is more leaf-shaped and the transformations are not so clearly distinguishable, because the SIM and SIR are distributed all along the curve. The curvature is continuous and there are no discontinuities where the transformations start and end, nor during loading nor unloading. Because the model is developed for a HT sample, it rather presents such discontinuities, which are therefore an intrinsic defect of the simulation.

The initial part of the loading part (transformation A to R) was considered always straight, having no way to assume that a different trend represents the general behavior. For the first two tests, the correlation is fairly good, because the initial section is quite straight also in the experiment. For the other two, instead, the experimental behavior has a small initial plateau, while it should start with a straight elastic region. Regarding the unloading part (backward transformation), the discontinuity at the beginning of the transformation R to A is much more evident than in loading.

2.2 Boyd and Lagoudas model

2.2.1 Constitutive model

All the model family created by Lagoudas is macromechanical thermodynamic and three-dimensional. The investigated model has been originally presented by (Boyd and Lagoudas, 1996) and then generalized by (Lagoudas et al., 2012). The model assumes stress and temperature as control variables, and the transformation strain, the total martensitic volume fraction and the transformation energy as internal ones.

The Lagoudas model extends the work done by (Sun and Hwang, 1993), performing micromechanical analysis to obtain Gibbs free volume of a representative volume (RVE) element in the presence of rate-independent plastic deformation. Assuming a small strain regime, the Gibbs free-energy function is taken as the weighted sum of energy of Austenite, Martensite and a mix of the two phases:

$$G = (1-\xi)\, G^A + \xi G^M + G^{mix} \tag{2-20}$$

$$G^i = -\frac{1}{2\rho}\,\boldsymbol{\sigma} : \mathbf{S}^i \boldsymbol{\sigma} - \frac{1}{\rho}\,\boldsymbol{\sigma} : \boldsymbol{\alpha}\,(T - T_0) + c^i \left[T - T_0 - T \ln\left(\frac{T}{T_0}\right)\right] - s_0^i T + u_0^i \tag{2-21}$$

$$G^{mix} = f(\xi) \tag{2-22}$$

Model parameters, S, c, s_0, and u_0, denoting the compliance tensor, specific heat, specific entropy at the reference state, and specific internal energy at the reference state, respectively, are assumed to be different for each phase and are defined using the rule of mixtures.

$$\begin{cases} \mathbf{S} = \mathbf{S}^A + \xi\left(\mathbf{S}^M - \mathbf{S}^A\right) \\ c = c^A + \xi\left(c^M - c^A\right) \\ s_0 = s_0^A + \xi\left(s_0^M - s_0^A\right) \\ u_0 = u_0^A + \xi\left(u_0^M - u_0^A\right) \end{cases}$$

Parameters ρ and α, denoting the density and the thermal expansion, respectively, are assumed the same regardless of phase.

The function $f(\xi)$ is the transformation hardening function. By choosing its functional form, different SMA constitutive models can obtained, as described by (Lagoudas et al., 2003). To obtain the constitutive model presented by Boyd and Lagoudas (1996) it is selected as:

$$f(\xi) = \begin{cases} \frac{1}{2}\rho b^M \xi^2 + (\mu_1^p + \mu_2^p)\xi, & \dot{\xi} > 0, \\ \frac{1}{2}\rho b^A \xi^2 + (\mu_1^p - \mu_2^p)\xi, & \dot{\xi} > 0. \end{cases} \tag{2-23}$$

The quantities a_e^M, a_e^A, μ_1^e, a_c^M, a_c^A, μ_1^c, b^M, b^A and μ_1^p are material constants, while μ_2^e, μ_2^c and μ_2^p are introduced to enforce continuity for the function during forward and reverse transformation.

The total strain ε is given by:

$$\boldsymbol{\varepsilon} = \mathbf{S} : \boldsymbol{\sigma} + \boldsymbol{\alpha}(T - T_0) + \boldsymbol{\varepsilon}^t. \tag{2-24}$$

The evolution equation for the transformation strain tensor, $\dot{\boldsymbol{\varepsilon}}^t$, is defined as a function of the martensitic volume fraction, through the transformation tensor $\boldsymbol{\Lambda}$, which determines the transformation strain direction.

$$\dot{\boldsymbol{\varepsilon}}^t = \dot{\xi}\boldsymbol{\Lambda}^t \tag{2-25}$$

Two different forms of the transformation tensor Λ are implemented. The form recommended for computations and suitable for cases of proportional loading (e.g. uniaxial loading) uses the fraction rate to determine the transformation direction:

$$\boldsymbol{\Lambda} = \begin{cases} \frac{3}{2}H\frac{\boldsymbol{\sigma}'}{\bar{\sigma}}, & \dot{\xi} > 0 \\ H\frac{\boldsymbol{\varepsilon}^{t-r}}{\bar{\varepsilon}^{t-r}}, & \dot{\xi} < 0 \end{cases} \tag{2-26}$$

$$\bar{\sigma}^m = \sqrt{\frac{3}{2}}\|\boldsymbol{\sigma}^{m\prime}\|, \qquad \boldsymbol{\sigma}^{m\prime} = \boldsymbol{\sigma}^m - \frac{1}{3}\mathrm{tr}(\boldsymbol{\sigma}^m)\mathbf{I}, \qquad \bar{\varepsilon}^{t-r} = \sqrt{\frac{2}{3}}\|\boldsymbol{\varepsilon}^{t-r}\| \tag{2-27}$$

H is the maximum uniaxial transformation strain ε^{t-r} is the transformation strain at the reversal of the transformation.

The second form of the transformation tensor Λ is conceived for more complicated loading cases and should be used if convergence problems are experienced. This is independent of the transformation direction, and results:

$$\boldsymbol{\Lambda} = \frac{3}{2}H\frac{\boldsymbol{\sigma}'}{\bar{\sigma}} \tag{2-28}$$

Then the transformation function Φ is defined, which allows to evaluate whether the martensitic transformation evolves, i.e. if the martensitic fraction varies. Constraints on the evolution of the martensitic volume fraction are expressed in terms of the Kuhn-Tucker conditions as:

$$\Phi \leqslant 0, \quad \Phi\dot{\xi} = 0, \quad \Phi = \begin{cases} \pi - Y & \dot{\xi} > 0, \\ -\pi - Y & \dot{\xi} < 0. \end{cases} \tag{2-29}$$

When the transformation function Φ is negative, the rate of the martensitic fraction is fixed at zero and therefore the transformation does not occur; when Φ is equal to zero the rate of martensitic

fraction can be non-null and thus indicate a direct or inverse transformation. Term π is the thermodynamic force conjugate to the martensitic fraction driving the transformation.

$$\pi = \boldsymbol{\sigma} : \boldsymbol{\Lambda} + \frac{1}{2}\boldsymbol{\sigma} : \Delta\mathbf{S} : \boldsymbol{\sigma} + \Delta\boldsymbol{\alpha} : \boldsymbol{\sigma}(T - T_0) - \rho\Delta c \left[(T - T_0) - T \ln\left(\frac{T}{T_0}\right) \right] + \rho\Delta s_0 T - \frac{\partial f}{\partial \xi} - \rho\Delta u_0 \quad (2\text{-}30)$$

$f(\xi)$ is the transformation hardening function seen above, the terms with the prefix Δ indicate the difference of a quantity between the martensitic and austenitic phases

Y is a constant of the material describing the internal dissipation due to a complete cycle of transformation (is the amount of energy per unit of volume required for a complete conversion cycle).

2.2.2 SMA_UM routine

SMA_UM (Shape Memory Alloy - Unified Model) is a FORTRAN code that implements the unified constitutive model presented by (Bo and Lagoudas, 1999), which unifies and generalizes to three dimensions the constitutive models presented by (Tanaka, 1986), (Boyd and Lagoudas, 1996) and (Liang and Rogers, 1997).

The model is numerically implemented using return mapping algorithms. Detailed description of the implementation is provided in the research paper by (Qidwai and Lagoudas, 2000). Despite the subroutine can be integrated in any other standard finite element or computational program, its current implementation follows the specifications for user-material subroutines by ABAQUS and it is intended primarily for use with ABAQUS. The subroutine can be used in 3-D, 2-D plane strain and generalized plane strain, and 1-D problems. The SMA_UM and associated example input files are available for use at two links on the web–page of the SMART laboratory at Texas A&M university.

SMA_UM subroutine requires some material parameters to be defined. The syntax of the definition in the input file is the following:

```
*MATERIAL, NAME=SMA
*DENSITY
dens
*SPECIFIC HEAT
spH
*CONDUCTIVITY
cond
*DEPVAR
100
*USER MATERIAL, CONSTANTS=24
IPHASE,MODEL,TOL,xi0,NELMTP,EA, EM,nu,
alphaA,alphaM,Mos,Mof,Aos,Aof,H,rDs0A,
rDs0M,epstr11,epstr22,epstr33,2epstr23,2epstr13,2epstr12,FRULE
```

After the definition of density, specific heat and conductivity, the number of solution-dependent state variables is given after the keyword `*DEPVAR`. Next, the input parameters for the subroutine are given under the keyword `*USER MATERIAL`, where the number of the material constant is given after the keyword `*CONSTANTS`. Due to the ABAQUS requirements, the parameters are given in groups of eight entries per line. The parameters are defined in Table 2-1, where bold font is used for physical parameters.

Table 2-1 – SMA_UM input parameters

ID	Name	Definition	Suggested values
1	**IPHASE**	The initial phase of the material	1 - austenite, 2 - martensite
2	MODEL	The constitutive model	1 - Tanaka's exponential model, 2 - Boyd and Lagouda's polynomial model, 3 - Liang and Rogers's cosine model
3	TOL	Convergence criterion tolerance: the iteration process terminates if the absolute value of the increment of the martensitic volume fraction is less than TOL	1.0e-08
4	**xi0**	Initial value of the martensitic volume fraction	consistent with initial phase
5	NELMTP	Number of integration points in all SMA finite elements	16
6,7	**EA,EM**	Young modulus for austenite and martensite	experimentally derived from isothermal tests
8	**nu**	Poisson ratio (assumed 0.33)	
9,10	**alphaA, alphaM**	Thermal expansion coefficient of austenite and martensite	experimentally derived from isostress tests
11-14	**Mos,Mof,Aos,Aof**	Start(s) and finish(f) transformation temperatures of martensite and austenite	experimentally derived from DSC
15	**H**	Maximum transformation strain	
16,17	**rDs0A,rDs0M**	Stress influence coefficient of austenite and martensite	
18-23	epstrXX	Initial value of the XX-component of the transformation strain tensor	set to zero
24	FRULE	Flag for the form of the transformation tensor	1 - suitable for proportional loading cases (e.g., uniaxial loading), 2 - for more complicated loading cases

Note that any consistent units system may be used for the mechanical parameters. However, in parameters involving temperature, this must be expressed in Kelvin. In the present and following chapters, SI units are used.

The elastic Young's moduli of the austenite and martensite can be determined from the uniaxial PE test by measuring the slope of the stress-strain curve at the beginning of the loading at the

beginning of the unloading. From the same test also the maximum transformation strain H and the transformations trigger stresses σ_A and σ_M can be defined (see Figure 2-13). The stress influence coefficients are defined as:

$$\rho\Delta s_A = -\frac{\sigma_A}{T_{test}-A_S}H \qquad \rho\Delta s_M = -\frac{\sigma_M}{T_{test}-M_S}H \tag{2-31}$$

T_{test} is the temperature at which the PE test is performed. The fractional terms of the above expressions are the slopes of the transformation lines in the phase diagram. Using many tensile tests at different constant temperature or different constant stress, they can be univocally estimated as the linear regression of the values of stresses vs. temperatures.

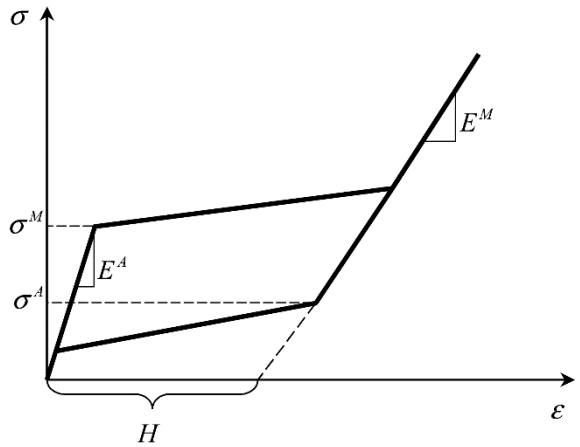

Figure 2-13 - Schematic representation of a SMA uniaxial PE test

2.2.3 Model sensitivity

The model for this test is quite simple and consists of a beam, whose geometric data are taken equal at the ones of the tested sample, which has one end fixed and the other loaded. The wire commercial name is Smartflex (producer: SAES Getters) and is a NiTi (49-51 at.%) SMA, 0.2 mm diameter. Two static steps simulate loading and unloading; the control variable is the displacement during the loading step and the force during the unloading one. The objectives of this sub-section are to test the efficiency of the user subroutine in reproducing the material stress-strain behavior and to calibrate the input parameters required by the model.

The experimental characterization of the wire comprises DSC analysis and mechanical tests, both stress-strain isothermal and strain-recovery isostress. From this characterization, the following physical parameters are derived:

Transformation temperatures:

- Ms = 13.82 °C
- Mf =-7.65 °C
- Rs = 67.20 °C
- Rf = 48.39 °C
- As = 60.62 °C
- Af = 75.11 °C

Elastic moduli:

- EA=40.2e+9 Pa;
- EM=26.0e+9 Pa

Thermal expansion and Clausius–Clapeyron coefficients:

- $\alpha_A = 12e\text{-}06\ 1/K$
- $\alpha_M = 6e\text{-}06\ 1/K$
- $d\sigma/dT(Af) = 8.72\ MPa/K$
- $d\sigma/dT(Ms) = 7.39\ MPa/K$

Stress-strain tests are also reported in Figure 2-14. From these tests, two PE cycles at room temperature (25 °C) and high temperature (105 °C) are selected for comparison used in the following section.

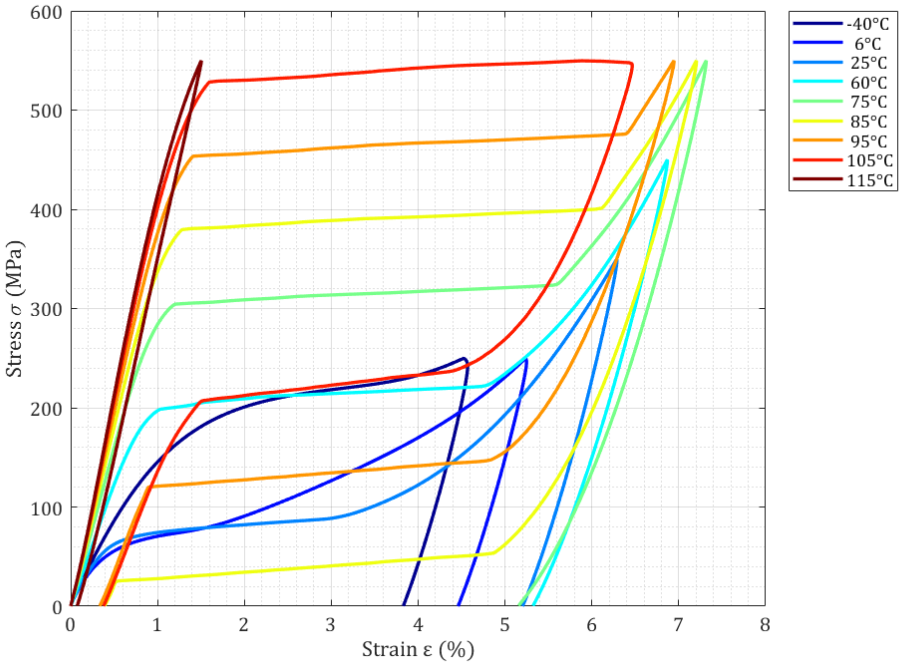

Figure 2-14 - Experimental characterization of stress-strain tests at different temperatures.

To understand the role of the parameters that links the stress–influence coefficient (σ_A, σ_M, H), a Matlab routine has been implemented to write the input files for different parameters combinations, run the corresponding ABAQUS analysis, write, read and then plot the stress-strain reports from the results files (*.odb extension). The results of this sensitivity analysis are reported in the following three figures, where the experimental test is the dotted black line and the influence of a single parameter is evaluated maintaining the other fixed. As can be seen from Table 2-1, some physical parameters, like specific heat, specific entropy and specific internal energy are not input parameters for the model and then the routine has to be modified in order to change their value.

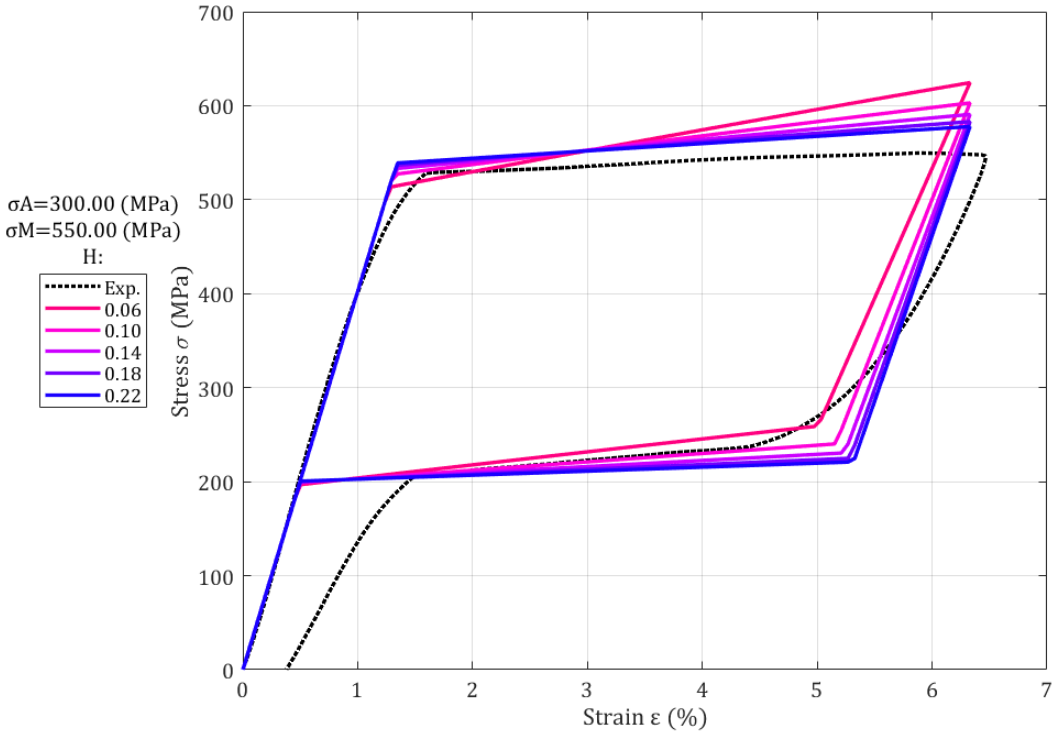

Figure 2-15 - Sensitivity to the maximum transformation strain H at 105 °C

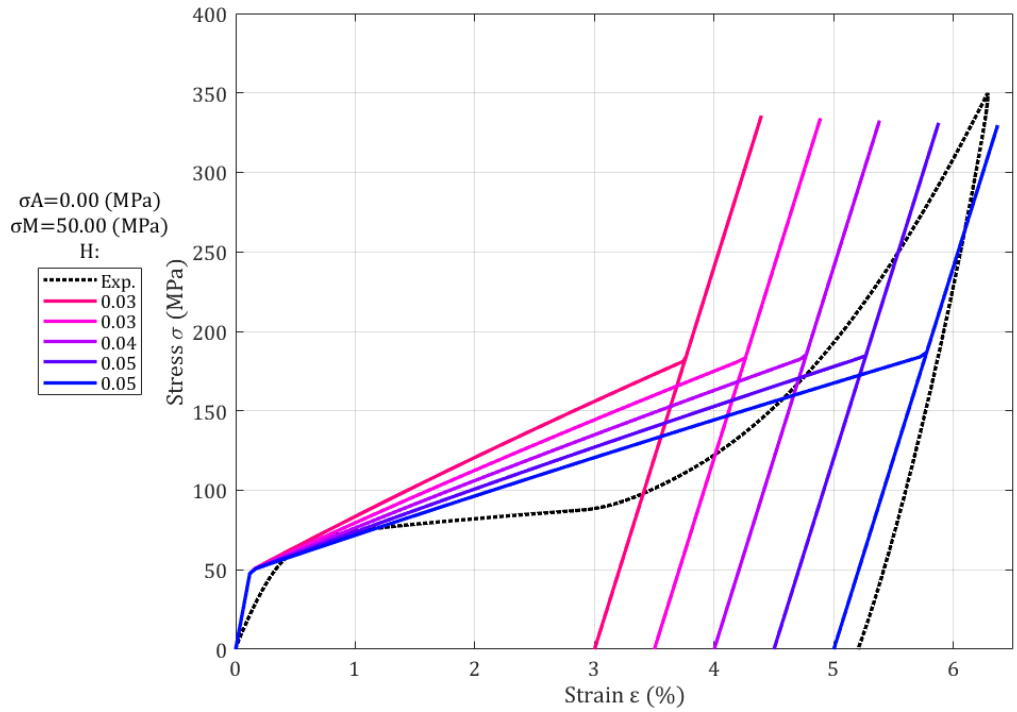

Figure 2-16 - Sensitivity to the maximum transformation strain H at 25 °C

The H parameter is one of the most important characteristic of the material, which is the transformation strain (see also Figure 2-13 and Figure 2-20). With this test, an evident effect is that, increasing the value of the H parameter, the slope of the plateau decreases. Nevertheless, this is a sort of parasitic effect, since it depends on the fact that the stress at the end of the transformation remains unchanged and then the slope of the plateaux has to adjust to reach the

stress value at different maximum strains. It can be observed that the transformation plateaux become flat in the austenite cycle only with H value very high (over 0.14). Another main consideration is that H is an intrinsic characteristic of the material, and then it should remain unchanged for the two test temperatures. Doing so, it is evident that the user has to decide whether the plateaux slope in austenite or the recovery strain in martensite is the most important aspect. In the selection of this parameter in the context of an actuation application, the second is to favor.

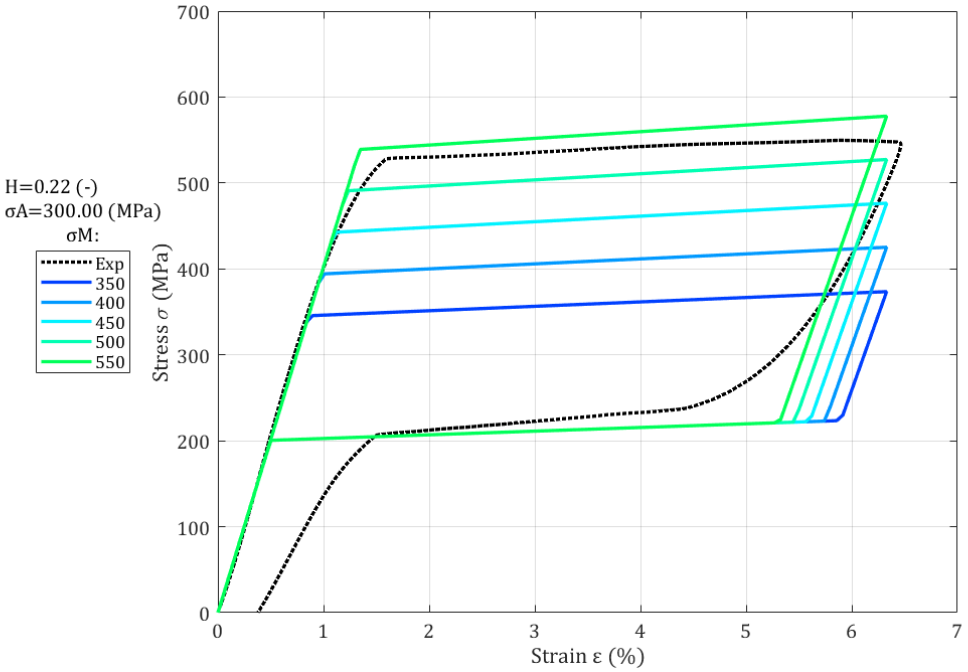

Figure 2-17 - Sensitivity to the Austenitic transformation trigger stress σ_A

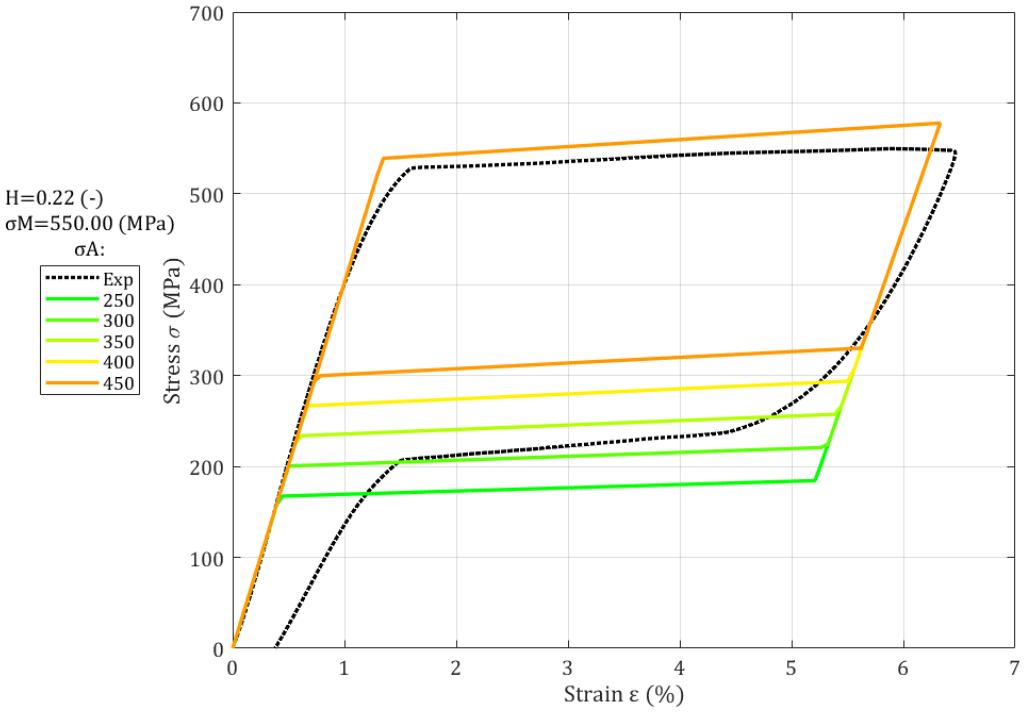

Figure 2-18 - Sensitivity to the Martensitic transformation trigger stress σ_M

The triggering stresses for the transformation are tuned varying the stress–influence coefficient at fixed H. The value of the stress makes the corresponding plateaux shift rigidly based on the Clausius–Clapeyron coefficient that leads a linear increasing of the stress with growing temperature.

In all these figures, note that, since the control of the loading step is the displacement, the austenitic transformation ends only ones reached the maximum value of deformation imposed.

Basing on the results of this analysis, the values selected for the material simulation are:

- H = 0.052
- rDs0A = –4.53e+05
- rDs0M = –3.84e+05

2.2.4 Model validation on tensile test

The tests are isothermal, then the two temperatures (105°C and 25°C) are imposed as Predefined Field in ABAQUS. In both cases, the martensite is not in stable state, so the phase created under loading is Stress-Induced-Martensite (SIM). The values of the parameters are given by the experimental characterization and the sensitivity analysis reported in previous sections.

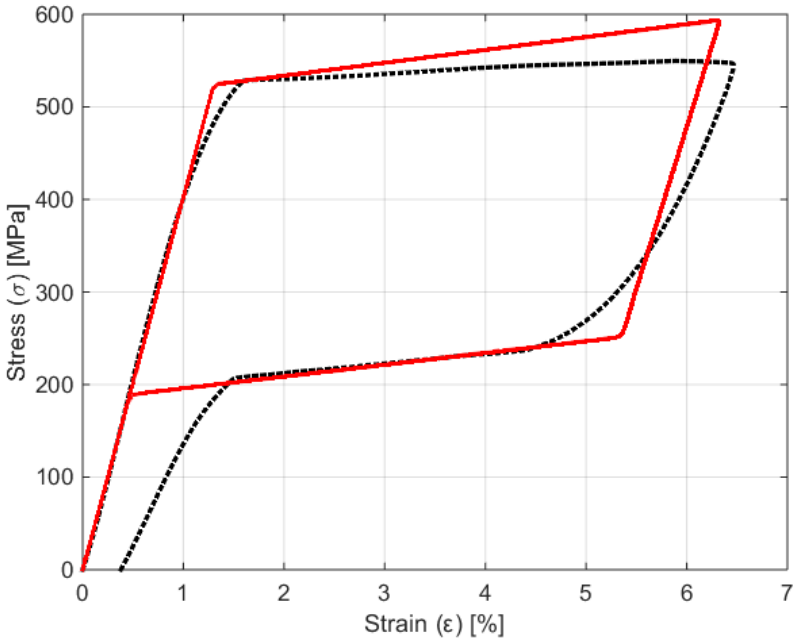

Figure 2-19 - Result of the Abaqus analysis (red line) vs. experimental result (dotted black line) for the test at 105°C

At temperatures higher than A_F, where the austenite is the stable phase, the behavior of PE effect is expressed. Increasing the load, when the trigger stress σ_M for the test temperature is reached, the Martensitic transformation starts and the SIM is produced. Reached the maximum displacement (i.e. deformation), the unloading step is taken to zero load. The stress decreases until the trigger stress σ_A is reached and the Austenitic transformation starts making the phase returning to austenite.

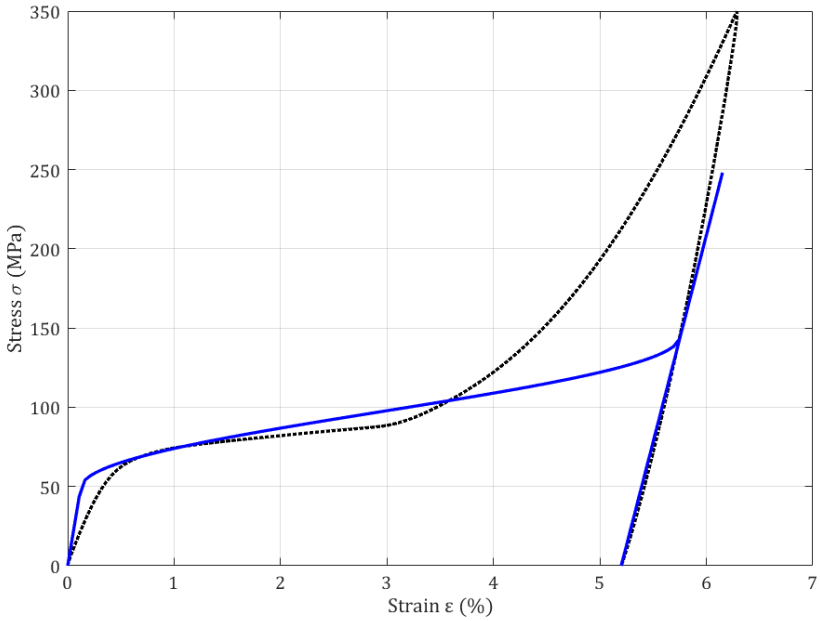

Figure 2-20 - Result of the Abaqus analysis (blue line) vs. experimental result (dotted black line) for the test at 25°C

At room temperature, increasing the load, the twinned martensite undergoes Martensitic transformation and becomes de-twinned martensite. Unloading the sample, the material does not pass through Austenitic transformation, which is at higher temperatures, so the deformation is not recovered until the sample is heated above A_F. Because the displacement do not reset to zero, in this test is particularly important that the control variable of the unloading step is the force.

Since the parameters have been selected to favor the maximum transformation strain, the slope of the plateaux in the high-temperature test is higher than the experimental one. At the same time, the residual strain for the room-temperature test is correct, thanks to the H parameter that is set at 0.052. The curve in Figure 2-20 highlights that the stress in the final part of the transformation at room temperature is underestimate, but this is a common feature for quite all the models, which do not catch the actual shape of the hysteresis cycle at low temperature. Note also that the model implemented through this material subroutine not account for residual strain in PE condition (Figure 2-19). A little amount of martensitic fraction, which not retransforms at the end of Austenitic transformation, is normally present and disappears with cycling.

2.3 Müller–Achenbach–Seelecke model

Another model that has recently been applied to SMA actuator applications has originally been developed by Müller and Achenbach (Achenbach et al., 1986; Achenbach and Müller, 1985, 1982). It uses ideas from statistical thermodynamics and describes the evolution of two martensite fractions based on the theory of thermally activated processes. The model is able to qualitatively simulate the behavior of SMAs over the whole range of temperatures from pseudoplasticity to pseudoelasticity. Building on these works, (Müller and Seelecke, 2001) postulate that the interfacial energy arising out of coherency mismatch is responsible for the hysteresis. Through the calculation of the Helmholtz free energy as the effective potential energy, (Seelecke and Müller, 2004) has also able to make been quantitative predictions for a single-crystal assumption. The model used in this chapter refers to this version of the model with the acronym "MAS model"; in the following chapters, further developments will be discussed.

2.3.1 Constitutive model

With reference to micromechanics of martensitic transformation, it is well known that the peculiar behavior of SMA is given by a phase transition in the crystal lattice structure between two solid phases. The MAS model considers a single crystal material under uniaxial loading and then accounts for a couple of twin variants of martensite aligned in the direction that accommodate stress. In the one-dimensional case, a lattice particle does either exist as the highly symmetric austenite phase A, or as a sheared version hereof. Then, the couple of twin variants of martensite are indicated by M_+ or M_-, depending on the direction of shear.

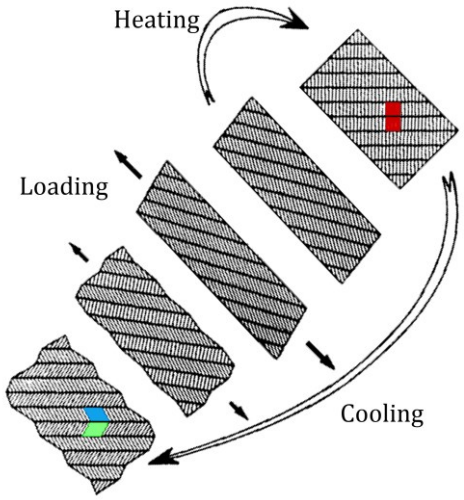

Figure 2-21 - Layer structure of an SMA specimen. The three

Figure 2-21 schematizes the behavior of these layers in a tensile experiment. Initially, at low temperature, twinned martensite is stable and then there is coexistence of M_+ and M_- equally distributed. Applying a tensile external load, the behavior of a pseudoplastic cycle. First, the twinned variants contribute to stretching with their elastic deformation; then, at a critical load level, detwinning occurs and the M_- layers flip into the M_+ phase that accommodates stress direction; finally, unloading, the deformation persists because the detwinned martensite is stable

at low temperature too. To obtain the shape recovery, the material has to be heated, so that all the layers transform into the undeformed austenitic phase and this causes the body to shorten again. Subsequent cooling finally completes the cycle by having the martensitic twins occur again.

In order to describe this behavior, the model takes the metallic layers as basic elements. The total length change and then strain of the wire is calculated as the sum of the strains of the individual layers, weighted by their volumetric fraction:

$$\varepsilon = x_A \varepsilon_A + x_+ \varepsilon_+ + x_- \varepsilon_- \tag{2-32}$$

The strain due to austenite is only its elastic part, while for the two martensite the maximum transformation strain ε_T is introduced.

$$\varepsilon = x_A \frac{\sigma}{E_A} + x_+ \left(\frac{\sigma}{E_M} + \varepsilon_T\right) + x_- \left(\frac{\sigma}{E_M} - \varepsilon_T\right) \tag{2-33}$$

This gives the stress-strain relationship:

$$\sigma(t) = \frac{\varepsilon(t) - \varepsilon_T\big(x_+(t) - x_-(t)\big)}{x_A(t)/E_A + \big(x_+(t) + x_-(t)\big)/E_M} \tag{2-34}$$

The transformation strain ε_T is the same as the parameter H in the Lagoudas model (Figure 2-13) but assumes here also a thermodynamic meaning. Each shear length Δ (i.e. each strain value) corresponds to a certain amount of potential energy $\Phi(\Delta,T,P)$ seen by a layer that is given by a triple-well function with each well corresponding to one of the three phases (Figure 2-22). The potential Φ is characterized by two stable minima for the martensitic twins (in the shear lengths $\Delta = \pm J$, which corresponds to the shear of the B19' crystal in NiTi and then to ε_T).and by a metastable minimum for the austenite. In between these minima, there are potential barriers at $\Delta = \pm\Delta_s$.

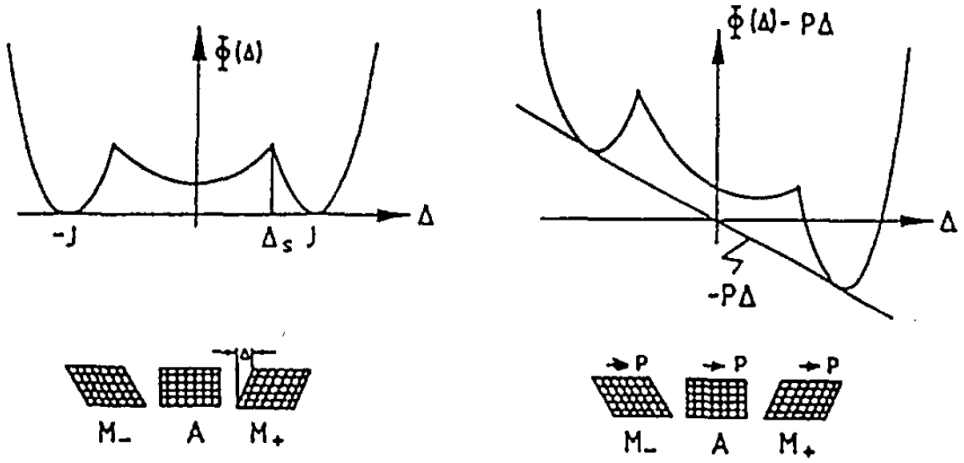

Figure 2-22 - Lattice particle phases and corresponding potential energy i n unloaded condition (left) and with loading P (right)
(Müller and Seelecke, 2001)

If the lattice particle is subject to a shear load P, the potential energy of the load must be added. This is a linearly decreasing function of Δ, and therefore, the potential energy of the particle

becomes distorted. The right minimum becomes deeper, making it the only stable minimum, and the barriers change their heights. When the temperature increases, the entropic stabilization participate modifying the potential Φ. The entropy in austenite is bigger than in martensite, and therefore, at higher temperatures – where the entropic contribution to the free energy matters – the entropy successfully competes with the energy that naturally favors the martensite. Then martensitic minima rise and the austenite becomes stable as soon as it has the smaller free energy.

In the variant of the model here implemented, the potential Φ is defined with five parabolas (Figure 2-23) in the form of the Helmholtz free energy:

$$\psi_i(\varepsilon) = a_i\varepsilon^2 + b_i\varepsilon + c_i, \quad i \in \{1,2,3,4,5\} \tag{2-35}$$

$$g(\varepsilon_{\sigma i}, T) = \psi(\varepsilon_{\sigma i}, T) - \sigma\varepsilon_{\sigma i} \tag{2-36}$$

$$\sigma(\varepsilon) = \frac{d}{d\varepsilon}\psi(\varepsilon) \tag{2-37}$$

The parabolas give 15 unknown coefficients *a, b, c* and the material physics give other 4 unknown parameters the strain of the martensitic minima ε_T, the two strain values of the tangent points between the parabolas and the potential value for austenite. The free energy can be completely defined through mathematics constraints (4 for continuity, 4 for differentiability, 6 for zero derivative and energy values in strain points $= 0, \pm\varepsilon_T$) and material characterization (5 parameters from Young moduli of pure phases, transformation stresses and maximum transformation strain).

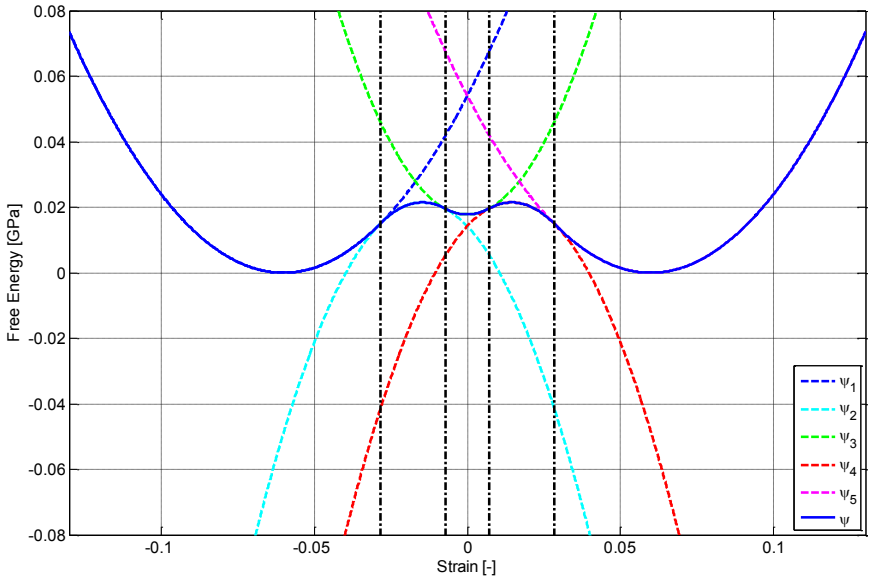

Figure 2-23 - Construction through five parabolas of the Free energy of the lattice

The kinetic rate laws for the phase fractions, which describe their evolution in time, are derived with arguments from the theory of thermally activated processes. The fraction of martensite (M_+ in case of positive loading) can only be altered by an exchange of particles with its neighboring

phase. Hereby, this exchange consists of a loss proportional to the quantity of this particles expressed by the volumetric fraction. The factors of proportionality with the fraction are called phase transformation probabilities and are indicated with p^{ij} for the transformation from phase i to the phase j.

$$\begin{cases}\dot{x}_+ = -x_+ p^{+A} + x_A p^{A+} \\ \dot{x}_- = -x_- p^{-A} + x_A p^{A-}\end{cases} \qquad p^{ij}(\sigma, T) = \frac{1}{\tau_x}\exp\left(-\frac{V_L}{k_B T}\Delta g_{ij}(\sigma, T)\right) \tag{2-38}$$

k_B is the Boltzmann's constant, τ_x the frequency for the transition and V_L the volume of an active layer.

Completes the model the balance energy, considering conductive heat exchange within the wire, the heat exchange with the environment, the Joule heating required for actuation and the latent heats of the phase transitions:

$$mc\dot{T} - k\frac{\partial^2 T}{\partial x^2} = -hA(T - T_{amb}) + H_+\dot{x}_+ + H_-\dot{x}_- + J \tag{2-39}$$

The equations (2-38) and (2-39) together with (2-34) constitute a system of nonlinearly coupled differential equations (an ODE and a PDE) and an algebraic relation. Together with appropriate initial conditions for phase fractions and temperature and prescribed heating function J(t), it can be solved for the resulting length change or, by inversion of (2-34), the load.

2.3.2 Implementation

This system can be easily implemented in COMSOL PDE module. It requires partial differential equations to be expressed in the general form:

$$e_a\frac{\partial^2 u}{\partial t^2} + d_a\frac{\partial u}{\partial t} + \nabla\Gamma = F \tag{2-40}$$

By appropriately specifying the coefficient matrices (e_a, d_a, Γ, and F, where e_a is considered the mass matrix, d_a is the damping matrix, Γ is the flux matrix, and F is the source term), the COMSOL model can be used to represent the SMA phase fractions, its constitutive relationship, as well its heat transfer dynamics. After converting the constitutive relationships into specific volume form, the coefficient matrices are:

$$e_a = 0$$

$$d_a = \begin{bmatrix} 0 & 0 & 0 & 0 \\ 0 & 1 & 0 & 0 \\ 0 & 0 & 1 & 0 \\ 0 & -\rho_{sma}H & -\rho_{sma}H & \rho_{sma}c_v \end{bmatrix}$$

$$\Gamma = \begin{bmatrix} \sigma(t) & 0 & 0 & 0 \\ 0 & 0 & 0 & 0 \\ 0 & 0 & 0 & 0 \\ 0 & 0 & 0 & -kT(t) \end{bmatrix}$$

$$F = \begin{bmatrix} 0 \\ -x_+ p^{+A} + x_A p^{A+} \\ -x_- p^{-A} + x_A p^{A-} \\ (-hA\Delta T + J)/(A_c L_{sma}) \end{bmatrix}$$

The state variables in equation are

$$u = \begin{bmatrix} u_x(t) \\ x_+(t) \\ x_-(t) \\ T(t) \end{bmatrix}$$

In these matrices, $u_x(t)$ represents axial displacement of the SMA wire, k is its conduction heat transfer coefficient, A_c is its cross-sectional area, and ρ_{sma} is its density. The stress $\sigma(t)$ is given by equation (2-34).

In addition to these model equations, appropriate boundary conditions must be specified in COMSOL for phase fractions and temperature.

2.3.3 Model calibration/sensitivity

As well as for the other models, also for the MAS one, a sensitivity study has been performed to understand the role of the material parameters and their influence on results. Also in this case, the sensitivity analysis has been carried on a pseudoelastic tensile test. this is useful not only to calibrate the model, but also to determine the order of influence of parameters on the results. Since the experimental characterization of material parameters can be delicate, accept the use of literature or less refined data for parameters that have less influence on the results might be an advantage.

The first observation has to be done on the period imposed to loading cycle. Since the analysis is time-dependent, this influences also the results. Figure 2-24 illustrates the result for the simulation of a quasi-static tensile test lasting 10 minutes, and fast tensile test completed in 6 s and 60 s. As can be seen, the quasi-static test displays the single–crystal behavior with net nucleation and propagation. On the contrary, the other test shows the known effect of self-heating: since the rate at which the heat is generated within the sample is higher than the one for thermal dissipation, the test results non isothermal and the transformation stress changes as a consequence.

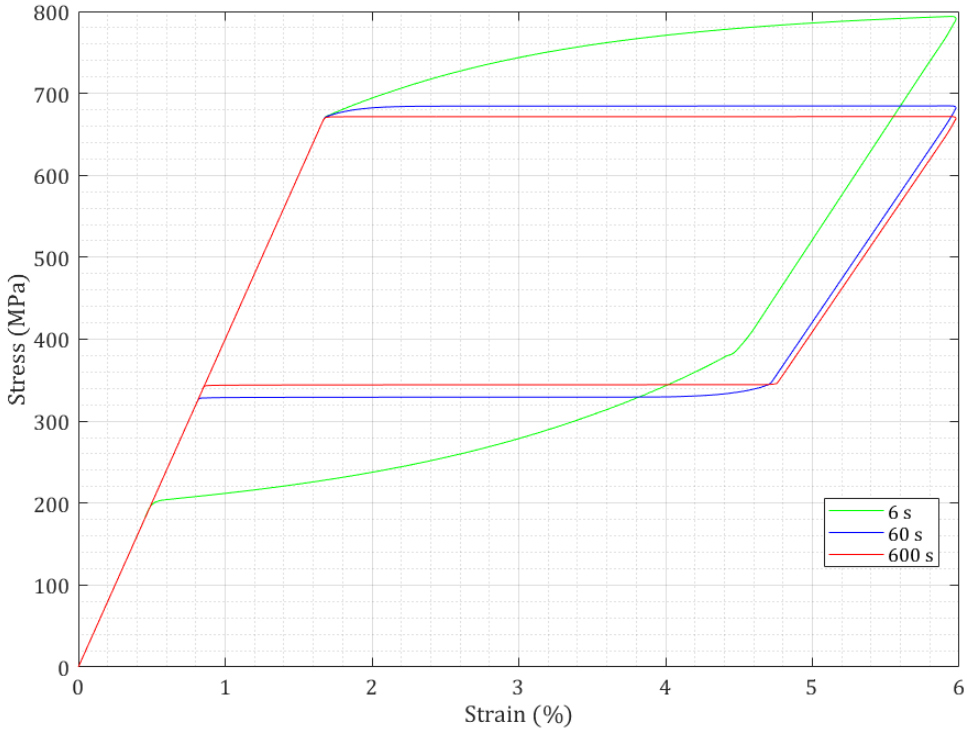

Figure 2-24 - Mechanical SS cycle with different period.

As for the maximum transformation strain, it suffers of the same effect seen in the Lagoudas model (Figure 2-25 and Figure 2-15). Increasing the value of the transformation strain, the slope of the plateau decreases. In Figure 2-26 the value of the displacement control has been stopped at 8% strain, for this reason the curves for the last two values of ε_T do not include the final elastic part.

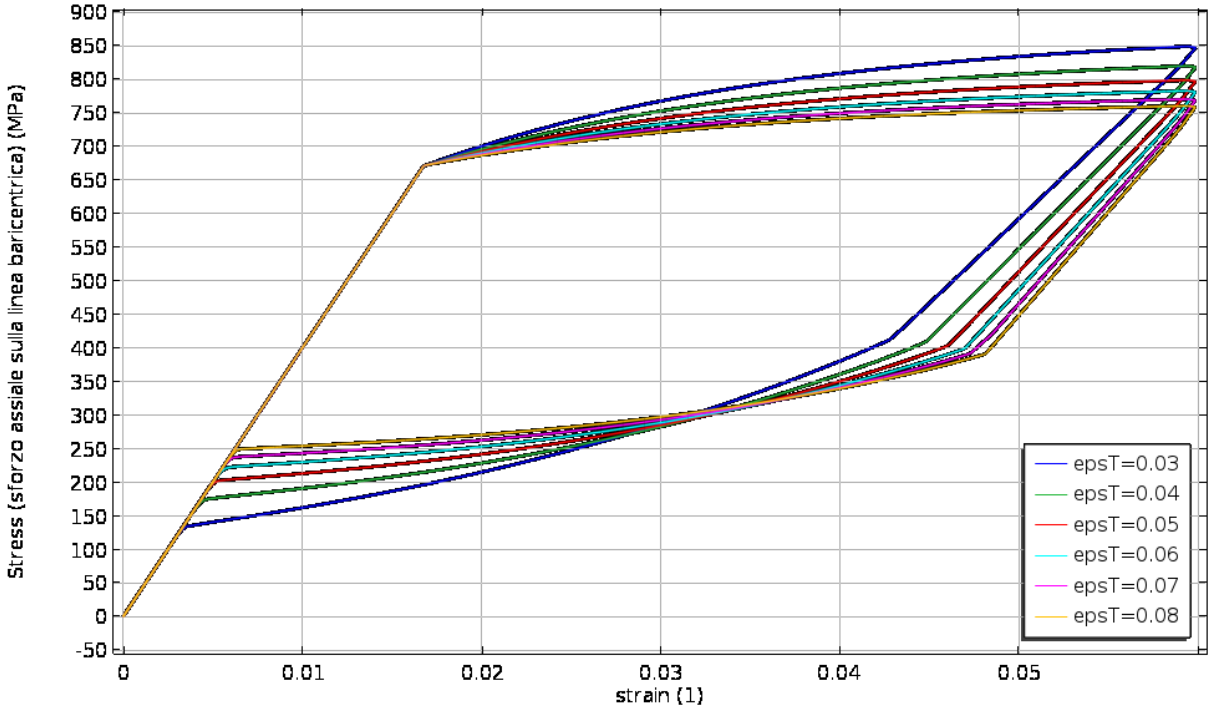

Figure 2-25 - Sensitivity to the maximum transformation strain ε_T at 105°C

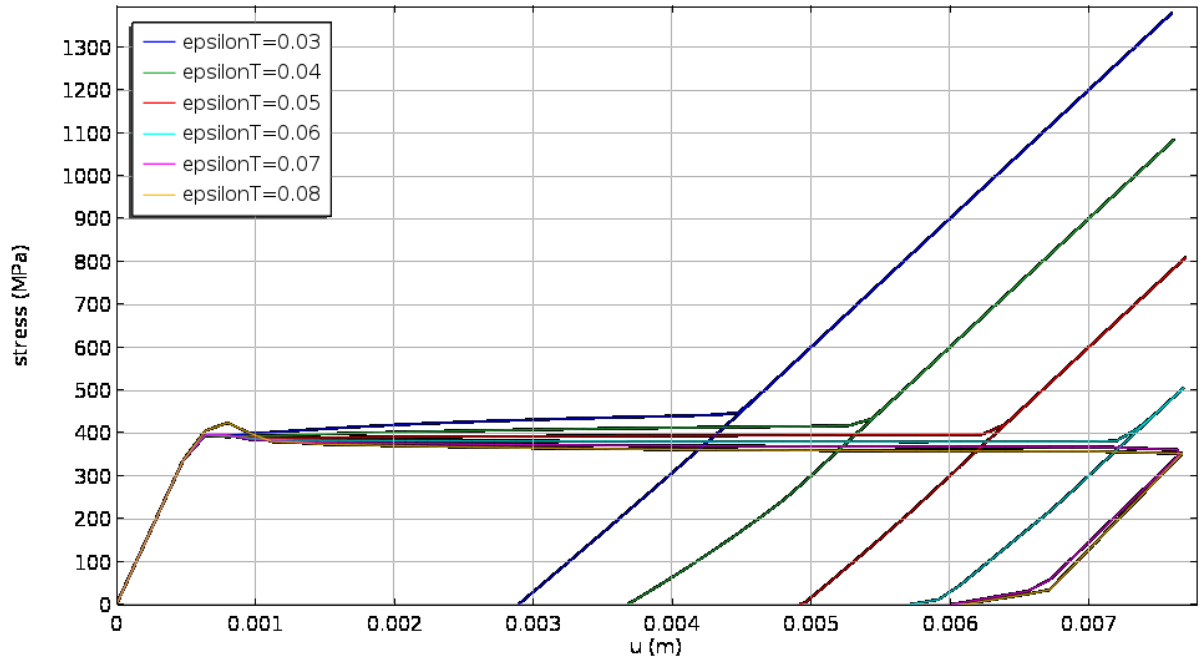

Figure 2-26 - Sensitivity to the maximum transformation strain ε_T at 25°C

Regarding the latent heat, it correctly influences the slope of the plateaux for the same reason of self-heating previously discussed. The error in determine experimentally this parameter can be of the order of

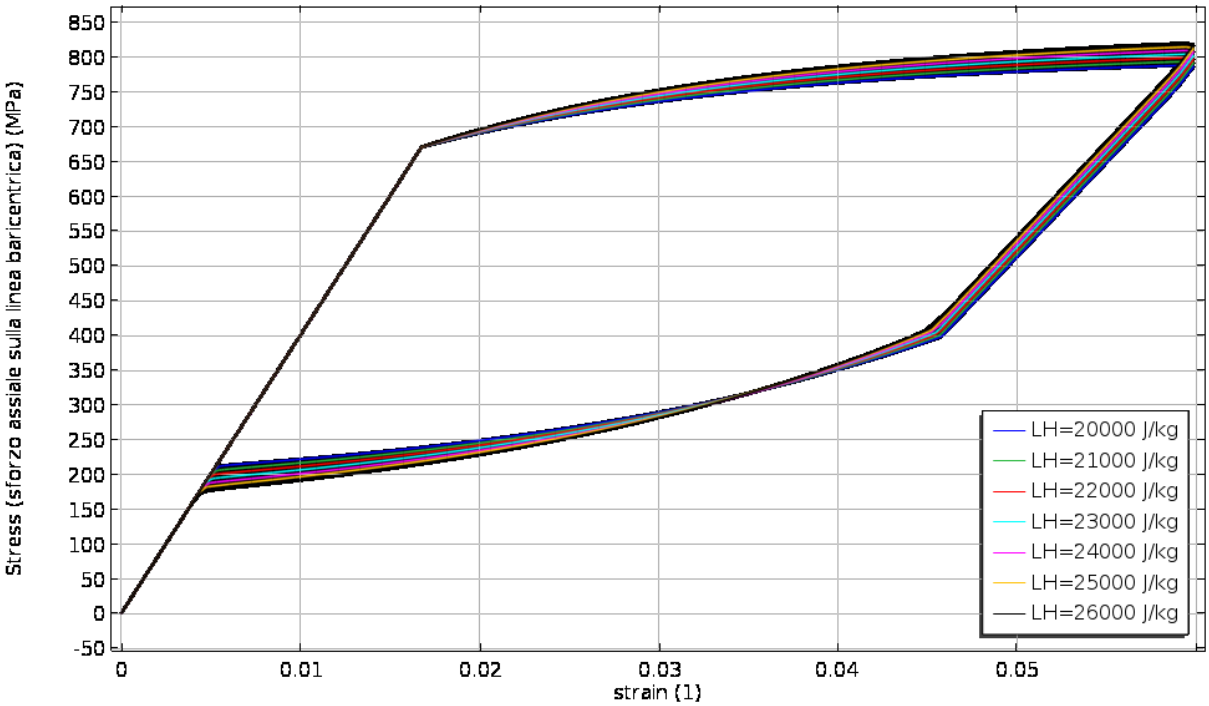

Figure 2-27 - Sensitivity to the latent heat

2.3.4 Model validation on tensile test

The two temperatures (105°C and 25°C) are imposed as ambient temperatures. To compare with the simulations with the Lagoudas model, the same type of wire has been considered. For these simulations, the quasi-static case has been used since the experimental tests are performed at 0.5 %/min strain rate. The maximum control strain is 6.5 %, then the test lasts 13 minutes. As a consequence, with respect to the analysis with Lagoudas model, the cycle results much more squared. It has to be noticed that this model is ideated for a single crystal, then this is fully justified. Also in this case the model does not catch the residual strain and it is not expected to be inserted as an additional parameter.

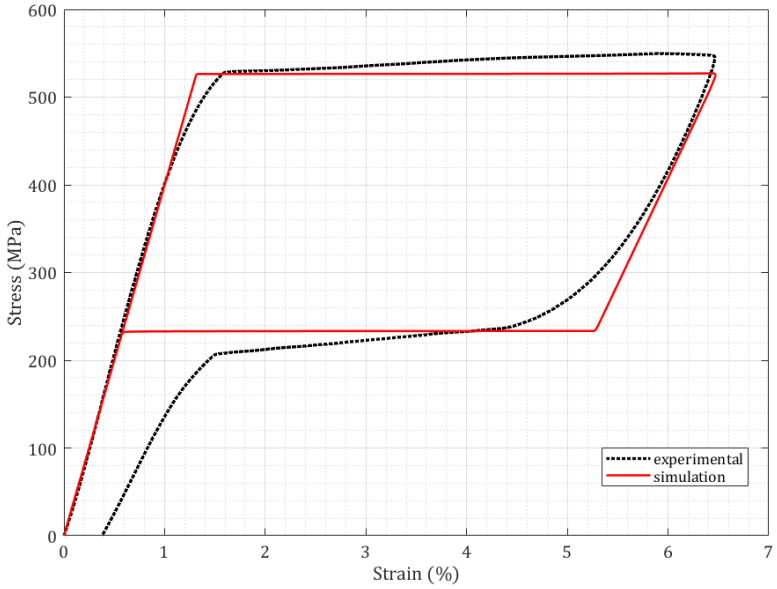

Figure 2-28 - Result of the Comsol analysis (red line) vs. experimental result (dotted black line) for the test at 105°C

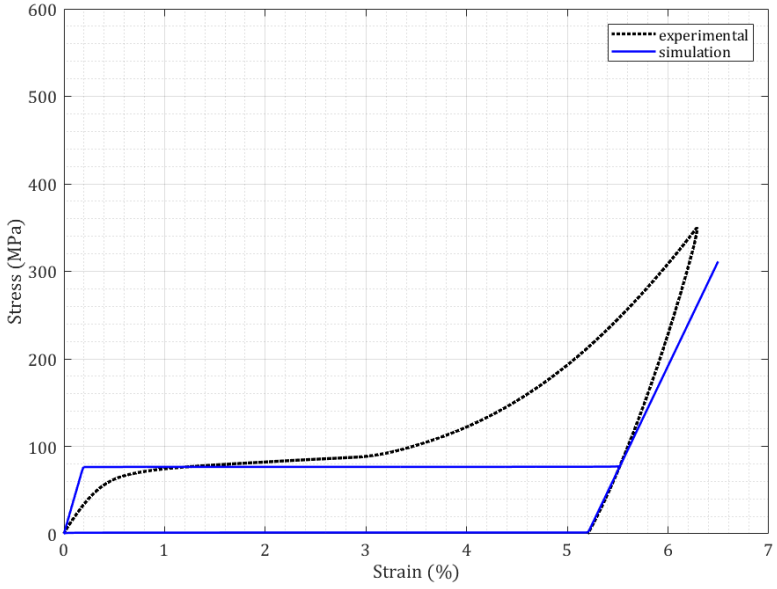

Figure 2-29 - Result of the Comsol analysis (blue line) vs. experimental result (dotted black line) for the test at 25°C

References

Achenbach M., Atanakdvic T., Muller I., 1986. A Model for Memory Alloys in Plane Strain. Int. J. Solids Struct. 22, 178–193.

Achenbach M., Müller I., 1985. Simulation of material behaviour of alloys with shape memory. Arch. Mech. 37, 573–585.

Achenbach M., Müller I., 1982. A model for shape memory. J. Phys. Colloq. 43, C4--163-C4--167. doi:10.1051/jphyscol:1982418

Bo Z., Lagoudas D.C., 1999. Thermomechanical modeling of polycristaline SMAs under cyclic loading, Part I: theroretical derivations. Int. J. Eng. Sci. 37, 1089–1140.

Boyd J.G., Lagoudas D.C., 1996. A thermodynamical constitutive model for shape memory materials. 1: The monolithic shape memory alloy. Int. J. Plast. 12, 805–842.

Brinson L.C., 1993. Dimensional Constitutive Behavior of Shape Memory Alloys: Thermomechanical Derivation With Non-Constant Material Functions and Redefined Martensite Internal Variable. J. Intell. Mater. Syst. Struct. 4, 229–242. doi:10.1177/1045389X9300400213

Chan C.W., Chan S.H.J., Man H.C., Ji P., 2012. 1-D constitutive model for evolution of stress-induced R-phase and localized Lüders-like stress-induced martensitic transformation of super-elastic NiTi wires. Int. J. Plast. 32–33, 85–105. doi:10.1016/j.ijplas.2011.12.003

Duerig T.W., Bhattacharya K., 2015. The Influence of the R-Phase on the Superelastic Behavior of NiTi. Shape Mem. Superelasticity 1, 153–161. doi:10.1007/s40830-015-0013-4

Heinen R., Miro S., 2012. Micromechanical modeling of NiTi shape memory alloys including austenite, R-phase, and martensite. Comput. Methods Appl. Mech. Eng. 229–232, 44–55. doi:10.1016/j.cma.2012.03.027

Helbert G., Saint-Sulpice L., Arbab Chirani S., Dieng L., Lecompte T., Calloch S., Pilvin P., 2014. Experimental characterisation of three-phase NiTi wires under tension. Mech. Mater. 79, 85–101. doi:10.1016/j.mechmat.2014.07.020

Ikuta K., Tsukamoto M., Hirose S., 1991. Mathematical model and experimental verification of shape memory alloy for designing micro actuator. Micro Electro Mech. Syst. 1991, MEMS '91, Proceedings. An Investig. Micro Struct. Sensors, Actuators, Mach. Robot. IEEE 103–108. doi:10.1109/MEMSYS.1991.114778

Lagoudas D., Hartl D., Chemisky Y., Machado L., Popov P., 2012. Constitutive model for the numerical analysis of phase transformation in polycrystalline shape memory alloys. Int. J. Plast. 32, 155–183.

Lagoudas D.C., Bo Z., Qidwai M.A., Entchev P.B., 2003. SMA_UM: User Material Subrotine for Thermomechanical Constitutive Model of Shape Memory Alloy 1–18.

Lexcellent C., Tobushi H., Ziolkowski A., Tanaka K., 1994. Thermodynamical model of reversible R-phase transformation in TiNi shape memory alloy. Int. J. Press. Vessel. Pip. 58, 51–57. doi:10.1016/0308-0161(94)90007-8

Liang C., Rogers C.A., 1997. One-Dimensional Thermomechanical Constitutive Relations for Shape Memory Materials. J. Intell. Mater. Syst. Struct. 8, 285–302. doi:10.1177/1045389X9700800402

Miyazaki S., Otsuka K., 1986. Deformation and Transition Behavior Associated with the R-Phase in Ti-Ni Alloys. Metall. Trans. A 17, 53–63. doi:10.1007/bf02644442

Morin C., Moumni Z., Zaki W., 2011. A constitutive model for shape memory alloys accounting for thermomechanical coupling. Int. J. Plast. 27, 748–767. doi:10.1016/j.ijplas.2010.09.005

Müller I., Seelecke S., 2001. Thermodynamic aspects of shape memory alloys. Math. Comput. Model. 34, 1307–1355.

Nespoli A., Rigamonti D., Riva M., Villa E., Passaretti F., 2016. Study of pseudoelastic systems for the design of complex passive dampers: static analysis and modeling. Smart Mater. Struct. 25, 105001. doi:10.1088/0964-1726/25/10/105001

Olbricht J., Yawny A., Pelegrina J.L., Dlouhy A., Eggeler G., 2011. On the stress-induced formation of R-phase in ultra-fine-grained Ni-rich NiTi shape memory alloys. Metall. Mater. Trans. A Phys. Metall. Mater. Sci. 42, 2556–2574. doi:10.1007/s11661-011-0679-y

Qidwai M.A., Lagoudas D.C., 2000. On thermomechanics and transformation surfaces of polycrystalline NiTi shape memory alloy material. Int. J. Plast. 16, 1309–1343. doi:10.1016/S0749-6419(00)00012-7

Rigamonti D., Nespoli A., Villa E., Passaretti F., 2017. Implementation of a constitutive model for different annealed superelastic SMA wires with rhombohedral phase. Mech. Mater. 112. doi:10.1016/j.mechmat.2017.06.001

Sedlak P., Frost M., Benesova B., Ben Zineb T., Sittner P., 2012. Thermomechanical model for NiTi-based shape memory alloys including R-phase and material anisotropy under multi-axial loadings. Int. J. Plast. 39, 132–151. doi:10.1016/j.ijplas.2012.06.008

Seelecke S., Müller I., 2004. Shape memory alloy actuators in smart structures: Modeling and simulation. Appl. Mech. Rev. 57, 23. doi:10.1115/1.1584064

Sun Q.P., Hwang K.C., 1993. Micromechanicsl modeling for the constitutive behavior of polycrystalline shape memory alloys - II. Study of the individual phenomena. J. Mech. Phys. Solids 41, 1–17.

Tanaka K., 1986. Thermomechanical Sketch of Shape Memory Effect: One-Dimensional Tensile Behavior. Res Mech. Int. J. Struct. Mech. Mater. Sci. 18, 251–263.

Wang X., Verlinden B., Van Humbeeck J., 2015. Effect of aging temperature and time on the transformation behavior of a Ti-50.8 at.% Ni alloy with small grains, in: Materials Today: Proceedings. pp. S565–S568. doi:10.1016/j.matpr.2015.07.348

Zheng Y., Jiang F., Li L., Yang H., Liu Y., 2008. Effect of ageing treatment on the transformation behaviour of Ti–50.9at.% Ni alloy. Acta Mater. 56, 736–745. doi:10.1016/j.actamat.2007.10.020

Zhu S., Zhang Y., 2007. A thermomechanical constitutive model for superelastic SMA wire with strain-rate dependence. Smart Mater. Struct. 16, 1696–1707. doi:10.1088/0964-1726/16/5/023

Chapter 3
COMPARATIVE ANALYSIS BASED ON APPLICATIONS

In previous chapter, numerical finite element simulations of simple uniaxial tests have been used to study three different approaches to SMA constitutive modeling and to highlight the sensitivity of the three models to their distinctive parameters. Here, a comparative analysis of the same three constitutive models is conducted based on as many different applications.

The first model (Tanaka modified) is used to study the parallel system of NiTi pseudoelastic wires, developed in collaboration with CNR-ICMATE, to analyze the possibility of tailoring the absorbed mechanical energy, coupling different types of wires.

The second one (Lagoudas phenomenological) is applied to the case of a device designed to shrink radially a compliant silicone pipe, by means of a single shape-memory NiTi wire bounded on its circumference. The comparison between numerical predictions and experimental data are available from a prototype of the actuator realized in the laboratories of the DAST in Milan, this allows to validate quantitatively the models and to demonstrate their reliability.

The last one (MAS model) is used to simulate a linear actuator consisting of a SMA wire bending a flexible beam to which is externally constrained with stiff aluminum stubs. The validation results for this application are taken from (Yang and Seelecke, 2009) and with few modifications can be adapted to the study of the bending of fiber–reinforced composite panels with polymeric matrix.

3.1 Pseudoelastic system for passive damping

The designed system for this application is constituted by a metallic sliding shaft on which three metallic disks are mounted: the central one is fixed in the middle of the shaft, while the others occupy an adjustable position. The assembly is then coupled to a metallic cage.

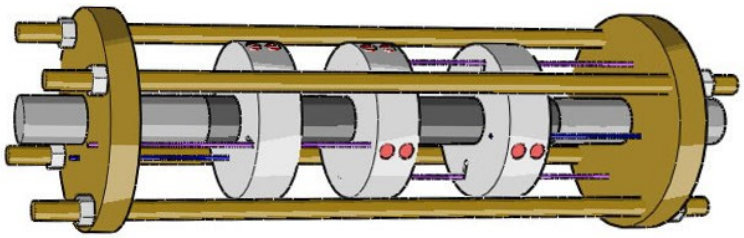

Figure 3-1 - Assembly of the damping system, mounting parallel wires

Between the fixed disk, the two mobile ones and the extremes of the cage, four groups of pseudoelastic wires working in a parallel configuration are installed. The fours groups work coupled two by two: while the two groups one side of the fixed disk are pulled, the other are compressed and vice versa. Considering a couple of groups on one side working in traction, the distance of the fixed and mobile disks from the extremity of the cage identify the lengths l1 of group 1 and l2(<l1) of group 2 respectively. Thus, the two groups 1 and 2 of wires with different adjustable length work in parallel in tensile configuration. This allows studying the effect of changing the lengths and the type of the wires. Standard tensile tests in different configurations were accomplished to evaluate the global damping capacity, the energy dissipated per cycle and the maximum attenuated force in a static condition. The numerical model was implemented to predict the damping response of more complex pseudoelastic arrangements.

As an example, the two materials cited in Chapter 2 are considered, treated one at 450 °C (HT wire) and the other at 320 °C (LT wire).

The system of two groups of NiTi wires, one HT and the other LT, arranged in parallel tensile configuration has been tested and compared with the coupled simulation. This last is realized by creating a single control law in displacement and by running, at each integration step, the two models (HT and LT) and summing the forces of the two. Figure 3-2 shows the results of this simulation, compared with experimental trends, for four different test temperatures in pseudoelastic range.

The model of the two wires in parallel is globally good for temperatures below the peak of R transformation, while it tends overestimating the stress for the two higher temperatures. The area of the hysteresis cycle is however well represented in all the cases. Looking more in detail, at 23 °C there is a peak in the end of the plateau, which is observed experimentally from the second cycle. The simulation does not represent at all this peak remaining consistent with individual wire tests. Moreover, in the unloading part of the experimental tests, two points of transformation start can be noticed (particularly for two tests: at 2 % and 0.8 % for 34 °C, and at 1.8 % and 0.5 % for 50 °C). These are probably due to the beginning of the transformations R to A at different strains for the HT and for the LT. Compared to individual wires, these have been set at 1 % (HT) and 1.2 % (LT), then there is no correspondence with the percentage seen in the coupling.

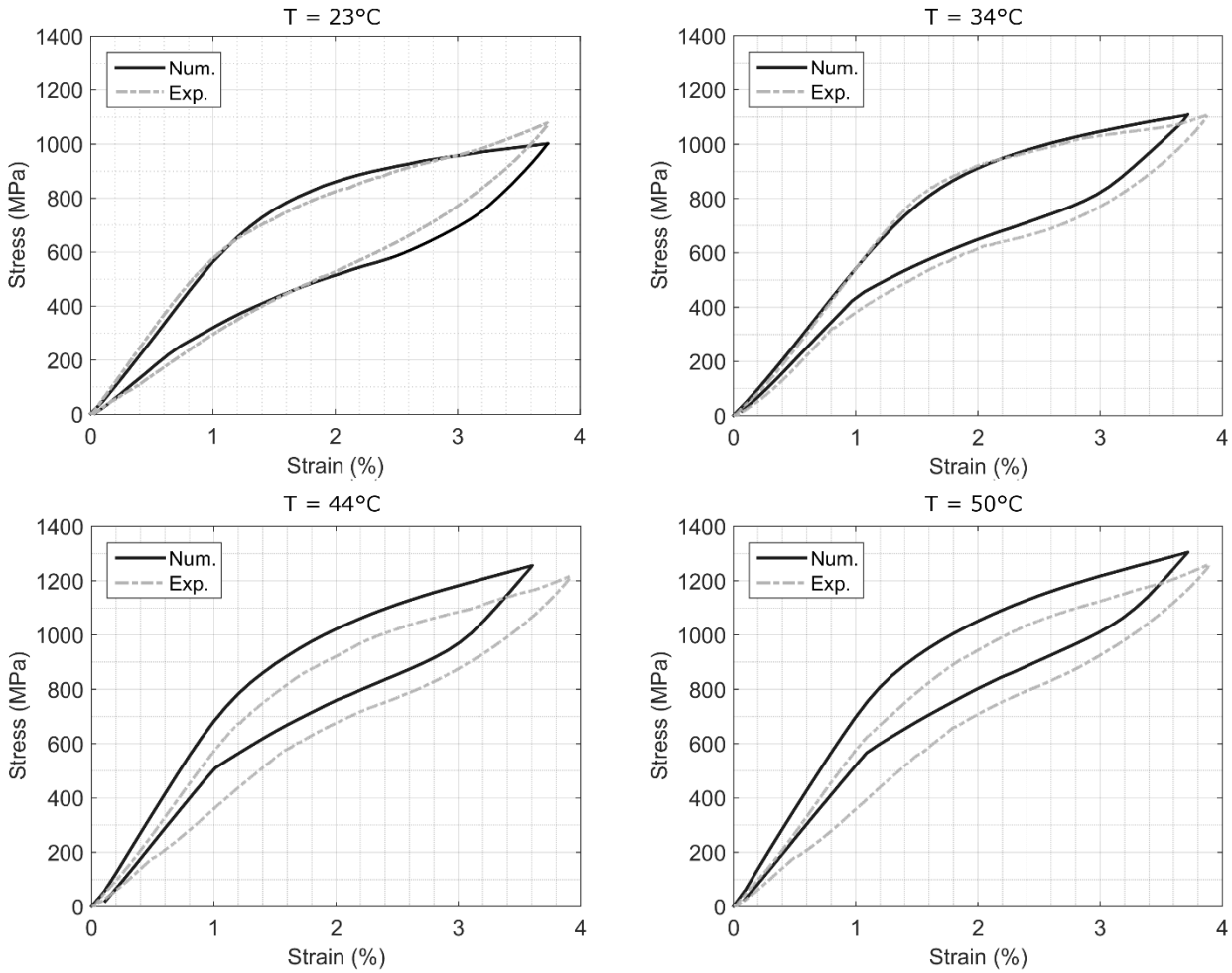

Figure 3-2 - Tests on coupled wires. Comparison of experimental vs. simulation trends, for four different test temperatures.

Because of the approach used to realize numerically the coupling, it represents exactly the linear combination of the two wires taken individually. Since the simulation confirms the experimental results, this means that the linear superposition of two wires in parallel is a proven result. Then, once tailored the model on the individual sample, the coupled behavior might be foreseen only by the simulation, which can be used as a predictive tool for the design of possible applications.

As mentioned in the introduction, since the Tanaka model thus formulated is able to simulate only the pseudoelastic behavior, it is not possible to design an actuation application with this model. It has been presented because its implementation is simple and allows various adjustments, but its application is not deepened further here. For more details, the reader is referred to (Nespoli et al., 2016).

3.2 Actuation system for radial shrinking

The benchmark case chosen for the Lagoudas model is an application of NiTi wires as actuators for pipe radial shrinking. A device is designed to shrink radially a compliant silicone pipe in which gas or liquid flows, by means of a single shape-memory NiTi wire bounded on its circumference: the goal is to convert the linear contraction of a heated SMA wire into a radial displacement (Borlandelli et al., 2015). Then, a sequence of these devices is placed alongside the tube to form a combined system in which each of them acts synchronized, that has been originally conceived to create peristaltic traveling waves inside the tube. Numerical simulations in an idealized setup suggested that a turbulent wall flow could be transformed into fully laminar by this type of forcing. This would allow a drag reduction, which would correspondingly lead to a reduction in parasitic power. This is the foundation of the experimental application and causes requirements that are:

- the minimum amount of linear deformation at 8% on the pipe diameter;
- the actuation frequency whose ideal value is 5 Hz, but can be relaxed to 1 Hz;
- the minimum distance between two actuators to fit the wave.

The second of these requirement lead to strict conditions of thermal control, especially because fast actuation brings to shorten the cooling time of the periodic actuation and consequently the wire warm up gradually as the cycles increase, reducing the shrinking performance to a regime condition.

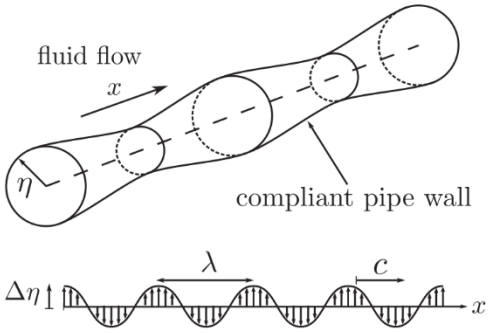

Figure 3-3 - Sketch illustrating the geometry of a pipe flow with peristaltic waves. The fluid flow is toward the positive x direction.

Figure 3-3 schematizes the travelling of a peristaltic (deformation) wave along the x-axis of a circular duct delimited by deformable walls. The wave is characterized by maximum peak-to-peak displacement $2\eta_{max}$, wavelength λ and phase speed c. Each wall point experiences a displacement $\Delta\eta\,(x, t) = \eta_{max} \sin(2\pi\,\lambda\,(x - ct))$.

Nonetheless, the aim of this chapter is not the accurate simulation of the real experimental conditions, and then some simplifications are made on the model, discounting the requirement for periodic actuation and the consequent thermal control. In the simulation, SMA wire is allowed to carry out a complete transformation, from room temperature to above Af and backward. This limits the comparison between the results of the numerical analysis and those of the experiment, because the latter never allow such a condition during running stabilized cycles (actually, the wire never returns to ambient temperature). Indeed, for the comparison, the only shrinking results used are those of the first cycle, which is the only one during which complete transformation takes

place. Another aspect that could not be experimentally validated is thermal exchange with the surrounding environment because the SMA thermal profile is not known during the test and the cooling conditions were not perfectly controlled. For this reason, the thermal exchange with the environment was not considered in the simulation and so it would have been inconsistent to simulate the Joule effect. In view of this, actuation has been achieved by a temperature condition imposed on the SMA part/domain.

3.2.1 Components of the system

The object on which the actuator acts is a silicone pipe (material acronym: 50 shore A) with internal diameter Di = 40 mm and thickness t = 3 mm. The internal pressure is set at 0.4 bar. The requirement for the actuator to shrink the pipe achieving a linear deformation on the diameter at least equal to 8 % becomes then a 3.2 mm reduction, i.e. a 1.6 mm displacement of the pipe wall.

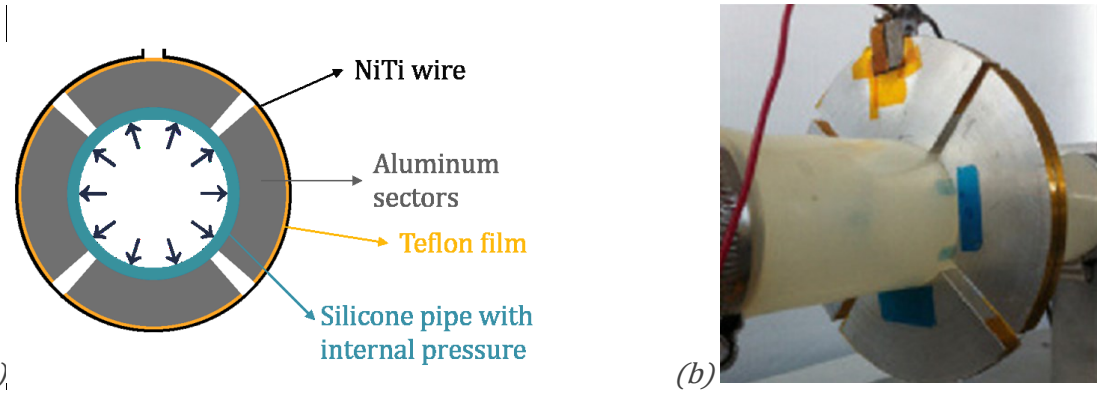

Figure 3-4 - Configuration of the actuation device: scheme (a) and picture (b)

The core of the actuation device is the structure that supports the SMA wire. This is a group of four rigid circular sectors made of aluminum, which leans along the pipe circumference and provides the required NiTi wire housing. The configuration with separate sectors allows themselves to slide over the pipe wall during the movement so that they move close during the actuation and move away during rearm. The goals of this structure are:

1) to supply a housing for the SMA wire;
2) to geometrically amplify the wire contraction ;
3) to act as a heat sink to dissipate the thermal energy of the wire during the cooling phase.

The first is obtained providing the sectors with a groove in the middle of their external surface on which the wire is wrapped. A thin Kapton layer (60 μm) is placed between aluminum and wire to provide electrical insulation. The groove diameter is chosen to maximize the contact surface between Kapton and the wire. On top, a shaped block of Teflon is inserted in the middle of a sector, to provide the mechanical fastening for the clamped tips of the wire and for the electrical contacts. Moreover, the sectors are supported by a global structure to prevent both tilt from vertical and slide due to gravity.

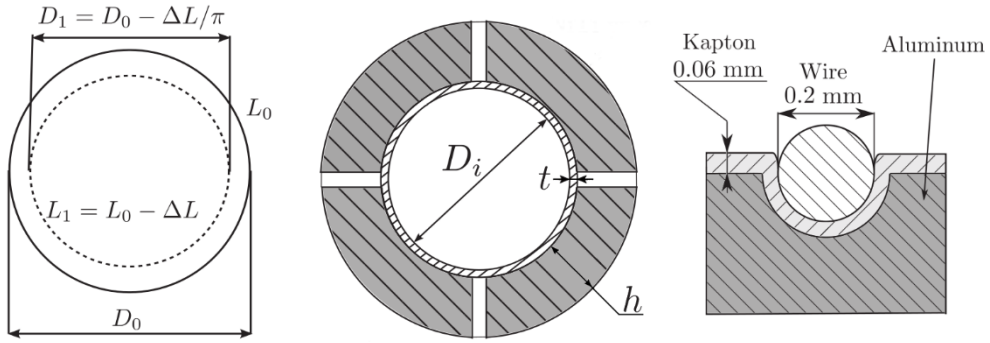

Figure 3-5 - Cross-section of the grooved interface between the SMA wire and the actuator.

The requirement regarding deformation on the diameter of the pipe is 8%. Although a SMA wire can ideally recover this strain amount, the best durability condition settles around 4%. Therefore, sectors assure also that the axial deformation of the wires is amplified to the required deformation on the pipe. The height h of the sectors can be calculates starting from the deformation of the wire:

$$\varepsilon_{SMA} = \frac{L_1 - L_0}{L_0} = \frac{(D_1 - D_0)/D_0}{\frac{2h}{D_0} + 1} \tag{3-1}$$

Fixing the deformation of the wire at 3%, the geometrical amplification leads to a dimensioning of the height of the sectors of 30 mm, which corresponds to an external radius of 53 mm. For the reference application, four to five actuators need to be side by side in a wavelength of 40 mm to generate correctly the wave, that is, one every 10 mm. The sectors are thus 6 mm thick and spaced apart by 4 mm between each other.

The wire adopted is a Smartflex (SAES Getters) NiTi (49-51 at.%) SMA, 0.2 mm diameter, which is the same calibrated in Chapter 2. The transformation temperatures are:

- $M_F = -17.6°C$
- $M_S = +13.8°C$
- $A_S = +60.6°C$
- $A_F = +75.1°C$

The actuator works at room temperature, which is between M_S and A_S, in SME configuration. In this case, the load is given only by the internal pipe pressure, so its value must be enough to rearm the wire (i.e. produce the SIM transformation) but not too high to oppose to shrinking.

3.2.2 Mounting the system

From Equation (3-1), the length at which the SMA wire has to be cut is L_0: this will be the "memorized" length. The wire is then stretched up to 3% (pulling it straight and then wrapped around the sectors on the pipe, which is then inflated at the operating pressure. Concluded the mounting phase, the activation takes place: the SMA wire, heated by Joule effect, is subject to the transformation that takes it back to the austenite phase, producing the uniform shrinkage desired. Then, decreasing the temperature, the wire returns to the martensitic phase. The strength falls, so the internal pressure and the elastic return of the rubber are enough to rearm the SMA and the

pipe returns to its inflated diameter. From here onwards, the cycles of heating and cooling alternate, producing the actuation frequency.

The complete device is composed by a series of actuators, but this analysis is limited to a single pipe-sectors-wire assembly.

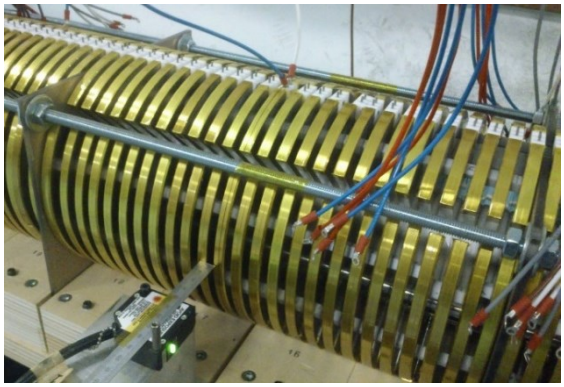

Figure 3-6 - Sequence of actuators in the experimental setup

3.2.3 FEM model

Geometry

The first part of the geometry consists of the pipe with internal diameter 40 mm, thickness 3 mm and length 300 mm, bounded at the extremities with two metal clamps. Due to the ratio between the thickness and the other dimensions, shell elements have been chosen. In particular, the element type in Abaqus is S4R (general-purpose conventional shell element with four nodes (quadrilateral) and reduced integration). Because all the loads and boundary conditions are symmetrical to the vertical middle plane of the equipment, this part is sketched through a shell extrusion of the mean plane of half pipe wall.

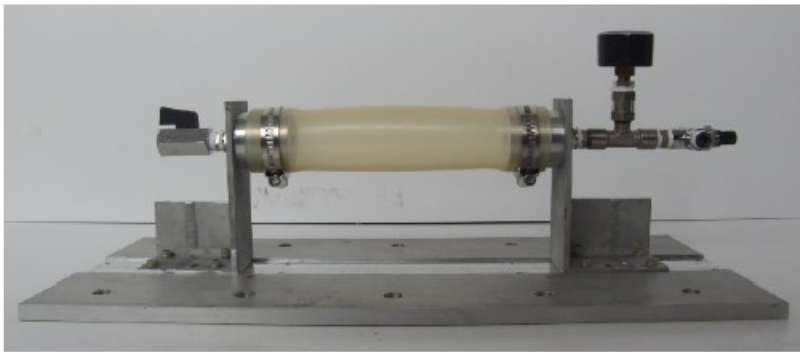

Figure 3-7 - Picture of the pipe with its support equipment

Leaning against the pipe, is the second part made by the aluminum sectors with height 30 mm, thickness 6 mm and separated on the circumference by a 10 mm arc, whose dimensioning is reported in previous chapter. The sectors dimension ratio is greater than 1/10 so it is meshed with solid elements and is consequently solid sketched, respecting the same symmetry of the previous part. The element type is C3D8R (three-dimensional continuum linear brick, with eight nodes and reduced integration). Modeling this part with solid elements gives also an advantage providing a surface, which can be a master for the contact definition both for shell and beam elements.

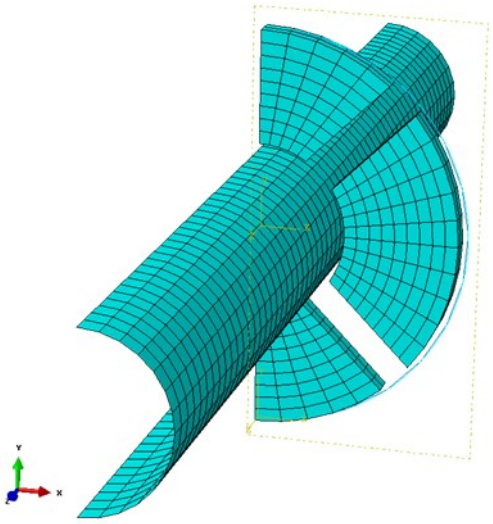

Figure 3-8 - Assembly

Finally, on the external circumference of the sector, the wire is sketched as a line through its central axis that is located at a radius of 53.1 mm. Although not essential for the purposes of the model, also the missing portion of wire, equal to 3.5 mm per part (considering symmetry), on the top was included to have the identical length of the wire with respect to the analytical calculation of the estimated strain percentage. The element type is B33 (Euler-Bernoulli beam in space, with cubic formulation). These elements do not allow for transverse shear deformation (plane sections normal to beam axis remain plane and normal to the axis); for beams made of uniform material, typical dimensions in the cross-section should be less than about 1/15 of typical axial distances (e.g. the distance between supports) for transverse shear flexibility to be negligible. In this case, the diameter/length ratio respects this assumption. During assembly, by fixing the ends with crimped terminals and bending the wire to form an arc, moment has shown to be partly transmitted by the wire, so beam instead of truss elements have been selected.

Steps

Sketching the parts already in contact creates problems of contact interference between parts themselves; therefore, a first static, general step that simulates the mounting has been defined. In this step, the wire is rigidly rotated (defining a displacement/rotation boundary condition, arbitrary UR3= 0.035 radians) to bring it into contact with the surface of the sectors. Being assigned a rigid rotation, the pipe is not pushed and it is therefore not necessary to define an initial inflation.

The second static, general step represents the clamping of the tip of the wire and the inflating of the pipe at the operative pressure 0.4 bar. Clamping has been modeled in the simplest way possible, i.e. with a boundary condition that keeps constants the U1 displacements made in the first step, fix at zero the U3 displacement and allow free U2, UR1, UR2, UR3 degrees of freedom.

To close, the actuation step is achieved by a temperature condition imposed on the SMA part/domain through a predefined field. As explained, the thermal exchange with the environment was not considered in the simulation and so it would have been inconsistent to simulate the Joule effect.

Boundary conditions, loads and interactions

As already said, the symmetry of loads and boundary conditions of the system allows defining a symmetry condition on the longitudinal plane of the model (XSYMM, U1=UR2=UR3=0), which reduces the size of the model and smooths the convergence. The metal clamps that fix the pipe are modeled using a pin boundary condition. In real application, the sectors are prevented from rotating both in the case in which is mounted a single actuator and in the series of actuators side by side. In this second case, the devices are also supported by a metal equipment. To reproduce this situation a condition of no-tilt (U3=UR1=UR2=0) is assigned to the lateral surface of the sectors and another of no-slip (U2=0) is assigned to the nodes on the y-axis in the central sector (the one not bounded by symmetry). The node of the wire on the bottom has, in addition to symmetry, U3=0, while the node of the wire on top has the already described conditions of imposed rotation in the first step and clamping in the second step.

The only load is the pressure of 0.4 bar (40000 Pa) applied in the second step on the internal surface of the pipe.

A general contact interaction has been defined, with a global property that uses Abaqus default options for contact. For the master-slave assignment, the pairs defined are:

- external surface of the pipe-internal surfaced of the sectors
- external surfaces of the sectors-circumferential surface of the beam

The surface of the beam is not a valid master surface for contact, so in the second pair the assignment is obliged. In the first pair, the sectors are the rigid part between the two and so it is used as master surface in this case too.

Materials

The 8% shrinkage of the diameter corresponds to an absolute reduction value of 3.2 mm on the diameter, hence an expected displacement of the nodes of the pipe of 1.6 mm. Due to the small value of this displacement, it has been chosen to model the material of the tube only with its elastic properties. The elastic modulus has been calculated starting from the hardness value; using linear elastic indentation hardness, a relation between the ASTM D2240 hardness and the Young's modulus for elastomers has been derived by Gent (Gent, 1958) and has the form:

$$E = (0.0981 * (56 + 7.62336 * S))/(0.137505 * (254 - 2.54 * S)) \qquad (3\text{-}2)$$

E is the Young's modulus in MPa and S is the ASTM D2240 type 'A' hardness. With a 50 shore A value the modulus results 2.5 MPa.

The sectors are aluminum and the wire is defined following the SMA_UM subroutine requests as described in Chapter 2.

3.2.4 Results and comparison with experimental values

In the experiment, both the radial external displacement of the sectors and the internal wall deformation due to the peristaltic movement are independently measured. An external laser measuring system is employed to obtain the time history of the wall deformation. Simultaneously, an endoscopic camera synchronized with the actuation signal shoots two pictures, respectively at the end of heating and cooling phases. The displacement is then evaluated by picture graphic analysis thanks to markers of known size previously placed on the internal wall (Figure 3-9). The endoscopic measurements are used to validate the model results with the obtained shrinkage of the pipe wall.

When the wire is mounted in pre-deformed state, its recovery is up to 3%, so the first activation cycle results in a radial displacement of the inflated tube of 1.6 mm. In the subsequent rearm, the inner pressure of the tube is not enough to pre-deform the wire again to the same initial value, so the recovery of subsequent cycles is lower than and equal to 1.1 mm. In the model, this effect is not resembled, because the mounting is simulated with the length of the wire that already wraps the pipe. The simulation therefore has a radial pipe displacement equal to 1 mm, equal in both the first cycle and the second (Figure 3-10).

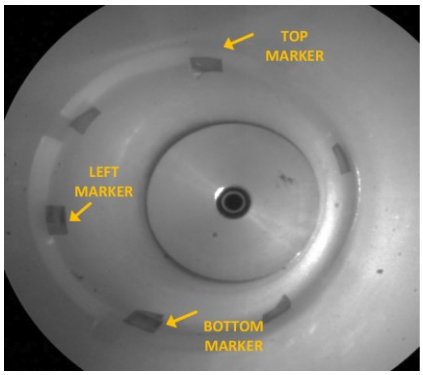

Figure 3-9 - Endoscopic acquisition

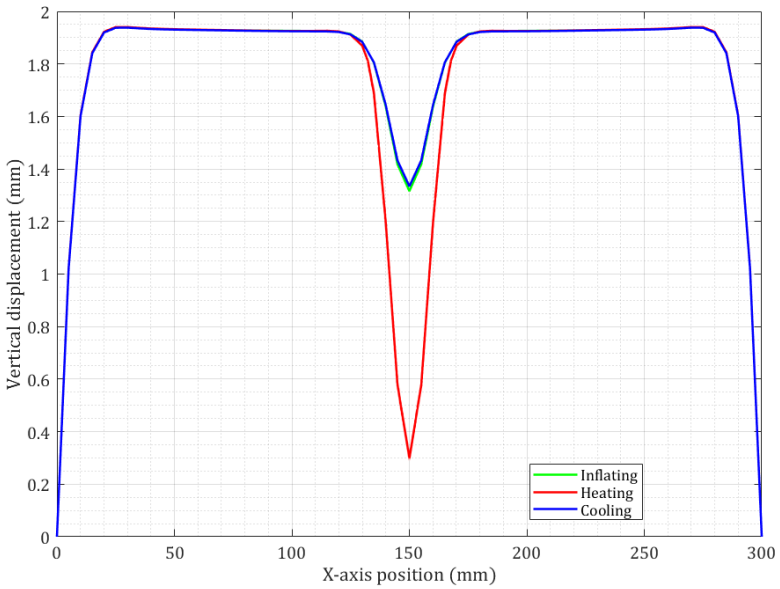

Figure 3-10 - Simulation results: displacement along longitudinal axis of the pipe.

To estimate the stress σ acting in the wire it has been assumed a simplified model in which the silicone stiffness is negligible. This assumption leads to the formula

$$\sigma = \frac{pD_i z}{\pi D_w^2/2},$$

where DW is the wire diameter, p is the internal pressure and z is the thickness of the sectors, which distributes on the wire the pressure due to the pipe expansion. The evaluation corresponds to a stress value around 200 MPa, which is the optimal stress for this type of SMA material.

From the model, the stress within the wire can be calculated at each point. Figure 3-11 shows the stress value in the wire along its length. During heating, the stress reaches the designed value of 200 MPa. Although scattered, the trend shows also that during martensite rearm, there is a stress concentration in the two free parts of the wires, not in contact with the sectors. On the contrary, there is a lower stress in the same portions during heating.

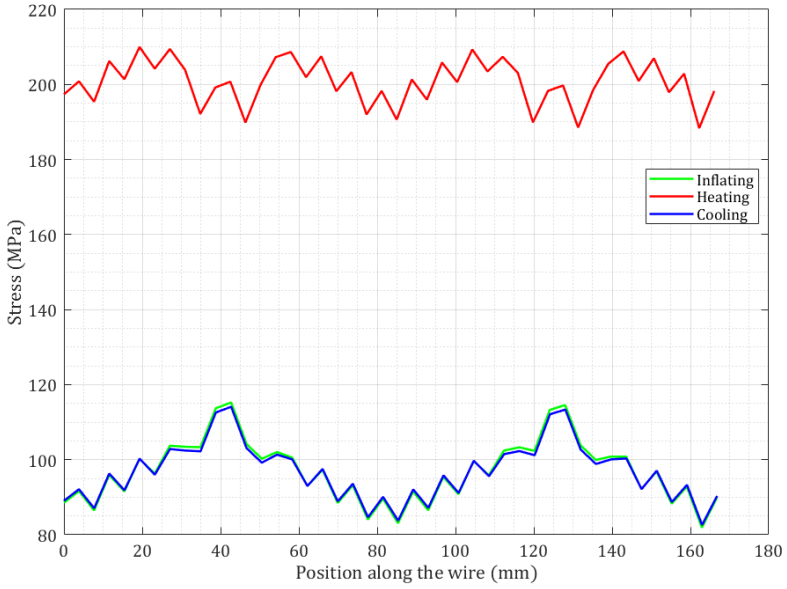

Figure 3-11 - Stress value in the SMA wire along its length

From the FEM we have also some information not obtainable from experiments:

- ✓ Radial displacement of the pipe in the free portion (maximum value of expansion due to pressure only) = 1.9 mm
- ✓ Radial displacement of the pipe in the middle section with the wire in martensitic state (expansion due to pressure, balanced by the elastic deformation of the martensitic wire) = 1.4 mm
- ✓ Distance of influence of the shrinkage action (longitudinal distance from the middle section at which the radial displacement is equal to the maximum one) = 30 mm

3.3 Bending of plane beam

The last case of application is studied with the MAS model. This is the case of a linear actuator consisting of a SMA wire bending a flexible beam to which is externally constrained with stiff aluminum stubs (Figure 3-12). This can represent a usual condition of actuation of aeronautic panels for morphing (Ameduri et al., 2012; Barbarino et al., 2014; Concilio and Lecce, 2014) and has been selected for this reason. In this case, there is not an experiment that can be used to validate the model and then results from (Yang and Seelecke, 2009). This paper studies the bending of a beam made of thermoplastic, but can be easily adapted to the study of the bending of fiber–reinforced composite panels with polymeric matrix with few modifications.

3.3.1 FEM model

The model is implemented in a 2D environment. The compliant structure is made by a beam of thermoplastic material 85 mm long. The cross section is 20 x 1 mm and is applied as a property of the beam. Similarly is made for the aluminum stubs, which are 10 mm long with a 2.5 x 2.5 mm cross section.

The geometry of this model is very simple and the tricky part lies in the coupling of the SMA model with the structure. As already described in Chapter2, The SMA component is solved through a set of PDE equations. In order to catch the 2D behavior and to couple the SMA wire actions with Comsol Structural Mechanics Module, different strategies can be adopted, but the most performing is to model the wire as a Truss and couple the variables of the truss with the ones from the PDE.

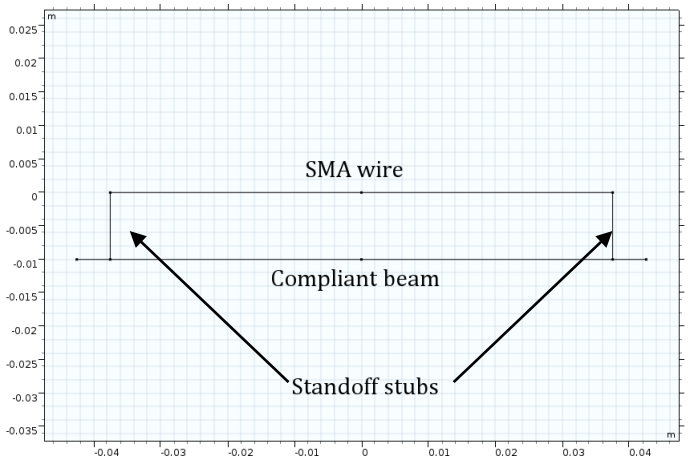

Figure 3-12 - Geometry of the model

Following this approach, the PDE system presented in Chapter 2 has to be implemented without the equation relative to variable “u” (displacement). Since the dimension of the model is 2D, the system has to be imposed as “boundary” PDE to be applied to a line. Then, the SMA wire (length 75 mm and diameter 0.05 mm) has to be added as a truss on the same boundary. Then, to couple mathematics and structural physics, strain and stress SMA variables has to be set as the axial deformation in the barycenter line (truss.en) and as Second Piola–Kirchhoff axial stress (truss.Sn), respectively. By comparing SMA's stress-strain relationship (Equation (3-3)) with the

material law applied by Comsol (Equation (3-4)), it is also possible to identify the elastic modulus and the initial strain to be applied to the truss so that the SMA material can be implemented.

$$\sigma(t) = \frac{\varepsilon(t) - \varepsilon_T\big(x_+(t) - x_-(t)\big)}{x_A(t)/E_A + \big(x_+(t) + x_-(t)\big)/E_M} \tag{3-3}$$

$$N = EA\left(\frac{du}{dx} - \alpha\big(T - T_{ref}\big) - \varepsilon_{ni}\right) + N_i \tag{3-4}$$

The elastic modulus is the weighted sum of the moduli with the Reuss average formulation (denominator in Equation (3-3)). The initial axial deformation ε_{ni} can be applied to the truss as a sub-option of the elastic material property and results equal to $\varepsilon_T\big(x_+(t) - x_-(t)\big)$. In addition to these assignments, the equation solving the truss physics has to be put in stationary form, because the transient solution is already comprised in the PDE formulation.

The mounting step can avoided, because the result of wire pre-strain can be imposed through appropriate initial variables condition. In this case, it has been added to evaluate the initial conditions, then two transient steps solve the actuation.

During this step, heating is applied through the PDE thermal balance as Joule heating. A constant 0.5 A current is applied for 10 seconds trough a rectangle function.

3.3.2 Results

Unlike the model implemented through the Lagoudas routine, the model here realized inherently solves the energy balance. The heating law is displaced in Figure 3-13: the rectangle function assumes a unit value multiplied by the current value in a 10-second window. In the same figure, overlaid on the control law is the time development of the temperature at the mid-point of the wire. As soon as the power is applied, the temperature starts rising until reaching 155°C.

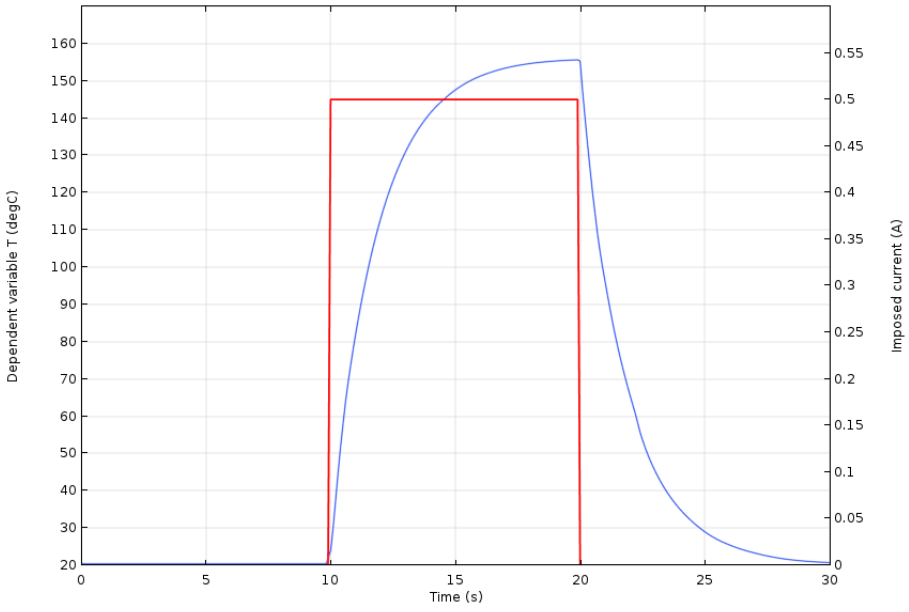

Figure 3-13 - Joule heating control law and temperature in the middle point of the wire

This is the actuation phase, where the SMA martensitic fraction decrease and produce a contraction of the wire along its axis. The maximum deformation occurs at 20 sec and results in a 2.9 mm vertical deflection of the central point of the beam and a 2.6 mm wire contraction.

After removing heating, the wire immediately starts cooling and the structure rearms it. In 10 seconds, the structure comes back to its initial undeformed shape.

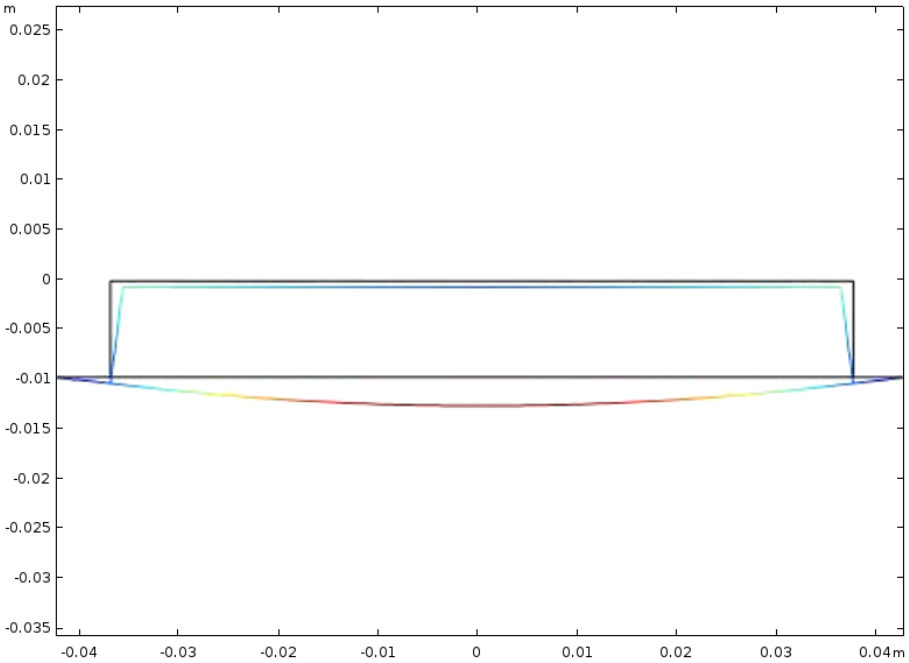

Figure 3-14 - Deformed configuration of the beam

3.4 Discussion

For being an effective design tool for actuators, a good model must be able to describe both pseudoelasticity and pseudoplasticity (shape memory effect and then recovery force). Moreover, in order to be implemented with modifications that take into account other effects than the basic behavior, it must be flexible and guided by simple formulations. 3D character is very interesting for non-linear applications, but it is not a mandatory parameter, because most SMA applications are based on thin wires that have trusses behavior, with no flexural stiffness. Computational/experimental cost and implementation ease are also an important parameter for a constitutive model, to assure reliability against different possible applications. Some features that could be interesting to take into account are cycling and pre-strain (functional fatigue), hysteresis internal loops (partial actuation), anisotropy (use of sheets), secondary effects such R-phase or TWSME (specific actuators need).

The model based on Tanaka has to be discarded for this study is. It fits well to simulate the uni-axial test and - being phenomenological - has great ability to be modified by getting good simulations. Despite this, it is not suitable for the simulation of actuators because it is able to reproduce the pseudoelastic effect only.

The Boyd and Lagoudas model is widely used in engineering applications, because closed form solutions for pseudo– elasticity and plasticity are obtainable from the model. Moreover, it is interesting for its 3D formulation that allows simulation also complex configurations. On the other side, this potential leads to a complex mathematical formulation that complicates the possibility of adapting the formulation in case of specific characteristics of interest. Another drawback is the large number of material parameters to be determined. The basic macroscopic parameters such as Elastic moduli and maximum transformation strain are still the only ones that can be customized because other parameters are difficult to identify and the values already implemented are to be used. Furthermore, due to its provenance from the classical theory of plasticity, the dissipation potential is not chosen from physical reasoning but rather from mathematical arguments like convexity properties.

On the other side, the MAS model is now implemented only in its 1D formulation and the version here adopted assumes single crystal hypothesis. Despite these simplifications, the coupling with the energy balance allows reproducing the time-dependent response of the material in terms of both temperature and displacement, like in the case of an electrically heated SMA wire under a time dependent electrical load and this is very motivating for actuation fine control. The attractiveness of the model is that the complete thermomechanical hysteretic behavior is derived from the energy function alone without any additional loading/unloading criteria and the simplification (1D and single crystal) does not reduce formal rigor. Moreover, the model uses a limited number of parameters, clearly attributable to the physics of the material and easily

obtainable, together with a convenient mathematical structure in the form of an ODE system, allowing for robust numerical integration. All these features together make the model an attractive candidate for the simulation of SMA actuators and eventually their control.

This qualitative comparison leads to the MAS model as a possible basis for investigations on the effects of fatigue and material microstructure. It combines easiness of use and a strong thermodynamic theoretical base and appears more suitable to express internal characteristics of the material tuned by the type of material itself and its cycling state.

Another aspect to consider is that the same software was not used for this analysis and therefore the possible implementable features are different, regardless of the model used. For example, in Comsol the implementation of contact between solid surfaces and beam/trusses is not integrated and easy as it is in Abaqus, and can be obtained only through mathematical stratagems and yet only as a reaction force below a certain distance and not as a real contact. A “design-friendly” model must be flexible and thus be able to be implemented in different modeling software. Despite this, the applications have been tested in the software environment for which they have been intended, to make full use of their capabilities. Modeling of smart structures with SMA actuators does not only involve the material constitutive behavior, but also the compliant structure and the dynamic system under control. Then, the possibilities given by the FE software are very important. Based on my personal experience, Abaqus is more reliable and robust in problems like Structural and Solid Mechanics and implements very efficient solvers, powerful in nonlinear problems and that is why it has been used in Aerospace and Automotive industry. On the other side, in Comsol implemented equations can be easily seen and then the user can set up their own system of equations, adjust it and relate it to geometry variables much easier than in Abaqus, which requires the compilation of user subroutines and then the study of the software definition of variables and numerical implementation. The user interfaces are different but both are at a very high level. Regarding thermal coupling, both the software has this feature, but Comsol is specifically born to study the combination of different physics and then gives more possibility to study thermal control of the actuator.

References

Ameduri S., Brindisi A., Tiseo B., Concilio A., Pecora R., 2012. Optimization and integration of shape memory alloy (SMA)-based elastic actuators within a morphing flap architecture. J. Intell. Mater. Syst. Struct. 23, 381–396. doi:10.1177/1045389X11428672

Barbarino S., Saavedra Flores E.I., Ajaj R.M., Dayyani I., Friswell M.I., 2014. A review on shape memory alloys with applications to morphing aircraft. Smart Mater. Struct. 23, 63001. doi:10.1088/0964-1726/23/6/063001

Borlandelli E., Scarselli D., Nespoli A., Rigamonti D., Bettini P., Morandini M., Villa E., Sala G., Quadrio M., 2015. Design and experimental characterization of a NiTi-based, high-frequency, centripetal peristaltic actuator. Smart Mater. Struct. 24. doi:10.1088/0964-1726/24/3/035008

Concilio A., Lecce L., 2014. Shape Memory Alloy Engineering: For Aerospace, Structural and Biomedical Applications, Shape Memory Alloy Engineering: For Aerospace, Structural and Biomedical Applications. doi:10.1016/C2012-0-07151-7

Gent A.N., 1958. On the Relation between Indentation Hardness and Young's Modulus. Rubber Chem. Technol. 31, 896–906. doi:10.5254/1.3542351

Nespoli A., Rigamonti D., Riva M., Villa E., Passaretti F., 2016. Study of pseudoelastic systems for the design of complex passive dampers: static analysis and modeling. Smart Mater. Struct. 25, 105001. doi:10.1088/0964-1726/25/10/105001

Yang S., Seelecke S., 2009. FE analysis of SMA-based bio-inspired bone–joint system. Smart Mater. Struct. 18, 104020. doi:10.1088/0964-1726/18/10/104020

Chapter 4
CHARACTERIZATION PROCEDURE

Some of the physical features of Shape Memory Alloys can be assumed from data in literature with enough confidence. Nevertheless, the need for high-quality data is ever more valued in aerospace applications, due to the need to fine-tune the actuator operative routines. Unfortunately, the testing of SMAs is not yet fully standardized, although there is work in this direction at ASTM (Shaw et al., 2008). SMAs characterization requires more properties to be known than is usual for conventional alloys and – unlike them – material properties libraries either are not available or provide incomplete information for the user. Each SMA is different and small changes in both chemistry (composition) and/or processing (thermal and mechanical history) can result in quantitative and even qualitative differences in the material behavior, and, in addition, SMAs suffers of extreme sensitivity to testing conditions, which can create difficulties in material testing and interpretation. For these reasons, the user is often faced with testing SMAs in their own laboratory to obtain a satisfactory characterization of the material at hand (Shaw et al., 2008). Even under simple tensile loading, performing meaningful experiments on SMA wire is not a trivial matter and good practice is surprisingly helpful. At the same time, getting lost in characterizations that are too demanding, for the equipment needed or for the difficulty of interpreting the results, can be counterproductive, aiming at an application to reach a high readiness level. So define which features are essential to characterize and which requirements can be relaxed becomes crucial when dealing with SMAs.

Accordingly, another main issue addressed in the present work is the experimental determination of material constants from uniaxial tests. Even though the model is conceived for actuation, this type of test is used in general to characterize the physical properties of the SMA. Indeed they provide elastic moduli of pure phases, transformation strains at various temperatures and the dependence of the stress from the temperature. Moreover, the uniaxial tensile test can be useful also to design actuators, through the graphic method described in (Concilio and Lecce, 2014), which consists in comparing the tensile tests of the SMA at ambient and actuation temperature with the stiffness of the constraining structure. The experimental techniques that I have used to calibrate and validate the model on a real application, will be described in this section. The characterization has been conducted on a commercial material commonly used at iMSL for mechatronics applications: a Dynalloy–Flexinol NiTi wire of 0.076 mm (0.003 inches) diameter. This is aimed at defining a standard for the identification of physical data (elastic moduli, transformation strains and Clausius-Clapeyron coefficients) and parametrization coefficients for the model (coefficients of the analytical stress-fraction law), with particular reference to the "parametric" model. Parameters related to material are listed in Table 4-1.

Table 4-1 - Parameters for the MAS model

Name	Unit	Description
Cp	(J/kg/K)	Specific Heat
k	(W/m/K)	Thermal conductivity
LH	(cal/g)	Specific Latent Heat of Transformation
nu	(–)	Poisson's Coefficient
ro	(kg/mm^3)	Density
Ea	(GPa)	Young modulus of Austenite
Em	(GPa)	Young modulus of Martensite
epsT	(–)	Max. transformation strain
sigmaA	(MPa)	Transition stress A to M+
sigmaM	(MPa)	Transition stress M+ to A
tau	(s)	Frequency for the transition (Yang and Xu, 2011)
VL	(m^3)	Volume of an active layer (Yang and Xu, 2011)

4.1 Calorimetric characterization

The first step in characterizing a SMA is to perform a Differential Scanning Calorimetry (DSC) test, to determine the temperature and heat flow associated with material transitions. DSC provides quantitative and qualitative data on endothermic and exothermic variations of SMAs during

physical transitions that are the solid-state phase changes. The specific targets of DSC analysis for SMAs are transformation temperatures, specific heats, and latent heats. Alternate methods exist to measure transformation temperatures, such as electrical resistivity scanning, but while potentially convenient, they are more difficult to interpret and do not provide any information about latent heats of transformation or specific heats.

Recalling the descriptions given previously, the four transformations become evident in the DSC thermogram thanks to two or four (this depends on the presence of the R phase; see Section 4.1.2) peaks. Each peak represents the energy addition or subtraction needed to transform the crystal structure, that is measured as the ‘‘excess’’ heating or cooling needed to maintain the temperature rate. All first-order phase transformations are associated with latent heat exchange and SMAs make no exception. In literature, both the two possible conventions for the positive direction of the heat flow can be found, that is, the two directions of the vertical axis. This may depend on the settlements used to graph the data, or from the position of sample and reference in the instrument, but, in any case, the transformations remain unambiguously identified: the direct transformations A→R and A/R →M occur during cooling and are associated with exothermic peaks, whilst the opposite for the revers ones (M→R and M/R →A occur during heating and are associated with endothermic peaks). In addition, thermal hysteresis causes Transformation temperatures of a direct transformation to be always lower than those of the corresponding reverse one.

The latent heat peaks separate temperature regimes where pure (or nearly so) phases exist. The two marginal ranges of high and low temperatures correspond respectively to stable austenite and martensite, whilst rhombohedral dominates at intermediate temperatures. As the temperature traverses a given latent heat peak, the material has a progressive mixture of the two phases from either side of the peak. The adjective "thermal" is sometimes added to these states of the phases, because DSC-measured samples are always stress–free. The interaction between temperature and stress is a key aspect of SMAs and it is important to keep in mind that under the action of the stress, not only these ranges of stability change, but also the microstructure of martensite is different (twinned/detwinned).

4.1.1 Some considerations on DSC measurements

With SMA wires, especially the ones for actuation that are very thin, I have experienced that some attention should be paid to sample preparation, because this can affect the quality of the results.

First, in DSC measurements, it is important to ensure good thermal contact between the sample pan and the material specimen, which will ensure that the temperature read by the DSC thermocouple accurately measures the temperature of the sample. This is generally optimized by having thin, flat surfaces that cover as much of the pan bottom as possible. Usually wires are simply cut into a number of short lengths, which are placed side by side, creating a single layer of material that fills the sample pan. Since their circular section intrinsically limits the thermal contact, wires can be scratched with fine sandpaper, but this operation is not suitable for actuation thin wires, so just place them so that they are side-by-side and possibly not overlapped. Cutting

the wire should be done in a manner to avoid plastic deformation, which introduces residual stresses, so a clean cut is needed without plastic bending.

Figure 4-1 - Pan with layer of wires. Open on the left and then closed on the right.

The pans used are standard aluminum. In DSC measurements, the sample pan can be either open (uncovered) or hermetic (sealed using a sample encapsulation press). The first are a common option and optimize atmospheric interaction, the second are normally used only for special applications, like materials generating gases (volatile liquids, materials that sublime, materials in self-generating atmospheres, etc.). In the case of SMAs, the best solution is the intermediate solution of pans crimped with an aligned or inverted lid. Crimped pans improve the thermal contact between the sample, pan and disc and reduce thermal gradients in the sample. During crimping operation is also important to keep the specimen free of contaminants, including moisture, to avoid introducing unwanted artifacts into the thermogram.

Selection of the optimum weight can vary. In general, the sample to be analyzed must be representative of the total sample and the change in heat flow due to the transition of interest should be in the range of 0.1 - 10 mW, then for metal suggested mass is about 5 mg. The mass used here is 5.35 mg.

Despite the fact that the transformations are generally characterized as athermal, meaning that they are neither thermally activated nor rate dependent, the consistency of the DSC measurements can be affected by the cooling/heating rate specified by the user. Here a commonly used rate of 10 °C/min is used, which is a compromise between trade-offs. Higher rates tend to give sharper enthalpy peaks, which can be integrated more accurately, but may not give accurate Transformation temperatures due to thermal lag. Lower temperature rates will reduce thermal lag, but excessively slow rates can make the enthalpy peaks rather indistinct.

The peaks are bell shaped (more often not symmetrical), so the start and finish temperatures of a transformation are typically extracted by a straight-line construction fitted to the steepest sides of the peak. The particular Transformation temperature is read off the intersection of this line with a ‘‘baseline’’ that cuts off the peak. One can appreciate that this procedure has some uncertainty associated with it, since it depends on the shape of the enthalpy peak and the baseline that is chosen.

The DSC is a twin instrument and its output is the difference between the heat flows measured by a sample and a reference calorimeter within a common thermal enclosure. It follows that if the two calorimeters are identical and symmetrically positioned within the DSC enclosure, the differential heat flow signal of the empty DSC should be zero. However, all DSCs give nonzero heat

flow measurements when operated empty. The instrument baseline is the residual heat flow signal of the DSC when operated empty. Moreover, empty pans should produce a flat signal (constant Heat flow), but this is not verified too. To avoid uncertainty due to baseline choice, it is good practice to acquire it, measuring the signal of empty pans and lids with the same mass of the ones containing the sample and with the same cooling/heating rate used during the sample scan. Moreover, a 10-minute isothermal step before the cycle gives the value of the Heat flux in isothermal regime that can be used to normalize all the curves. The acquisition signal of the baseline is reported in Figure 4-3 within the sample measurements.

4.1.2 How to isolate R phase

The transformations involving the R phase are associated with a few degrees thermal hysteresis. This means firstly that Rcs and Af are separated by 3–4 °C on average and the same occurs for Rcf and Af; secondly that often the endothermic peaks associated with M→R and R→A (heating curve) are partially overlaid. At worst, the two transformations are not clearly distinct, to the limit of appearing as one and – in any case – discerning between the two endothermic peaks can be "tricky". For this reason, it is useful to compare the full DSC cycle with partial cycles as suggested by (Olbricht et al., 2011).

The first partial cycle is needed to isolate R→A transformation. First, it is required stabilizing the sample in pure A phase (thus heating more than Af); then, the cooling ramp has to be interrupted between the two exothermic peaks, at a temperature sufficiently below Rcf, but possibly higher than Ms, compatibly with the separation of the two peaks. In this way, only R phase should form and then the measured heat absorption is related only to the transformation from R to A when heating (Figure 4-2a).

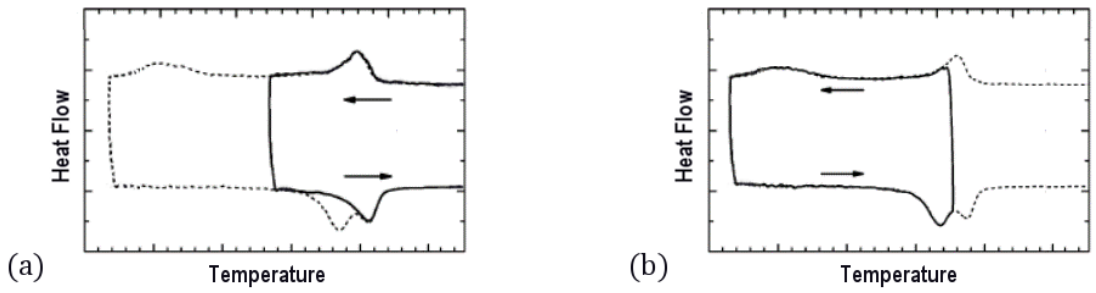

Figure 4-2 - Partial cycles to isolate R-phase and Martensite

Similarly, the M→A peak can be obtained by a second partial cycle that stabilizes the sample in pure M phase and then interrupt heating between the two endothermic peaks (Figure 4-2b). Alternatively, M↔A cycle can be derived subtracting the a-type partial cycle from the complete cycle. Often this is a better solution, because heating peaks are often partially or even fully overlapped. Then may be difficult identify the temperature at which stop heating and even so the isolated peak can result partial. Figure 4-3and Figure 4-4 show experimental results for Dynalloy–Flexinol NiTi wire.

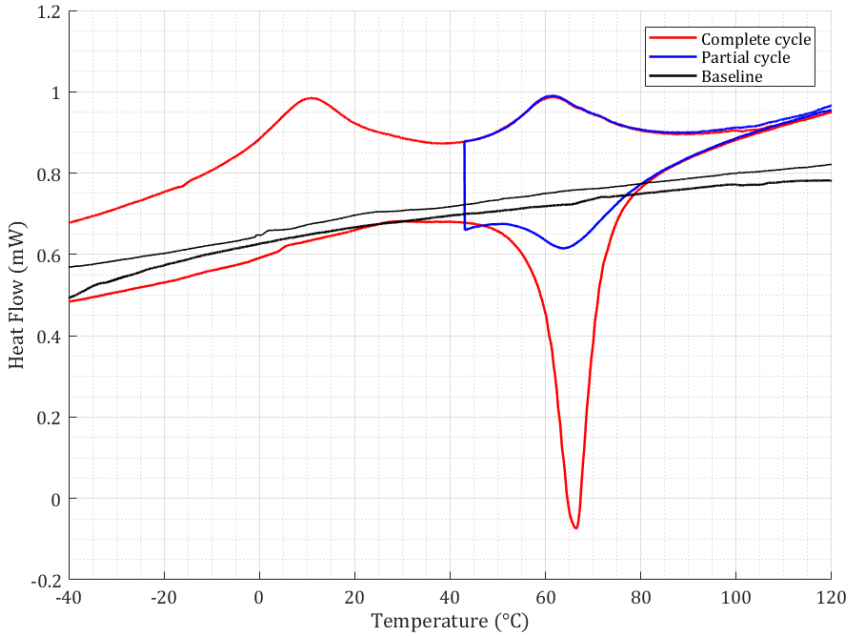

Figure 4-3 - DSC thermograph of the complete cycle, the partial cycle to isolate martensite and the baseline with empty pans

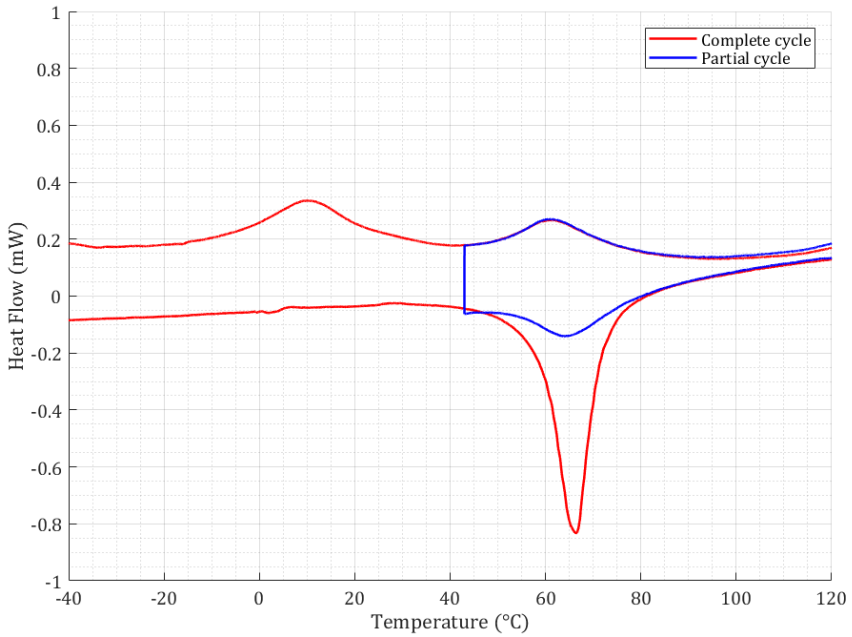

Figure 4-4 - DSC thermograph of the complete cycle and the partial cycle deducted the baseline

The presence of the R-phase is evident in the complete cycle (red curves) from the two peaks on cooling, whilst only one peak seems to appear on heating. Carrying the partial cycle, the contribution of R-phase to endothermic peak becomes evident (blue curves). The similarities of the areas of the two peaks obtained during cooling and heating and the small thermal hysteresis between the peak positions represent experimental proof of the forward and reverse transformation of R-phase. From these experiments is evident that the b–type partial cycle is not

pursuable, because the peaks are fully overlapped. Then the contribution of Martensite has been obtained through signal subtraction and can be seen in Figure 4-5 and Figure 4-7.

4.1.3 Transformation temperatures

Transformation Temperatures are essential to identify the operative conditions. When the SMA component is used for its pseudo-elasticity, the ambient temperature must be higher than Af and the transformation stress is directly proportional to the gap between the two. If the SMA component is intended for actuation, ambient temperature must correspond to M or R phase at zero stress and the activation temperature will depend on the Af temperature jointly to the stress to which the actuator is subjected. From the characterization point of view, Transformation temperatures are needed also to define ambient conditions at which perform mechanical tests.

Three characteristic temperatures can be identified for each peak: start (s), peak (p) and finish (f) temperatures. Austenite temperatures are referred to heating with A as product phase, and then they are the highest. In analogy, Martensite temperatures are referred to cooling with M as product phase, and then they are the lowest. The nomenclature of Rhombohedral temperatures must distinguish between heating and cooling because R is an intermediate phase and then can be product in both cooling and heating.

Transformation temperatures of a Nitinol alloy can be tailored by the supplier anywhere from cryogenic temperatures to as high as about 100 °C by small changes in chemistry, by aging heat treatments in the range 350–500 °C, and by thermomechanical processing. The first-order effect on transformation temperatures is alloy chemistry. (Shaw et al., 2008)

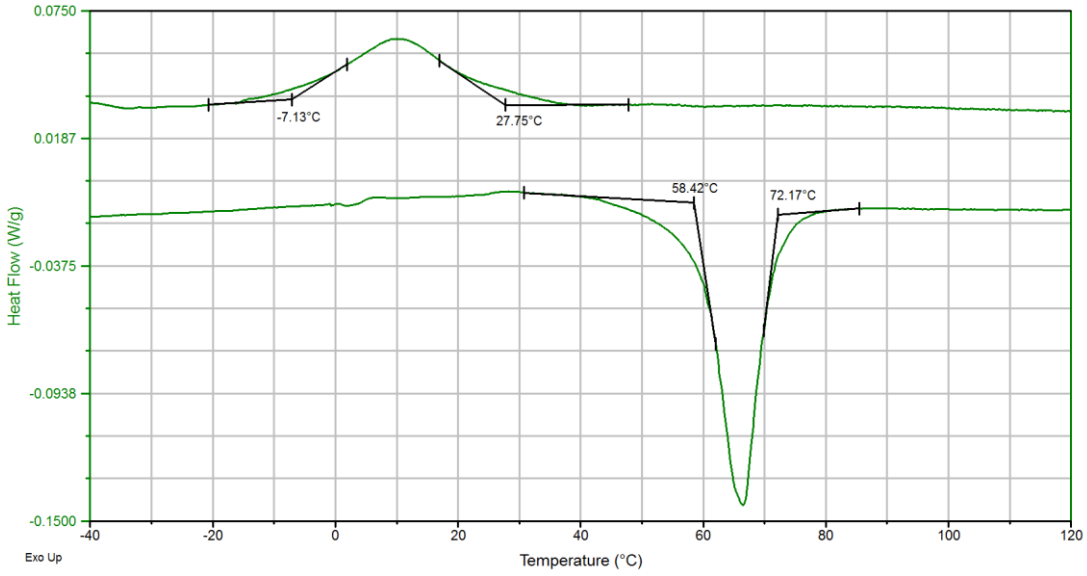

Figure 4-5 - Transformation temperatures for M↔A cycle

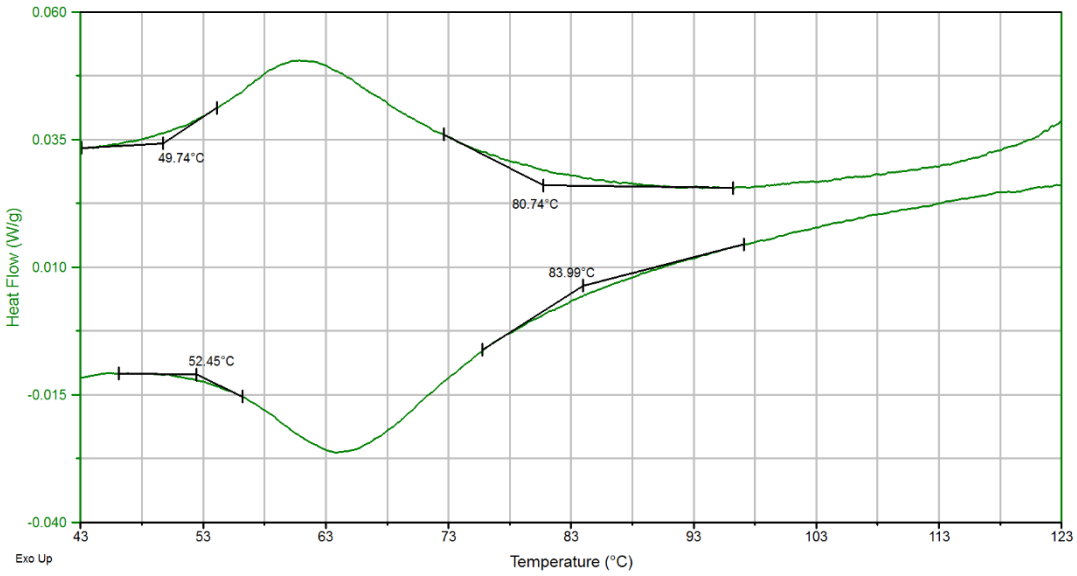

Figure 4-6 - Transformation temperatures for R↔A cycle

As already mentioned, the transformation temperatures are extracted by a straight-line construction fitted to the steepest sides of the peak. Figure 4-5 shows the transformation temperatures extracted from M↔A cycle. The interest is particularly focused on Ms (27.75 °C) and Mf (-7.13 °C) temperatures. Since at room temperature at zero stress the material falls in the middle of the transformation peak, its condition depend on whether is being heated (then it is fully martensitic) or cooled (as in actuation case and then the condition depends on the stress applied). Figure 4-6 instead gives transformation temperatures for R↔A cycle and serves to get As (52.45 °C) and Af (83.99 °C) temperatures. The results are summarized in Table 4-2.

4.1.4 Transformation Latent Heats

The specific latent heat LH (per unit mass) for a given transformation is obtained by integrating the shaded area of the peak by:

$$\mathrm{LH} = \int_{t_1}^{t_2} \dot{q}_\mathrm{L}(t)\,\mathrm{d}t = \int_{T_1}^{T_2} \frac{\mathrm{d}q_\mathrm{L}}{\mathrm{d}T}\,\mathrm{d}T \qquad (4\text{-}1)$$

Where q_L is the specific latent heat (Q/m) and t_1 and t_2 are the respective start and finish times of the transformation with the corresponding T_1 and T_2.

The resulting latent heats for the transformation are summarized in Table 4-2, along with temperatures.

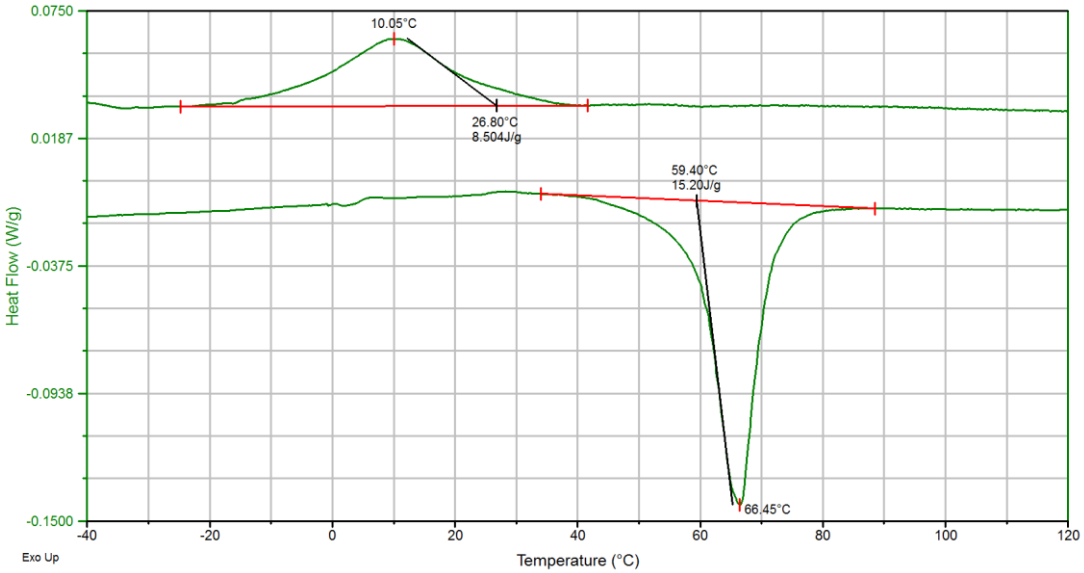

Figure 4-7 - Peak temperatures and latent heats for M↔A cycle

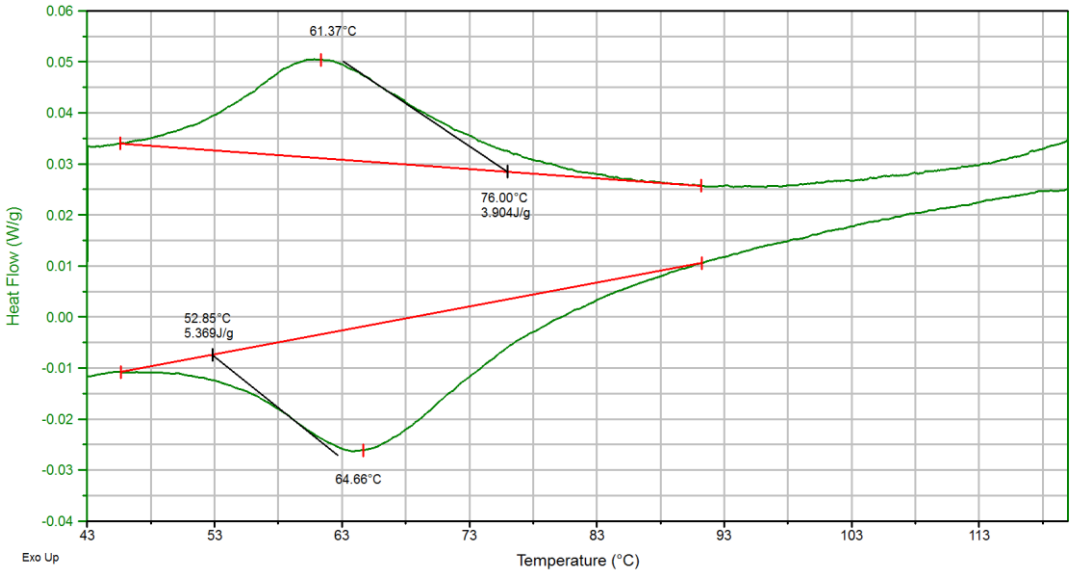

Figure 4-8 - Peak temperatures and latent heats for R↔A cycle

Table 4-2 - Results from DSC analyses

Peak:	M↔A cooling	M↔A heating	R↔A cooling	R↔A heating
T start (°C)	27.75 (= Ms)	58.42	80.74	52.45 (= As)
T peak (°C)	10.05	66.45	61.37	64.66
T finish (°C)	-7.13 (= Mf)	72.17	49.74	83.99 (= Af)
LH (J/g)	8.504	15.200	3.904	5.369

4.2 Mechanical characterization

Due to the thin dimensions of the Flexinol wire, a DMA (TA instruments Q800) with 18 N load cell has been used for tensile tests at constant temperature (stress-strain test, SS). Temperatures for the near-isothermal tests have been selected based on the DSC results.

– Starting phase Austenitic:
- ~Af = 80 °C
- Af + 10 = 90 °C
- Af + 20 = 100 °C

– Starting phase Martensitic:
- ~Mf = –10 °C
- Mf – 10 = –20 °C
- Mf – 20 = –30 °C

– Room temperature:
- 20 °C
- 25 °C
- 30 °C

Results are shown in Figure 4-9 for temperatures above Af (pseudo-elastic behavior) and in Figure 4-10 for room temperatures and below Mf (pseudo-plastic behavior). The wires have been stretched until reaching the elastic part of stress-induced martensite.

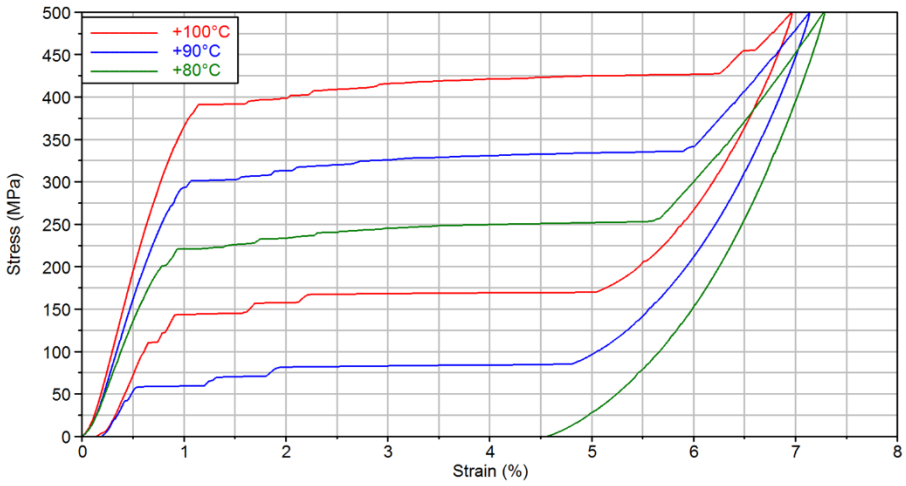

Figure 4-9 - Near-isothermal tensile Stress-Strain results above Af

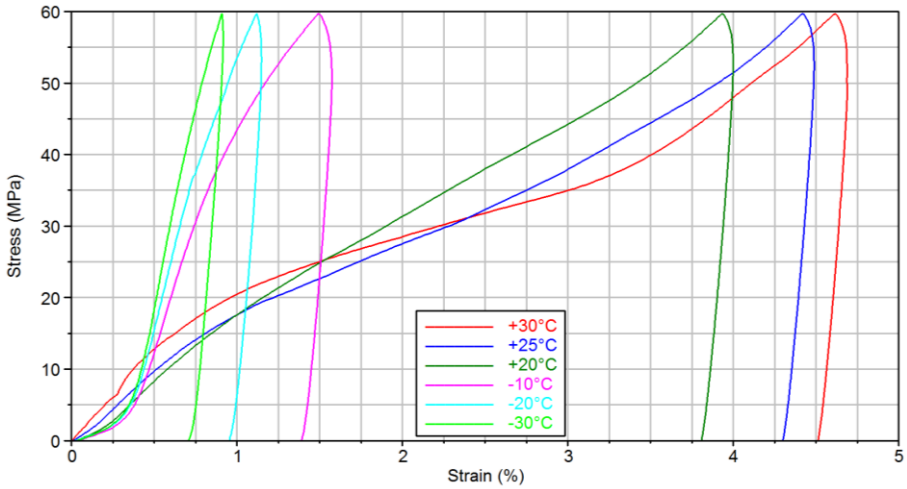

Figure 4-10 - Near-isothermal tensile Stress-Strain results at room temperature and below Mf

For identification and calibration purposes, we start considering only the pseudo-elastic behavior, in which the initial phase is fully austenitic. The transformation develops with nucleation and propagation of stress-induced martensite (SIM), but also the R–phase competes with martensite for the transformation, then, also the formation of stress-induced rhombohedral (SIR) occurs. Rhombohedral phase contributes only at low strains, below 0.5 %, but reveals its presence in the first part of the elastic range, where the path is not linear and the first derivative increase (see also Chapter 2). Differently from what reported by the extensive study by (Helbert et al., 2014), our experiments show that elastic modulus is reduced in the very first part also for temperatures above Af.

Analyzing the slope of the mechanical cycle two points can be identified and used for characterization. The first one is the maximum value of slope in the loading path: it marks the end of the R-phase contribution, so it denotes also the austenitic elastic modulus. The second is the maximum negative slope of the unloading path, which is the martensitic elastic modulus. The unloading path starts with a sudden reverse of the load causing inaccuracies, also for this second point an initial part has to be excluded. These two points results clear when analyzing the time trend of the derivative of stress with respect to strain. Figure 4-11 shows this trend for the tensile test at 100 °C: red circles marks the two points described, while the green stars mark the two plateaux.

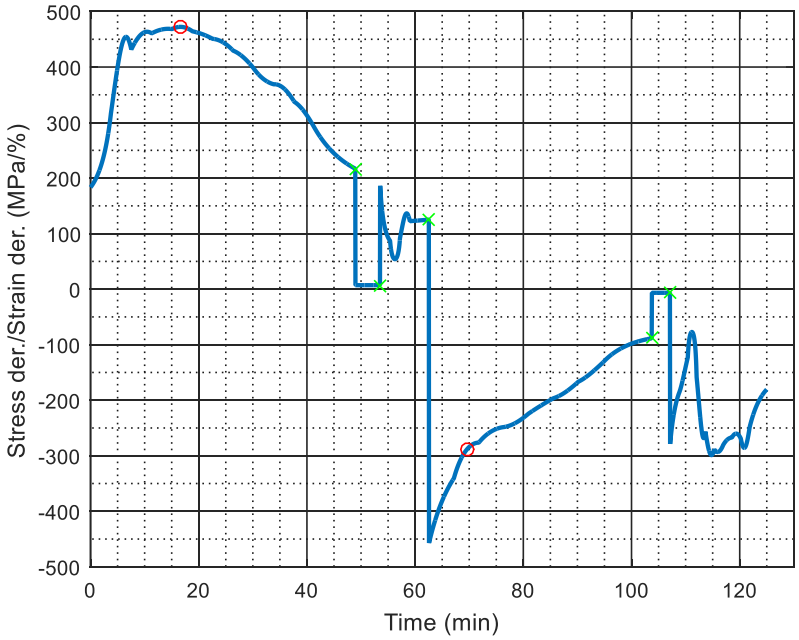

Figure 4-11 - Derivative of the Stress-Strain curve for the test at 100 °C

The second point (beginning of the unloading phase excluding the initial inaccuracies) can also be used to have the maximum transformation strain. This is obtained tracing the tangent to the stress-strain curve in this point and extending it down to zero stress. Figure 4-12 shows the trend in the case of the test at 100 °C.

The resulting values of this analysis are:

- Elastic modulus of austenite: Ea = 47.2 GPa (at 0.365 % ,132.97 MPa)
- Elastic modulus of martensite: Em = 28.9 GPa (at 6.723 % and 444.15 MPa)
- Maximum transformation strain: $\varepsilon_T = 5.2$ %

These values are in line with literature and the value of the maximum transformation strain is very close to the extension of the loading plateau, proving that this identification method is actually reliable.

For the purposes of this analysis devoted to model calibration, the part at low stresses/strains that is characterized by the presence of the R-phase can be neglected. Several fundamental aspects of this transformation are still under investigation (Ren et al., 2001) and their comprehension goes beyond the purpose of this work, moreover R-phase contributes to the deformation with a very low mechanical loop under 1% strain (Otsuka, 1990) and in a real application it tends to disappear with cycling. For these reasons, the parts of the mechanical cycle attributed to R-phase can be substituted with straight lines. In the loading path, the straight line goes from zero to the first point identified earlier (strain-stress point locating the end of the R-phase transformation). In the unloading path, the start of the backward R-phase transformation is simply chosen with good confidence as the one with the same strain of the forward one. These two straight lines are highlighted in red in Figure 4-12. The same figure shows also the second point previously described and the tangent line identifying the maximum transformation strain (dashed magenta line in Figure 4-12).

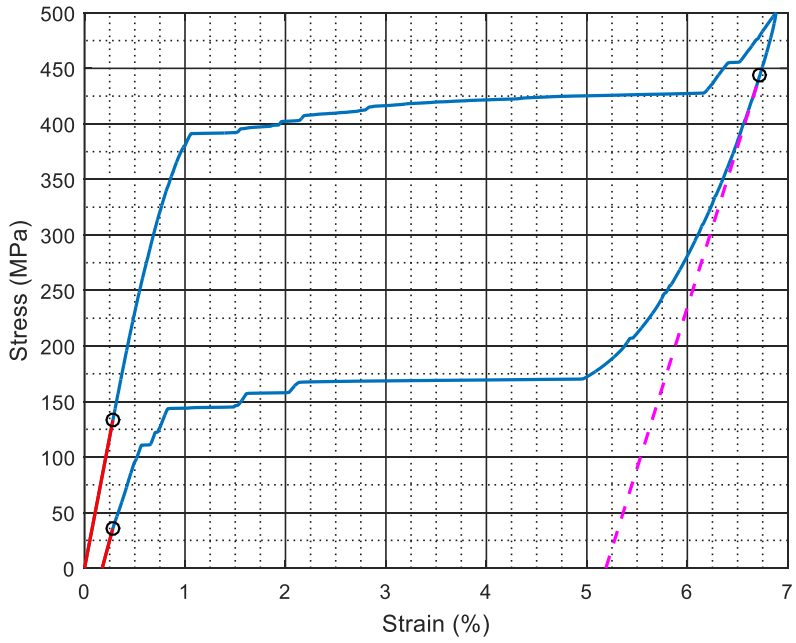

Figure 4-12 - Stress-strain cycle at 100 °C after R-phase influence removed.

To define the scaling with temperature, in addition to SS tests, also cooling and heating cycles at constant stress (strain-recovery test, SR) have been performed. Stress levels for the isostress cycles have been set to 10, 20, 30 and 40 MPa. Results are shown in Figure 4-13.

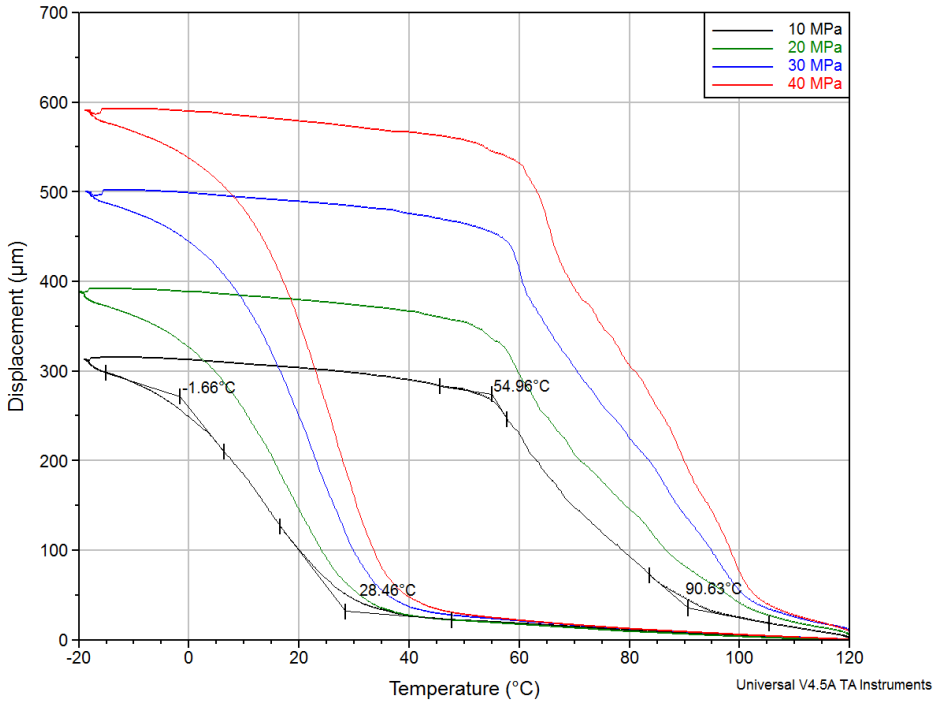

Figure 4-13 - Isostress tensile Strain-Recovery results with transformation temperatures at 10 MPa stress

From the onset of SR cycles, transformation temperatures (Ms, Mf, As, Af) can be obtained at different levels of stress. Figure 4-13 shows as an example the results of the 10 MPa test. Start and finish points of both direct and reverse transformations can be easily identified. A linear regression calculated using these points gives the Clausius-Clapeyron relationship and then the scaling factor for transformation stresses at different temperatures. Figure 4-14 displays the temperature from the SR tests at the corresponding stress levels and the temperatures from DSC at zero stress. The robust fit giving the Clausius-Clapeyron coefficients are also reported with the following results:

- Cl-Cl Ms = 4.79 (MPa/K)
- Cl-Cl Mf = 3.57 (MPa/K)
- Cl-Cl As = 4.49 (MPa/K)
- Cl-Cl Af = 3.46 (MPa/K)

SS curves can be used to have additional information, but SR tests are much more better for this purpose. Initial and final onsets of the loading plateaux correspond to the nucleation and the complete transformation of the SIM, so they can be taken as a starting and ending stresses at the test temperature (σ_{Ms} and σ_{Mf}). The reverse transformation from the SIM starts actually as soon as unloading starts (SIM is not stable at high temperature), so it is unfitting assuming the onset of the unloading plateaux (σ_{As}) as a start condition. Likewise, the onset at the end of the unloading plateaux cannot be taken as the end of the transformation, because – as discussed with reference

to Figure 4-6 – Af (and then σ_{Af})is the finish temperature for R↔A cycle, thus involving also R-phase. The points obtained with SS curves are indicated in Figure 4-14 too.

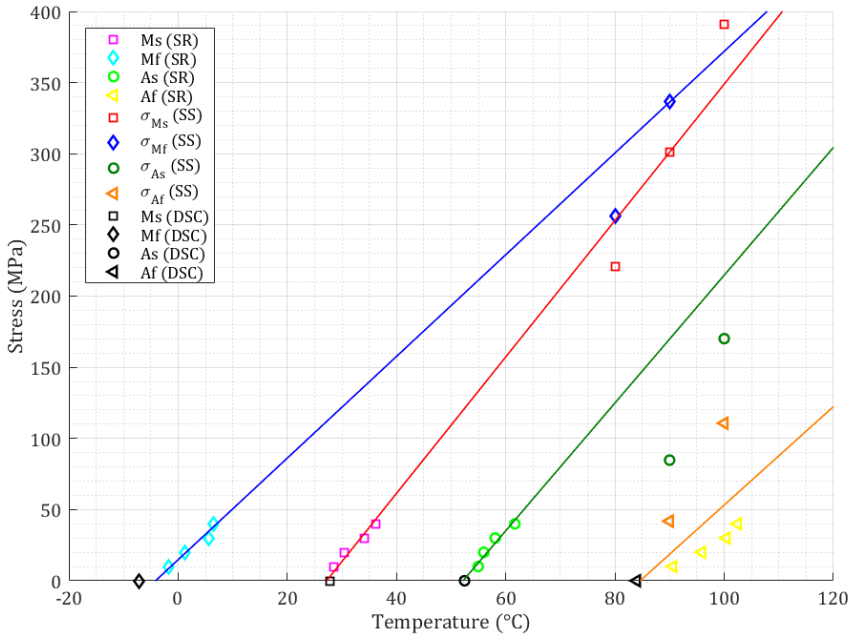

Figure 4-14 - Transformation temperatures from DSC and SR tests, transformation stresses from SS tests and linear regression

4.2.1 Tensile rate in isothermal tests: strain- vs. stress- control

An observation is noticeable about the type of control used for tensile tests. The MAS model comprises both the heat absorbed–exchanged–generated during transformation, and the effect of increasing transformation stress with increasing temperature. Consequently, SS tensile tests should be made in perfectly isothermal conditions, to exclude the thermal effects already considered in other parts of the model. To have an isothermal test, the transformation should occur very slowly to allow the heat generated by the material to be dissipated. This implies a low tensile rate during the plateaux and therefore the question arises of how to obtain this with DMA. Indeed, that is an instrument using force as physical quantity for direct control and then force/stress–controlled tests give a curve with low disturbance, but also different velocity and sampling during elastic part and plateau. On the contrary, displacement/strain control assures same velocity and sampling during the whole cycle, but introduces more disturbance on the curve (Figure 4-15). This is not only a noise on the curve, but effectively a control issue, because DMA is very sensitive to displacement and then each movement of the martensitic variants as the transformation front propagates along the sample gives a control shift. Moreover, the presence of slides is either a disturbance in the calibration of the model, because it makes difficult to identify the actual loading/unloading stress values and trend. The force-controlled test requires more time (approx. 2 hours each cycle) to be performed at the same slow rate than a displacement–controlled test, but it is to be preferred to calibrate the model. To ensure that the chosen tensile

rate does not give a non-zero slope due to self–heating during the transformation, a rate conversion study from strain-control has been performed. Two are the questions to be answered: which is the maximum low–strain rate ensuring a near-isothermal test and which is the corresponding value of stress rate.

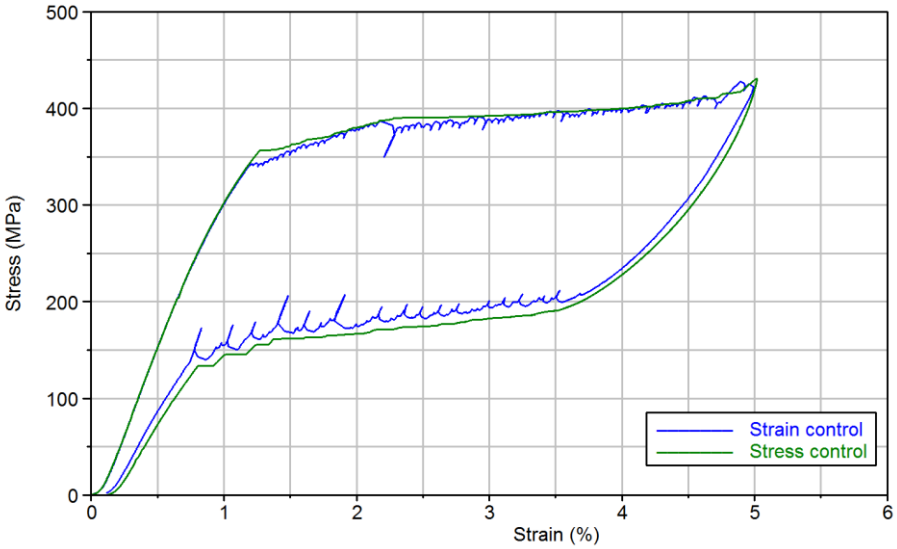

Figure 4-15 - Comparison between strain an stress control curves during isothermal tensile test using DMA instrument

As comparison, tensile tests at different strain-rate values have been performed. Maximum strain has been fixed at 5 % and the rates considered are 0.1, 0.2, 0.5, 0.7, 1.2, 1.5 %/min. Results are reported in Figure 4-16.

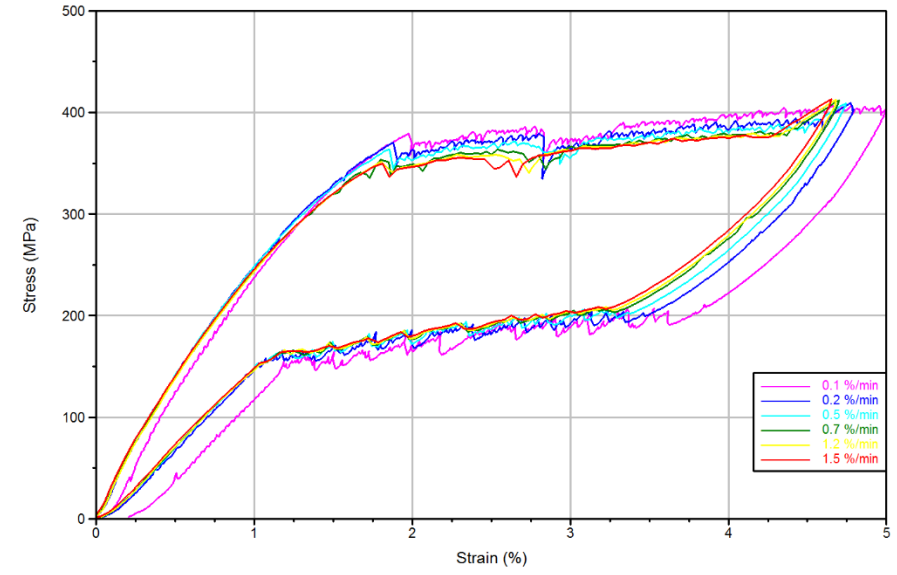

Figure 4-16 - Comparison between tensile tests at different strain-rate values

The cycles have been performed in sequence on the same sample, starting from the slowest rate to the fastest. As can be seen the disturbing shifts in the plateaux mainly correspond between the cycles. This proves that these are due to martensite variants triggering as the transformation front

propagates along the sample. Due to the stabilization of the material, disturbances on the curve decrease with cycling because the SIM triggering within the volume becomes smoother. Another aspect resulting from material stabilization is that the stress level of the plateaux and the hysteresis area decrease with cycling, so these are not effects to be ascribed to the strain rate. The effect of the strain rate on the plateaux slope is not clearly distinguishable from this plot, also because of the strain-control disturbed signal. Then a linear interpolating fit has been used to evaluate the slope of the plateaux. Yet again because of disturbances, this is not representative of the actual stress value, but it is suitable for comparison if made with same conditions for all curves.

In Figure 4-17, the linear robust fits of loading plateaux only are reported to valuate if the interpolant lines are valuable to be used for comparison purpose. To obtain a better fit, interpolation is made using time dependent data (stress(t) and strain(t)) and then combining them in stress(strain) curves.

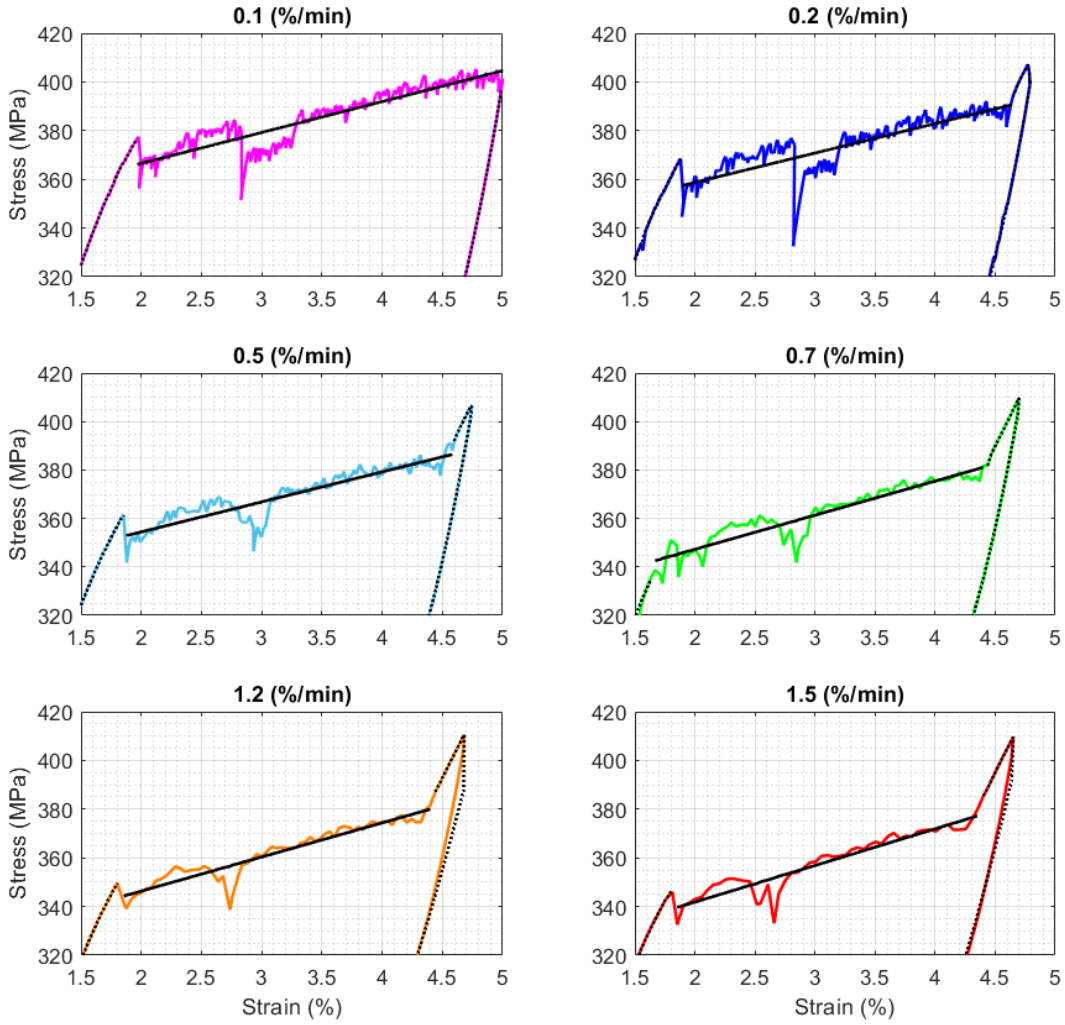

Figure 4-17 - Linear fits of loading plateaux only

Linear interpolation coefficients of the same loading plateaux are then compared in Figure 4-18. For each strain–rate control value, the slope of the plateaux is given both as stress/time and as stress/strain rates. The first are the coefficient of the linear interpolation of time–dependent stress curves (blue cross points in Figure 4-18). The second are the slope in the SS graphs,

obtained dividing the stress/time value by the strain rate (red star points in Figure 4-18). Values at 0.7 %/min are excluded from interpolation because outliers.

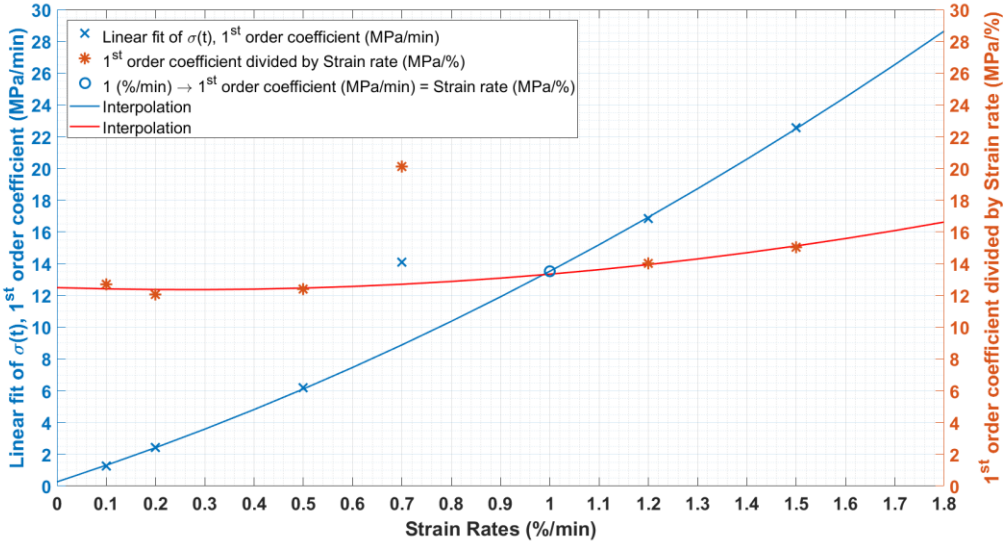

Figure 4-18 - Comparison betweeen the rates in the plateaux.

The blue curve confirms that the stress rate decreases reducing the strain rate with a quadratic dependence. More interesting is the red curve, from which it is noted that the slope of the plateaux actually decreases by reducing the strain rate of the test although varies little. Since red curve is obtained dividing by the strain rate, it should tend to {0,∞). The point at 0.1%/min seems to confirm a rising tendency, but more points at very low rates should be added to verify the asymptotic behavior. The usual strain rate 0.5 %/min has taken as a reference, being a good tradeoff between a sufficiently low rate and a reasonable short test. Figure 4-19 shows the time dependence of strain rate and stress rate for the test performed at this velocity. The stress–rate value at which the tensile tests have been performed has been defined as 6.5 MPa/min.

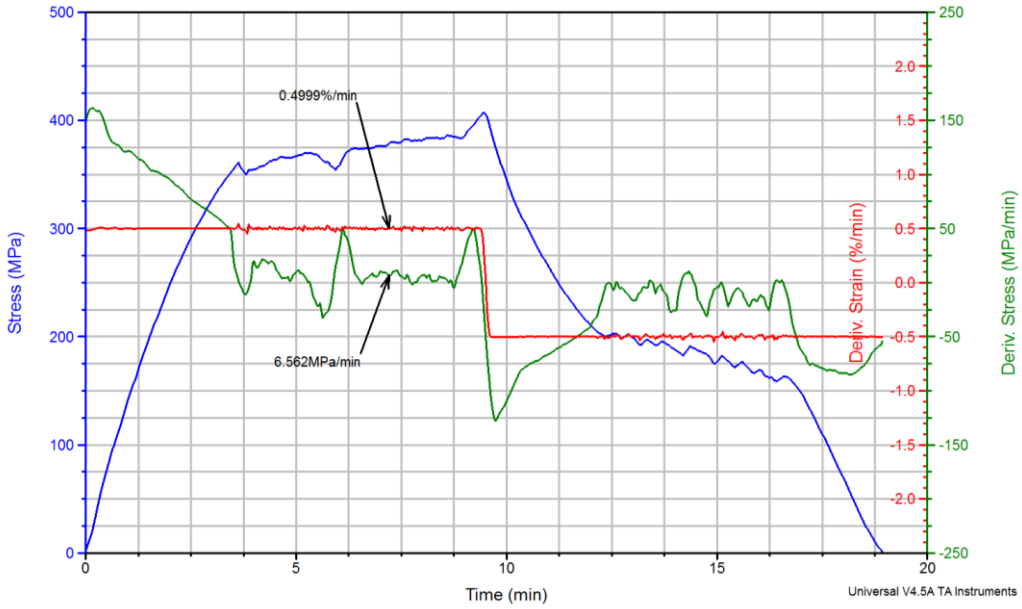

Figure 4-19 - Time dependence of strain rate, stress rate and stress for the test performed at 0.5 %/min

References

Concilio A., Lecce L., 2014. Shape Memory Alloy Engineering: For Aerospace, Structural and Biomedical Applications. Elsevier Ltd. doi:10.1016/C2012-0-07151-7

Helbert G., Saint-Sulpice L., Arbab Chirani S., Dieng L., Lecompte T., Calloch S., Pilvin P., 2014. Experimental characterisation of three-phase NiTi wires under tension. Mech. Mater. 79, 85–101. doi:10.1016/j.mechmat.2014.07.020

Olbricht J., Yawny A., Pelegrina J.L., Dlouhy A., Eggeler G., 2011. On the stress-induced formation of R-phase in ultra-fine-grained Ni-rich NiTi shape memory alloys. Metall. Mater. Trans. A Phys. Metall. Mater. Sci. 42, 2556–2574. doi:10.1007/s11661-011-0679-y

Otsuka K., 1990. Introduction to the R-phase transition, in: Duerig, T.W., Melton, N.K., Stöckel, D., Wayman, C.M. (Eds.), Engineering Aspects of Shape Memory Alloys. Butterworth-Heinemann, London, pp. 36–45.

Ren X., Miura N., Zhang J., Otsuka K., Tanaka K., Koiwa M., Suzuki T., Chumlyakov Y.I., Asai M., 2001. A comparative study of elastic constants of Ti-Ni based alloys prior to martensitic transformation. Mater. Sci. Eng. A 312, 196–206. doi:10.1016/S0921-5093(00)01876-1

Shaw J.A., Churchill C.B., Iadicola M.A., 2008. TIPS AND TRICKS FOR CHARACTERIZING SHAPE MEMORY ALLOY WIRE: PART 1—DIFFERENTIAL SCANNING CALORIMETRY AND BASIC PHENOMENA. Exp. Tech. 32, 55–62. doi:10.1111/j.1747-1567.2008.00410.x

Yang S. Bin, Xu M., 2011. Finite element analysis of 2D SMA beam bending. Acta Mech. Sin. Xuebao 27, 738–748. doi:10.1007/s10409-011-0496-y

Chapter 5
THE STRESS–FRACTION RELATIONSHIP

The model used in the Chapters 3 and 4, is a version that accounts for the behavior of an idealized single crystal, under the assumption of a perfectly homogeneous material (single crystal model, SC). This can be encountered in basic research, but "real life" engineering components are typically based on SMAs that are neither single crystalline nor homogeneous, whether they are commercial alloys or ones specially-made for a particular application. For this reason, the SC model has been extended by its authors to be applied to engineering applications design.

The true challenge is how to extend the basic thermodynamic rules to the macroscopic behavior, without introducing artifacts that little deal with the physics of the material. As is the case, for example, of parametric models like Tanaka with Sigmoid law.

The study of the influence of the microstructure of the material on macroscopic behavior relates to local phenomena. Examples are the nucleation of martensite volumes and the propagation of the transformation front; the interface stresses accompanying grain and phases boundaries (stress that varies with the propagation of the transformation front); impurities and defects both within the crystal lattice and on the grain boundaries, inborn or generated by fatigue effects. In terms of thermodynamics, all these effects have an impact on the mechanical component of the energy barrier separating the two phases' domains. In the perfect single crystal, each mesoscopic lattice particle faces the same energy barrier, whilst each lattice particle of a polycrystalline

volume can potentially have a barrier of its own. This leads to the concept of an "effective" barrier–stress (σ_{EB}) driving the actual material response, which includes the externally applied stress (σ_e) and the internal interaction stress (σ_i).

In the context of an engineering application, one is typically not interested in the microscopic detail of these effects, i.e. the spatial location of each lattice particle with its corresponding combination of energy barrier and effective stress, but much rather its impact on the resulting macroscopic behavior.

Stochastic approach with representative elementary volume.

To this end, a first approach is to assume distribution functions, which give the fraction of particles with a particular combination of energy barrier and effective stress, and apply a stochastic homogenization procedure to compute the average strain within a control volume (poly–crystal model with stochastic approach, PCS). This approach has been applied by (Massad and Smith, 2003) as well as by (Heintze, 2004). This is a homogenization problem quite similar to that used for other multiphase materials (e.g., composite materials with polymeric matrix and reinforcement fibers): to search for the parameters of a fictitious homogeneous continuous (single-phase), which has a macroscopic mechanical response equivalent to that of the real heterogeneous continuous (poly-phase). A common concept for all homogenization theories (even non-stochastic ones) is the *representative elementary volume* (REV). In general, this is the minimum volume that needs to be considered to ensure that the result obtained applying the homogenization theory is representative of the macroscopic behavior of the heterogeneous continuous. The general theory of homogenization is very elaborate and calls for concepts often not trivial. Moreover, the need for experimental characterization does not completely disappear, because in the composition of a multi-phase material some random factors are difficult to grasp, even if homogenization takes into account the stochastic character of physical quantities. Moreover, (Heintze, 2004) showed that the method, even though reproducing experimentally observed phenomena very well, can become extremely time consuming and this is prohibitive for its implementation into numerical tools like finite element programs or control schemes.

Parametric approach with representative single crystal

From the beginning, one of the cornerstones of my thesis was to use a macroscopic parameter (possibly easily measurable) to introduce microstructure effects on mechanical behavior, so the approach described above, though physically rigorous and detailed, is not prosecutable. This leads to a more viable approach and more consistent with the prefixed goals, which is that of the polycrystalline model with parametric approach (PCP). This has been detailed by (Heintze and Seelecke, 2008) and uses the concept of *representative single crystal* (RSC). Instead of considering a set of physical single crystals within the representative elementary volume, each with a certain combination of barrier and interaction stress, the focus is only on the one single crystal that is always the next in sequence to undergo a phase transition. Once this physical crystal

has transformed, the focus is switched to the one with the next higher barrier, and so forth. Therefore, the energy barrier for the transformation changes during the process as the physical elements undergo transformations: the RSC encounters a barrier that gradually increases as the volume of transformed martensite grows and likewise decreases if this drops. The major advantage is that the "mathematics" that needs to be solved is the same ODE system as in the perfect single crystal case, but with the barrier stress $\sigma_{A\to M}$ no longer constant, but proportional to the fraction of transformed material, so that the transformation has been effectively parameterized by the phase fraction.

5.1 Analytical expression of the phase fraction

The total deformation of the polycrystalline material can be considered as the sum of the deformations of the austenitic and martensitic fractions of volume within the material. Between them, the austenitic contribution is only elastic, while the martensitic one is the combination of elastic and transformation strains. In thin wires only a tensile stress state is expected, then the presence of the "compressive" martensite phase M$_-$ can be neglected, setting $\xi_- = 0$. As in previous description of this model, the subscript A refers to austenite, while the subscript + indicates the martensite directed as to accommodate tensile stress.

$$\varepsilon = \xi_A \varepsilon_A + \xi_+ \varepsilon_+ = (1 - \xi_+)\varepsilon_A^{El} + \xi_+ \left(\varepsilon_+^{El} + \varepsilon_+^{Tr}\right) \tag{5-1}$$

The elastic strain depends linearly from the stress through the reciprocal of the Young's moduli. The maximum transformation strain ε_+^{Tr} is the same as the parameter H of the model by Lagoudas and in the same way it is easily derived from the stress-strain values of a point in the martensite elastic region (i.e. at $\xi_+ = 1$). To achieve this, a tensile test is required, which also includes the elastic field of the martensite, under penalty of underestimation of the contribution from the transformation strain if using values of stress-strain at transformation not ended.

$$\varepsilon_+^{Tr} = \varepsilon|_{\xi_+=1} - \frac{\sigma|_{\xi_+=1}}{E_M} \tag{5-2}$$

$$\varepsilon = (1 - \xi_+)\frac{\sigma}{E_A} + \xi_+ \left(\frac{\sigma}{E_M} + \varepsilon_+^{Tr}\right) = \frac{\sigma}{E_A} + \xi_+ \left(\frac{\sigma}{E_M} - \frac{\sigma}{E_A} + \varepsilon_+^{Tr}\right) \tag{5-3}$$

The effective barrier stress σ_{EB} can be determined directly from an experiment performed at a low strain rate, i.e. assumed isothermal, interpreting the measured stress as the barrier stress itself (Heintze and Seelecke, 2008). In other words, the local value of the stress becomes the macroscopic expression of the energy barrier. In analogy, its shape can be seen also as the macroscopic expression of the microstructural effects: more the transformation has net nucleation, the more the condition approaches the single crystal, while a more strained trend reveals the presence of the above mentioned defects.

Therefore, the stress σ_{EB} as a function of the fractional volume of martensite ξ is calculated inverting the 6-3 from the Stress-Strain tests with the formula (obtained from the sum of the deformations of the individual phases, weighed for the phase fraction itself) as follows:

$$\sigma_{EB}(\varepsilon, \xi) = \frac{E_M(\varepsilon - \xi_+ \varepsilon_T)}{\xi_+ + (E_M/E_A)(1 - \xi_+)} \tag{5-4}$$

Making explicit the fraction rather than the stress is also obtained:

$$\xi_+ = \frac{\varepsilon(t) - \sigma(t)/E_A}{\sigma(t)(1/E_M - 1/E_A) + \varepsilon_T} \tag{5-5}$$

In this way a parametrization is introduced into the formulation, which results in the need to calibrate the model by thermal and mechanical characterization of the specific material (chemical composition, thermal treatment, mechanical machining). In view of this need, the initial idea of modifying the expression of energy to introduce the effect of the microstructure has turned into adding this effect to the calibration by acting, not on the expression of energy, but on the parametric part of the model, correlating microstructural measures to direct in situ measures of stress and martensitic fraction. In addition to the application in the model, so it would be able to simulate with great precision the behavior of SMA elements and smart systems that they understand, these measures are also interesting as a study of the material, to clarify mechanisms and modalities of the progression of transformation

5.2 Measure of the phase fraction

X-ray diffraction (XRD) is a valuable method for the determination of the crystallographic structure of materials and then it has the potential to differentiate between the various crystallographic forms of NiTi in a sample and – under some limitations that will be discussed – allows even performing quantitative analysis to know the fraction of each phase within the material.

Then, in situ X-ray diffraction during mechanical cycling has been used here to investigate the effects of microstructural changes on the stress-induced phase transition mechanism in polycrystalline NiTi. The idea is to apply thermal treatments to NiTi samples to produce different starting microstructural conditions. For each treatment, XRD measurements have been performed upon stopping the tensile testing at specific points of the mechanical cycle identified by the corresponding strain/stress values. Then, the martensite fraction is estimated by quantitative analysis of the patterns and an experimental relationship between strain, stress and fraction is obtained to validate the analytical relationship presented above.

Since the equipment used for tension cannot be contained in the thermal chamber supplied with the instrument, it is not possible to carry out measurements of the thermally induced martensitic fraction under prescribed variable stress (which would be the operating situation of the actuators). Therefore, it has been chosen to analyze a superelastic NiTi, which have PE cycles at

room temperature that correspond to high temperature condition for microstructure of actuation-devoted NiTi.

The following sections describe the preparation and choice of samples, the designed traction system, the experiments and the analysis of the results.

5.2.1 Samples preparation

The analysis of curved surfaces with XRD is possible, but requires a high degree of sophistication in the analysis to take into account axial and radial divergence and local surface tilt giving asymmetric diffraction peaks (Zhigachev, 2013). To avoid excessive complications in the analysis, it is preferable to have flat samples, i.e. sheets, even though wires are the most used form for SMA actuators.

The penetration depth of X-ray Cu–K_α radiation in the NiTi sample is around 50 μm (Thayer et al., 1995). The stress state is supposed to be uniform in the cross section of the sheet in pure uniaxial tensile condition, so the transformation should occur uniformly within cross sections. The tensile equipment ensures the absence of bending solicitation, but little misalignment with respect to the longitudinal axis is possible leading to a composed stress state. Then, the thickness of the sheet has been chosen twice the penetration depth (100 μm) because this makes sufficient having a stress state symmetric with respect to the horizontal plane of the sheet to have reliable measurements of the volumetric fraction of martensitic phase, giving a representative value of the whole volume.

Because of these considerations, a superelastic NiTi sheet of 0.2 mm thickness and 3.5 mm width (Memry supplier) was annealed at a temperature of 750 °C for 5 min and then cold-rolled to a final 0.1 mm thickness through a two-step reduction with intermediate annealing that results in a final 33.3% cold-work reduction. To obtain superelastic NiTi with room temperature superelasticity, the cold-rolled sheet has been cut in 10 cm long strips that have been treated at temperatures of 320 °C for 8 min, 450 °C for 10 min, 600 °C for 10 min and 800 °C for 10 min.

After the thermal treatment, the specimens have been first chemically polished to remove oxides formed during the thermal treatments and then mechanically polished to remove the warped layer from the surface and the cracked ends from the sides of the strips. This polishing guarantee also a precise dimensioning to 0.1 x 3 mm of the cross section of the strips, which after rolling had reached 4.3 mm width.

5.2.2 Reference DSC and mechanical tensile tests

As described in Chapter 4, DSC and mechanical tests allow fully characterize the samples. Moreover, DSC measurements give an immediate overview of the effect of the thermal treatment on the material behavior. Tensile tests in this section were performed using an MTS tensile test machine equipped with a 10kN load and displacement–controlled. In following paragraphs, characterization results and treatment properties are discussed.

Strip 320C

The low-temperature treatment (320°C) corresponds to the presence of a high residual cold work content and small grain size. This corresponds to higher mechanical resistance but also to higher interfacial energy blocking the transformation. In the DSC (Figure 5-1), this condition is expressed in squat transformation peaks, distributed over a wide range of temperatures. In MTS tensile tests instead (Figure 5-2), the hysteresis area is strongly reduced with respect to the one usually observed in commercial Nitinol and its profile becomes narrow (named "leaf–shaped" in Chapter 2). The nucleation-propagation mechanism usually distinguishing SMA is not present, even if the transformation occurs.

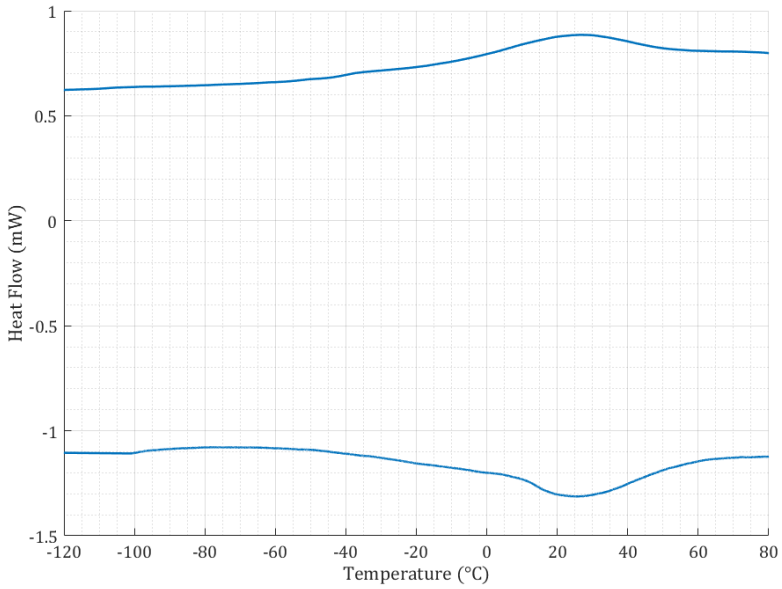

Figure 5-1 - DSC of sample 320C, total cycle

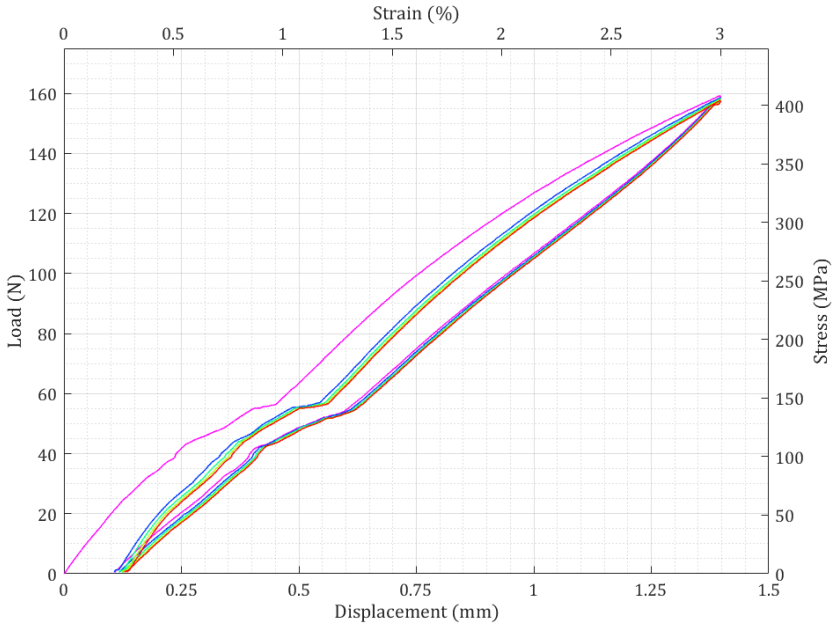

Figure 5-2 - Tensile test of sample 320C, 5 cycles

As can be noticed in Figure 5-2, there are few steps in the mechanical cycle, both in loading and unloading, around 50 N force. This is to be attributed to a fault in the control of the testing machine, due to a play in the crossbar mechanism, and not to a material feature. This can be eliminated by using the strain measured with a strain gauge as a control parameter, but this is not possible with the low–thickness strips used. This effect is repeated for all samples (Figure 5-4 and Figure 5-7).

In Table 5-1, the values of the mechanical energy for each cycle are listed. The initial decreasing from first to second cycle, so as the stabilization for the following.

Table 5-1 - Values of the mechanical energy for each cycle, sample 320C

Cycle	Areas Value (N*mm)
1	24.33
2	13.63
3	12.73
4	12.30
5	11.90

Strip 450C and 600C

Intermediate treatments (450°C and 600°C) serve to get the typical material characteristics that make it suitable for practical application. In the range 450 to 650 °C both grain size and precipitation increase the higher are the temperature and the exposure time. In the DSC thermograph (Figure 5-3 and Figure 5-6), the transformations are well defined and the R-phase is evident from the doubling of the peak during heating. Mechanically, these treatments give the material the typical pseudoelastic response of commercial polycrystalline NiTi alloys where transformation proceeds via nucleation and growth of a macroscopic martensitic domain on a stress-plateau and the mechanical energy dissipation manifests as a large closed hysteresis loop area. Treatment at 450°C forms an already stabilized material with low residual strain and is therefore a standard situation for commercial Nitinol (Figure 5-4). Treatment at 600 °C instead, is source of less stable mechanical properties (Figure 5-7) and hence this sample can be used to study functional fatigue by accelerating defect formation, which make few cycles on this material comparable to a longer life of a standard material.

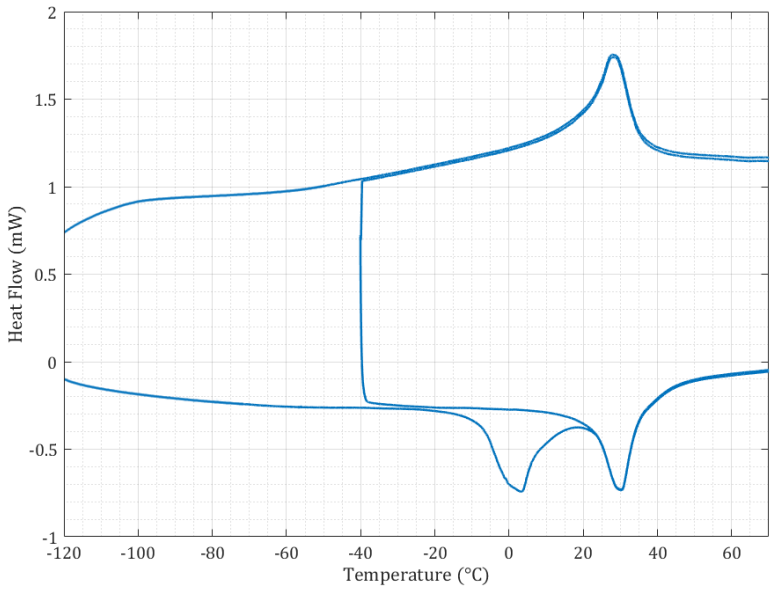

Figure 5-3 - DSC of sample 450C, total and partial cycles

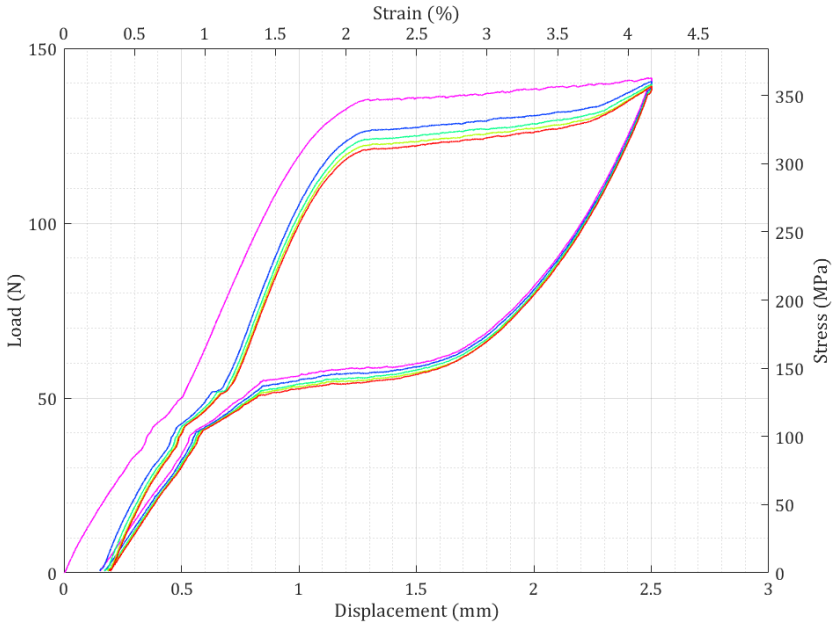

Figure 5-4 - Tensile test of sample 450C, 5 cycles

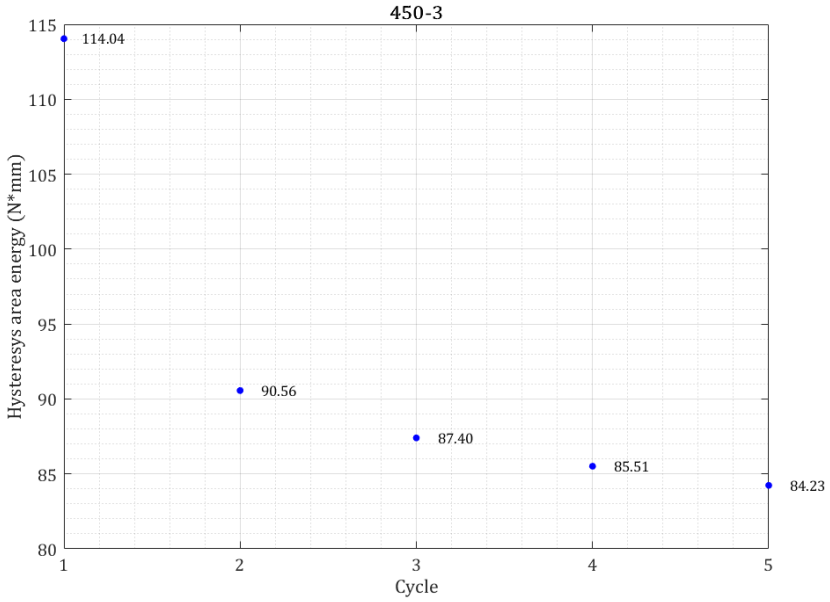

Figure 5-5 - Decay of the mechanical energy with number of cycles, sample 450C

Table 5-2 - Values of the mechanical energy for each cycle, sample 450C

Cycle	Areas Value (N*mm)	Areas Reduction (%)	Areas Reduction Difference(%)
1	**114.04**	**100.00**	
2	**90.56**	**79.41**	**20.59**
3	87.40	76.64	2.77
4	85.51	74.99	1.66
5	84.23	73.86	1.12

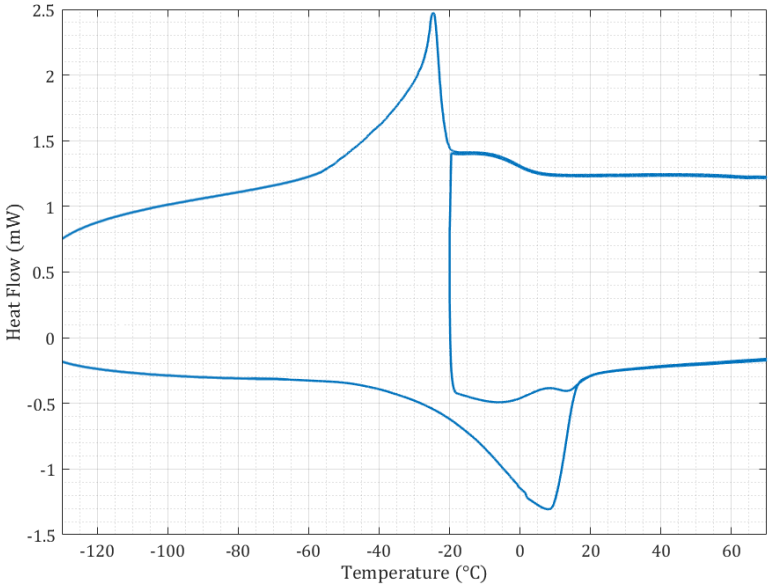

Figure 5-6 - DSC of sample 600C, total and partial cycles

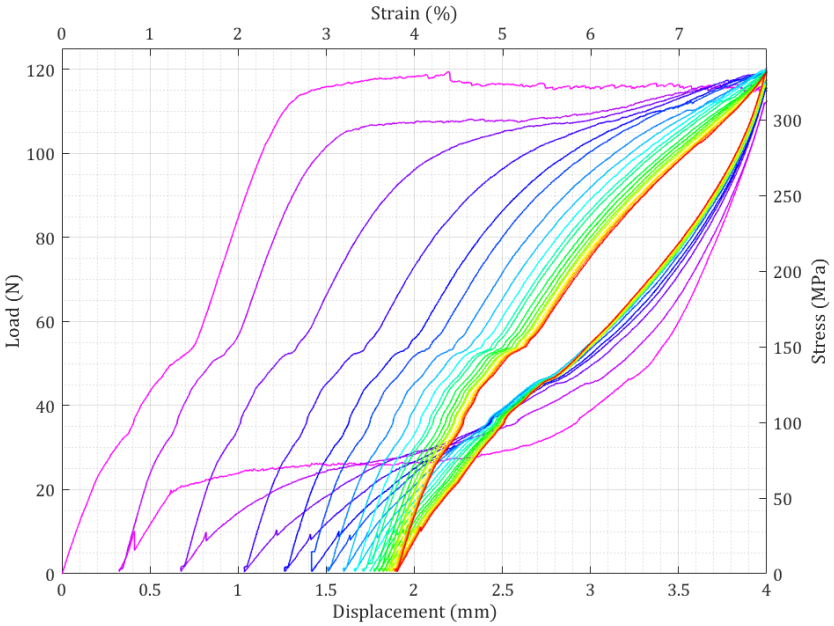

Figure 5-7 - Tensile test of sample 600C, 20 cycles

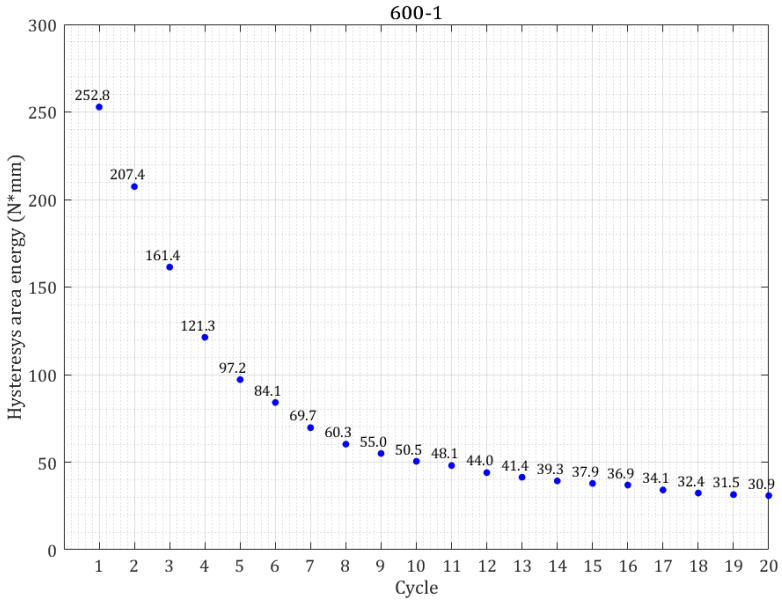

Figure 5-8 - Decay of the mechanical energy with number of cycles, sample 600C

Table 5-3 - Values of the mechanical energy for each cycle, sample 600C

Cycle	Areas Value (N*mm)	Areas Reduction (%)	Areas Reduction Difference(%)
1	**252.83**	**100.00**	
2	207.35	82.01	17.99
3	161.40	63.84	18.17
4	121.32	47.99	15.85
5	**97.16**	**38.43**	**9.56**
6	84.12	33.27	5.16
7	69.69	27.57	5.70
8	60.26	23.84	3.73
9	54.99	21.75	2.09
10	50.48	19.97	1.78
11	48.06	19.01	0.96
12	44.03	17.41	1.60
13	41.40	16.37	1.04
14	39.29	15.54	0.83
15	37.86	14.98	0.57
16	36.95	14.61	0.36
17	34.13	13.50	1.11
18	32.37	12.80	0.70
19	31.47	12.45	0.36
20	**30.91**	**12.23**	**0.22**

For the sample 450°C, the XRD measurements are performed on the first and second cycles. For the sample 600C, three cycles have been chosen, basing on the decay of mechanical energy, cycle and these are the 1st, the 5th that has a decay below 40% and the 20th that can be considered a stabilized condition.

The sample treated at 800°C (sample 800C) approaches the solubilized state. Grain size increase drastically and precipitates are dissolved. This condition gives sharp peaks in the DSC and an unimpeded nucleation and front propagation within the volume. However, the mechanical properties are low in terms of force and resistance; therefore, this case is of interest as a limit case but has not been inserted in the discussion because not relevant to the application.

5.2.3 Experimental setup

A sheets–straining setup has been realized to pull samples during diffraction data collection.

The system includes, in addition to the traction system, an aluminum disc that allows coupling with the XRD goniometer. It is designed by precisely reproducing the position and tolerances of the carvings of the original sample holders, which guarantee positioning and alignment through the pins already fixed on the goniometer.

The traction system, on the other hand, is based on a worm–screw system that creates a coupling with a crossbar. Two blocks provide the housing for the sampling system. One of the two blocks is secured to the coupling disc and accommodates the fixed gripping. The other block is connected to the crossbar through a load cell and thus accommodates the movable gripping that slides along a carriage formed by two tempered bars. This block also houses the laser sensor, whose target is applied to the fixed gripping block. The load cell and the contactless laser sensor provide real-time displacement and force data during traction and during XRD scanning.

The most important feature is that the system is designed to have the correct alignment with the diffractometer focal area. In the vertical direction (z), the gripping system is designed for the top surface of the sample to be always (regardless of the thickness of the specimen) at the exact height of the focal plane of the diffractometer. In the longitudinal direction (x), the length of the fixed block is assigned so that the illuminated area falls in the middle of the sample by excluding the gripping system.

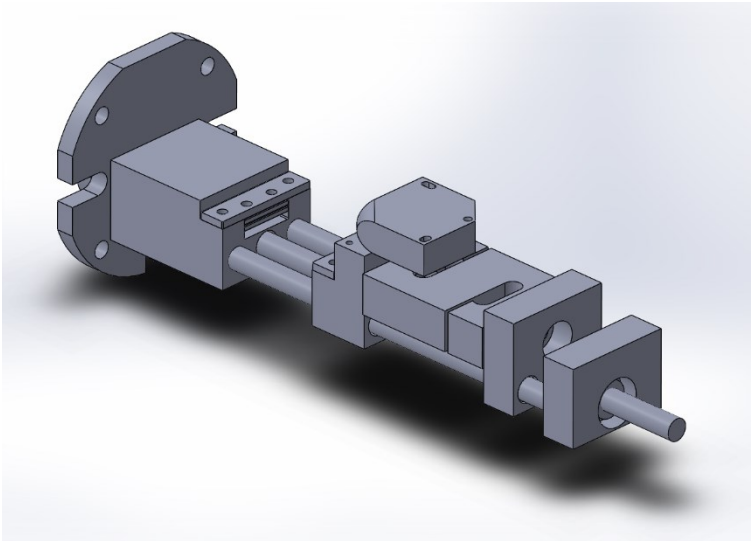

Figure 5-9 - sheets–straining setup with the aluminum coupling disc and the traction system

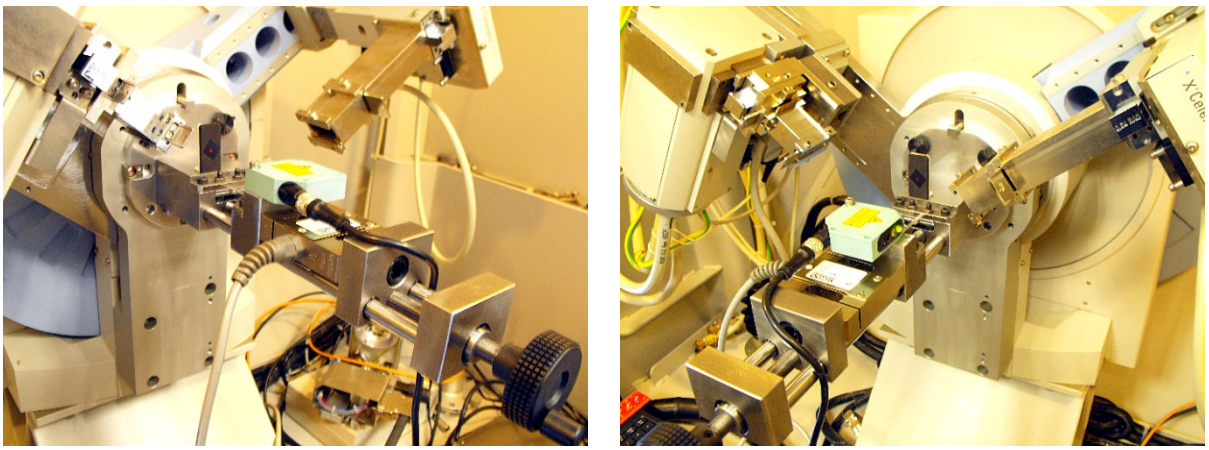

Figure 5-10 - Pictures of the sheets–straining setup mounted in the diffractometer chamber

5.2.4 Transformation mechanism

As already discussed, it is known that the behavior of SMA can be tailored through various expedients (chemical composition, thermal treatment, mechanical training), but the most manifested behavior in "early-life" commercial Nitinol is characterized by a nucleation–propagation mechanism, typical of first order military transformations. The nucleation starts at stress concentrators (reduced cross sections, holes or constraints) and then propagates throughout the material with a unique transformation front. This gives the plateau-type part of the stress–strain curve that resembles the localized Lüders-like deformation behavior in low-carbon steels (Hall, 1951; Sittner et al., 2005). It is also true that in the "leaf–shaped" curves (in particular for the cycled material, but also for the low–temperature treated), the hypothesis is that the transformation does not nucleate, but occurs homogeneously throughout the volume. A gradual change of transformation from localized to uniform with increasing number of load cycles has been suggested by several authors, based on indirect evidence (change of the slope of the strain–stress curves (Liu et al., 1999) or change of the accommodated strain recorded by digital image correlation (Kim and Daly, 2011)) and on measurements (Polatidis et al., 2015). This has been explained mainly with the presence of residual martensite or with grain reorientation due to cyclic tensile loading, both facilitating the A→M transformation by lowering the critical transformation stress. In this context, functional fatigue is not just a mere reduction of performance (recoverable deformation, generated force, and mechanical hysteresis) but is also a manifestation of a possible change of transformation mechanism. Some have also proposed that in this case, SMA martensitic transformation is no longer a first order transformation, but becomes a second order (Fabrizio et al., 2016). However, the best approach here followed to adapt the model to these microstructural conditions, is to maintain the order of transformation and the basic physics and only adapt the transformation stress of the single representative crystal to reflect the working condition after a number of work cycles.

To verify the change of transformation mechanism from "Lüders-like" to homogeneous, the samples were not thinned at the center to obtain a dog–bone shape. Without this cross–section reduction, stress concentration occurs at sample holders and accordingly nucleation starts there and then propagation front spreads throughout the material. To avoid the risk of including the gripping in the X-ray illuminated area, the distance between the holders has been designed longer than the length of the illuminating window, so the nucleation trigger–area is not captured. This allows verifying the mechanism condition: if nucleation is detected mechanically (reaching the plateau during loading), but not in the diffractogram, then this means that it is occurring in the non–illuminated area, i.e. at the extremes of the sample. On the contrary, if the fraction changes continuously both mechanically and in the diffractogram, then the homogeneous transformation hypothesis is verified.

5.2.5 XRD analysis

In situ tensile X-ray diffraction experiments were conducted using a PANalytical X'Pert X-ray diffractometer with a Cu–K_α radiation source in the Bragg–Brentano geometry. The characteristic of this instrument is the θ–θ goniometer configuration: this setup allows keeping the sample in a fixed position moving the X-rays source and collector both of an angle θ for the pattern collection. Two ranges have been selected for the analyses: $35° < 2\theta < 55°$ and $75° < 2\theta < 85°$. The option to acquire the whole pattern has been discarded because of the long time required for the measurement. A long measurement increases also the probability of stress relaxation, i.e. the time-dependent decay of applied stress under constant strain that would modify the sample state during the measurement. Therefore, a balance between the pattern accuracy, needing longer time per step, and the stability of the material under the load action has to be considered. Moreover, the diffraction peaks of the two main phases under investigation (B2 and B19') are very close among them, and this requires a reduction of the angular step for their discrimination, this imposing a longer measurement time too. As a result, the ranges of the patters not useful for the analyses have been neglected focusing the pattern on the more significant ones. The parameter chosen for the pattern collection has been a step equal to 0.008° with 120 s of time per step.

The in-situ XRD patterns were collected while halting the tensile system at specific strain values during loading/unloading of the specimens. The displacement and the force are continuously recorded to verify the stability of the mechanical conditions during the pattern collection. To reproduce a quasi-static condition, the strain rate has been kept between 0.2 to 0.3 %/min ensuring an isothermal test. The intermediate points along the cycle have been determined considering the number of pattern acquisitions in a working day to avoid leaving the sample under tension during the night. Then the specific positions have been reached by displacement control. The slope of the force has been monitored to identify the reaching of the elastic part in loading, whilst the value of the force has been used as control variable for the last point in unloading and set to less than 5 N.

During mechanical loading of superelastic SMAs, several new peaks identifying B19' appear upon the phase change from austenite (B2 cubic crystal) to martensite (B19' monoclinic crystal), and their intensities gradually increase at the expense of the austenite peaks during SIM formation.

The XRD patterns have been analyzed using MAUD software for a Rietveld refinement. Both the two angular domains collected have been used for the analyses, in order to achieve a more reliable result. Four main aspects related to the sample condition have to be here reported from the point of view of the XRD analysis. The first is related to the deformation of the crystals. All the data are collected on strips, so the samples are in a particularly textured structural condition imposed by cold rolling regardless of traction, and the consequence of this texture is usually the change of the intensity ratio among the different reflection indexes. This effect might lead to large errors in the quantitative analysis, which is mainly based precisely on intensities ratio. The second aspect is linked to the different phases existing in NiTi. The B2 and the B19' structures are easily distinguishable in the patterns, whilst other phases are not. In particular, the rhombohedral phase, here considered in two different forms, has its characteristic peaks overlapped to the ones of austenite and martensite. The third aspect is the vertical shift of the upper surface of the sample due to the shrinkage in the directions perpendicular to traction axis. This causes the reflection plane to be out of focus. The last is that the deformation of the crystals has to account for both the martensitic transformation and the elastic tensile strain. These aspects highlight that it is very important for the analysis to use jointly the information coming from both the XRD Rietveld refinement and the other experimental observations (e.g. the already cited effect of texture and elastic strain; the presence of R-phase known from DSC and mechanical characterization; the presence of precipitates). The quantitative analysis needs an iterative process – addressed to optimize the phase composition of the material observed – to be done in light of these additional information that need to be added to the refinement to ensure better quality and representation of the real situation of the samples. This can be done through some parameters offered by the software to tailor the analysis; among them a texture parameter, a z–axis shift and the presence of R-phase have been added to the refinement process to limit the error and to try including these effects. These corrections serve to improve the analysis and the fit of the experimental pattern, leaving however a certain margin of error, which is reported hereafter (associated to each quantitative analysis) through the Rwp value, addressed by the refinement software and indicating the quality of the refinement and so the reliability of the results achieved.

Strip 320C 1st cycle

Figure 5-11 displays the XRD patterns collected during the loading/unloading cycle on the sample treated at 320°C for 8 minutes (sample 320C). In the legend of this, as of the following Figures, the loading/unloading condition is indicated jointly with the number of the cycle with notation "Ln" or "Un" and the displacement/force point of pattern acquisition is specified. Here, only the Austenitic phase main peak is visible for each displacement. Increasing the displacement, a significant shift to the right, toward the position of the Martensite main peaks, can be observed.

At the same time, the peak intensity decreases and its width increases. The peaks are broadened probably due to a spread incoherent martensitic transition. Indeed, this behavior is in accordance with the character of the transition observed with other experiments: the DSC peaks are spread over a wide temperature range and the bell is not clearly detached from the baseline; the mechanical cycle is gradual and narrow, the XRD pattern changes gradually with no clear evolution of the peaks. Since the martensite formation is dispersed throughout the volume of material, the XRD lacks a significant number of reflections to discriminate the two phases and the Rietveld refinement of these patterns gives results not reliable. Consequently, no results for this sample are available.

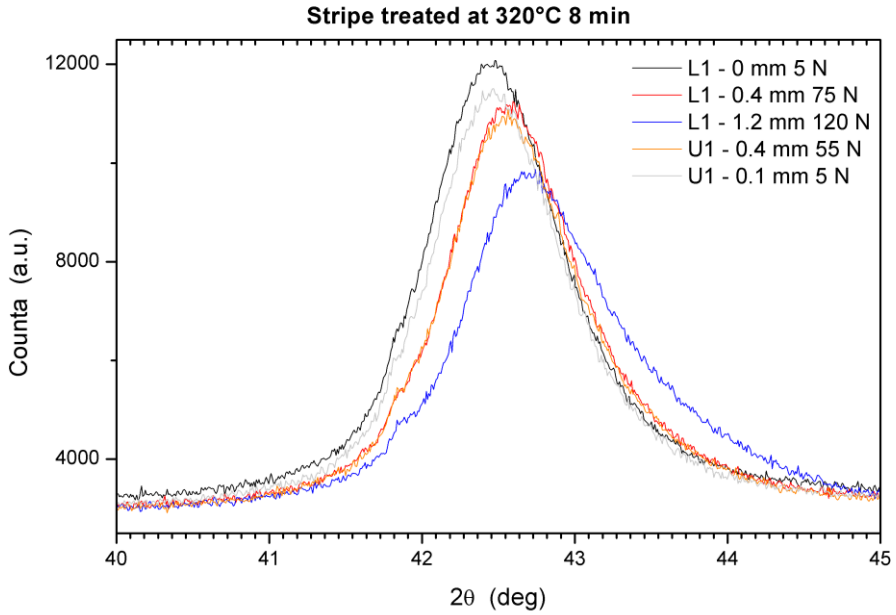

Figure 5-11 - XRD patterns collected during the first cycle, sample 320C

Strip 450C, 1st and 2nd cycle

In Figure 5-12, the data collected with the mechanical control system on the strip treated at 450°C for 10 min (sample 450C) are plotted. The dashed line reports the dedicated system sensors acquisition and the dotted line the resulting recoverable strain. The dots indicate where the XRD patterns were collected. The sample has been measured along a first loading and unloading cycle and on a second loading. The two cycles display a similar behavior indicating a good stability of the material after the heat treatment.

The results of the XRD measurement are summarized in Figure 5-13. To better display the behavior observed, the angular range has been restricted to the one of the main peaks transition. For the data of first cycle, the parameter of initial vertical shift from the perfect focus position has been set to 1 μm: the shift and the lower counts of the first cycle can be due to this aspect and to an initial compression of the strip causing a misalignment of the sample in the system. The Austenitic peak moves a lot during the experiment with a constant shift to high angles. This could be explained in different ways, e.g. with an elastic deformation under traction or with the

progressive change to the Martensitic phase. The XRD refinement addresses this as an effect of a transformation of an initial rhombohedral phase into a resulting martensite at the beginning of the second cycle.

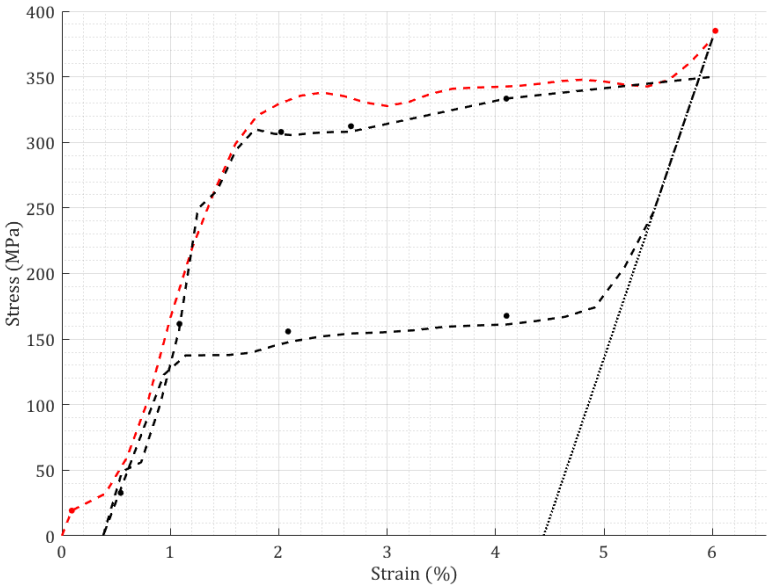

Figure 5-12 - Mechanical first and second cycles collected with laser sensor and load cell installed on the tensile system, sample 450C

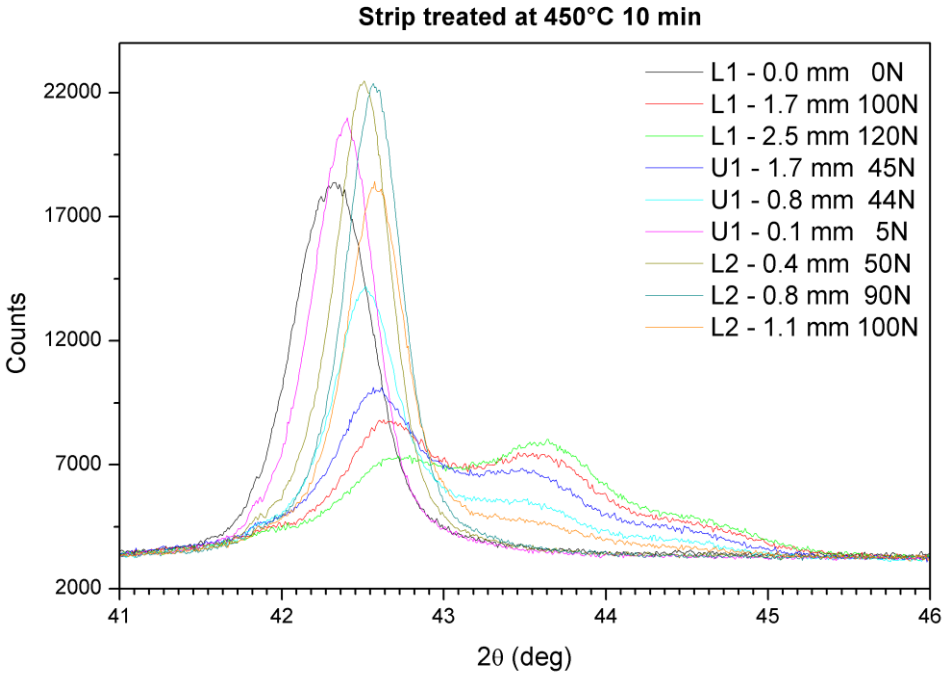

Figure 5-13- XRD patterns collected during the two cycles, sample 450C

Starting measurement (L1, l = 0 mm, F = 0 N) refinement displays the presence of an Austenitic phase with a weight fraction of 82±3% with the remaining amount associated to a Rhombohedral phase (a = 4.83 Å, b = 4.29 Å, c = 2.90 Å, beta = 88.4°). The identification of the Rhombohedral phase has been done introducing a hypothetical structure with free main structural parameters, in addition to the Austenite and Martensite phases. The structure refined leads to the parameters characteristics of NiTi Rhombohedral structure and, at the same time, indicates a null content of Martensite. The choice of considering the Rhombohedral structure has been suggested by the evidence of such a phase in DSC experiments.

At the second cycle the refinement of the condition at L2, l = 0.4 mm and F = 50 N, performed following a similar procedure, reports a final ratio of 78±1% of Austenitic phase, but the Rhombohedral phase has become a Martensitic residual phase (a = 2.59, b = 4.515, c = 4.375, gamma = 104.5°) with a content equal to 22±1%. XRD analyses suggested the presence of residual Rhombohedral phase in this sample for a fraction lower than 0.3±1%, here considered negligible. Martensite and Rhombohedral phases are really close in terms of structures, so the choice of the dominant phase in the data refinement has been led by the refined lattice parameters. In particular, the angles are reported to be greater than 90° in the case of Martensite and lower than 90° for the Rhombohedral. This result also agrees with the calorimetric analyses and the behavior observed in stress-strain experiments.

The refinement of the pattern with l = 2.5 mm and F = 120 N, where the strain effect overcomes the transformation, shows the presence of 96.0±0.1% of Martensitic phase and 4.0±0.1% of Austenite. For this refinement, a correction has to be considered to take in account the geometrical deformation of the material cell during the experiment. Fortunately, the relaxing time characteristic of the material resulted to be longer than the time required for the XRD pattern acquisition. This guaranteed the possibility to refine the patterns without any need of post-processing to correct a time dependent peak shift or broadening.

Along the stress-strain cycle, the growth of Martensitic fraction is observed with the quantitative analysis of the phases. At the point at l = 1.7 mm corresponding to F = 100 N, showed an Austenitic fraction still up to 54.3±0.7% and a Martensitic fraction equal to 45.7±0.6%.

In the following table, the results of the analyses performed along the two loading cycles and the intermediate unloading are summarized. As already stated, the Rwp value measures the fit quality: it ranges between 1 and infinite where 1 represents the perfect match point by point between the refined and the experimental patterns. The quality of the fits obtained is really good in the close to pure phases patterns: here the refinement was able to converge to stable solutions and the results are reliable. In some of the intermediate cases, especially close to the start and the end of the transition regimes, the correct matching of the peaks required some preliminary considerations related to the physics of the system analyzed. In fact, the multiple local minima corresponding to different sets of refined parameters may generate also solutions without a physical meaning.

Table 5-4 - Results of XRD pattern analysis, sample 450C

Cycle step	Austenite	Martensite	Rwp
L1 – 0 mm 5 N	82±3%	18±3% (R)	2.17
L1 – 1.7 mm 100 N	54.3±0.7%	45.7±0.6%	1.34
L1 – 2.5 mm 120 N	4.0±0.1%	96.0±0.1%	1.71
U1 – 1.7 mm 50 N	7±2%	93±2% (1±2%(R))	2.94
U1 – 0.8 mm 45 N	36±2%	64±2%	2.11
U1 – 0.1 mm 10 N	81±3%	19±3%	2.12
L2 – 0.4 mm 50 N	78±1%	22±1%	2.24
L2 – 0.8 mm 90 N	69±3%	31±3%	2.07
L2 – 1.1 mm 90 N	68±2%	32±2%	2.32

Strip 600C – 1st cycle

Figure 5-14 reports the first stress/strain cycle for the sample treated at 600°C for 10 min (sample 600C). Here too, the dashed line reports the dedicated system sensors acquisition and the dotted line the resulting recoverable strain. The dots indicate where the XRD patterns were collected. Mechanical data previously collected indicate a high initial instability of the phase with the mechanical cycling. The effect is a significant residual strain at the end of the cycles and an evolution of the Martensitic fraction is expected from the patterns collected at different cycles. Due to this complex behavior of the material, the reliability of the XRD refinement is decreased as respect to the one for the previous samples.

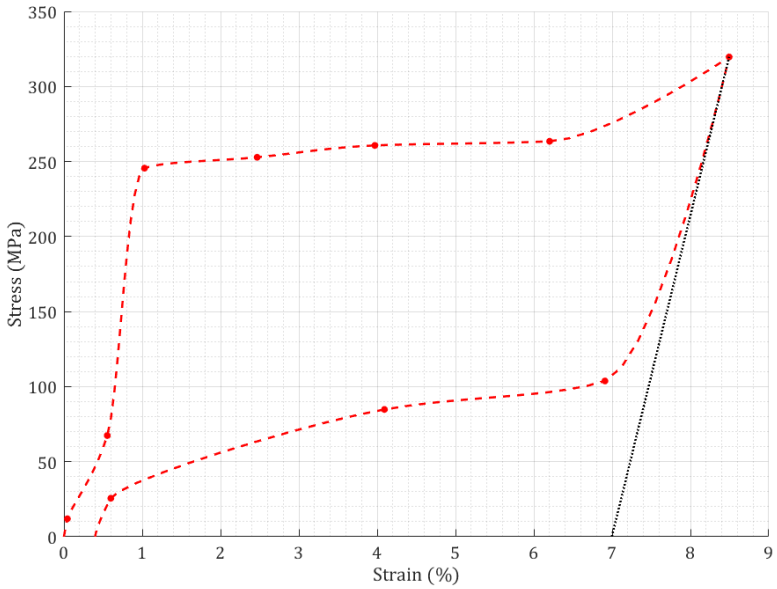

Figure 5-14 - Mechanical 1st cycle collected with laser sensor and load cell installed on the tensile system, sample 600C

The XRD patterns corresponding to the first cycle are reported, following the same standard indicated previously, in Figure 5-15. The first evidence is the high intensity obtained on the sample at the initial state indicating a perfect alignment of the sample into the instrument. In this sample, the peaks corresponding to the Austenitic phase are narrower than before, allowing an easy phase

identification. However, it can be observed in Table 5-5, summarizing the refinement results, that the final quality of the refinement is not improved. Here, the problem of the fit is associated to the presence of the peak at $2\theta = 44.3°$ not associated to any reflection of the Austenite. The peak is reported to be proper of the (422) reflection of $NiTi_2$ precipitates (Fall et al., 2014). Having no other reflections in the analyses range, the quality of the refinement is strongly reduced. In Figure 5-16, an example of the obtained result for a refinement considering the $NiTi_2$ precipitate phase is reported: despite the good agreement, the quantitative analyses display a Rwp>6.

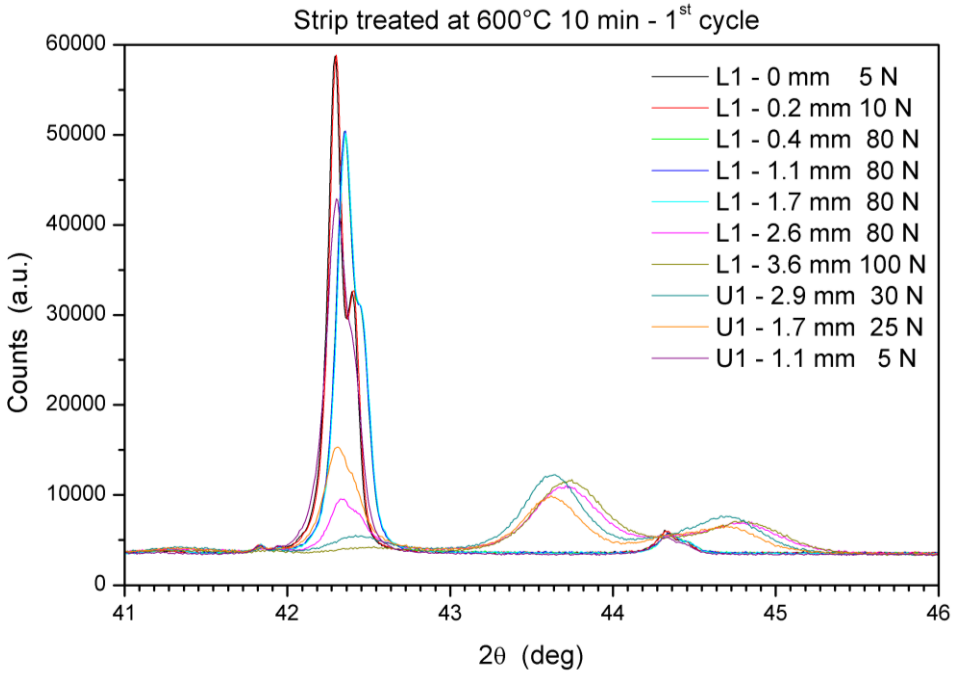

Figure 5-15 - XRD patterns collected during the 1st cycle, sample 600C

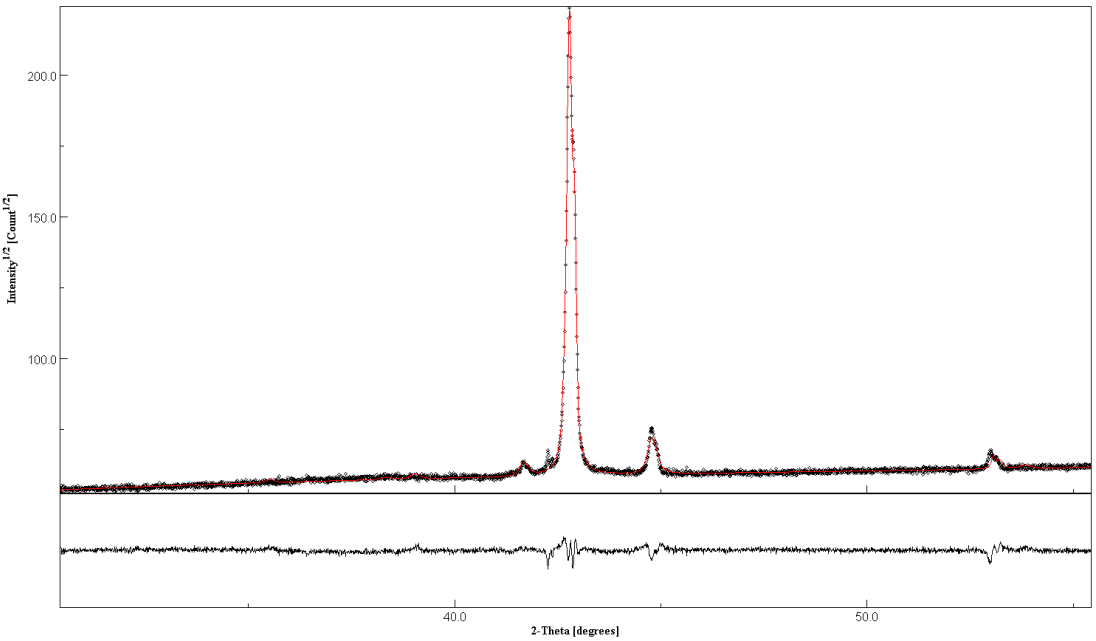

Figure 5-16 - Example of the obtained result for a refinement considering $NiTi_2$ precipitate phase, sample 600C cycle 1

The XRD patterns for L1, 0.4 mm, 1.1 mm and 1.7 mm at 80 N, are essentially the same. No shifts and no change in intensities of the peaks are observed along the elongation of the sample. The only visible aspect is a low shift to higher angle (from 42.352 to 42.358 degrees) of the main peak. This shift may be due to an increase of the martensitic phase, but it is probably mainly ascribable to the effect of the mechanical deformation of the sample, taking place during the measurements. From the stress-strain points associated with these three scan, it is also known that they lie in different positions on the loading plateaux. Therefore, an evolution of the martensitic phase fraction would be expected, whilst it does not appear, and the only way to explain this behavior is related to the nature of the transformation into this type of sample. In fact, during the first loading of the first cycle for sample 600C, the martensitic transformation does not occur homogeneously (as was for the sample 320C and for the second cycle of sample 450C), but instead the process takes place following the theory of the Lüders bands. In this scenario, the nucleation and then the martensitic initial growth start in the region close to the clamps, where there is the stress concentration for rectangular samples. Here, as previously explained in Section 5.2.4, X-rays do not scatter with the sample and then no transformation is detected proving the Lüders–like transformation. To overcome the non–detection of martensite nucleating at holders, dog bone shaped samples could be prepared, obtaining the concentration of stress to be in the irradiated part of the material. In our case, this was not done to attest the difference between homogeneous and nucleation–propagation mechanism and moreover because the width of the sample would have become not sufficient. The effects on pattern refinement analyses results are visible in the similar results obtained for the Martensitic fraction in the three cases, but at the same time, the high error on the final values and the similar high values in Rwp parameter for the refinements.

Table 5-5 - Results of XRD pattern analysis, sample 600C, cycle 1

Cycle step	Austenite	Martensite	Rwp
L1 – 0 mm 4 N	98±1%	2±1%	9.90
L1 – 0.25 mm 10 N	97±5%	3±5%	5.21
L1 – 0.5 mm 80 N	90±5%	10±5%	6.62
L1 – 1.1 mm 80 N	91±3%	9±3%	4.73
L1 – 1.7 mm 80 N	89±3%	11±3%	2.75
L1 – 2.6 mm 80 N	14±2%	86±2%	6.78
L1 – 3.6 mm 100 N	2±1%	98±1%	6.85
U1 – 1.6 mm 30 N	12±2%	88±2%	5.09
U1 – 0.4 mm 25 N	30±2%	70±2%	8.22
U1 – 0.2 mm 5 N	91±2%	9±2%	3.25

Strip 600C – 5th cycle

Figure 5-17 reports the fifth cycle for the sample 600C. The dashed line reports the dedicated system sensors acquisition and the dotted line the resulting recoverable strain. The dots indicate where the XRD patterns were collected. The mechanical behavior follows the expected evolution related to the material stabilization also reported in Figure 5-7. The residual strain is increasing

significantly at each cycle and the shape of the hysteresis cycle assumes the already cited "leaf–shaped" characteristic. The intermediate cycles have been performed following the strategy described above paying attention to avoid overheating of the material due to fast transformations. The upper limit of the strain has been set equal for all the cycles following the first, up to 8%, in order not to introduce possible additional effects into the experiment.

The patterns obtained for the 5th cycle of the 600C sample are reported in Figure 5-18 and the results on the Martensitic fraction summarized in the following table.

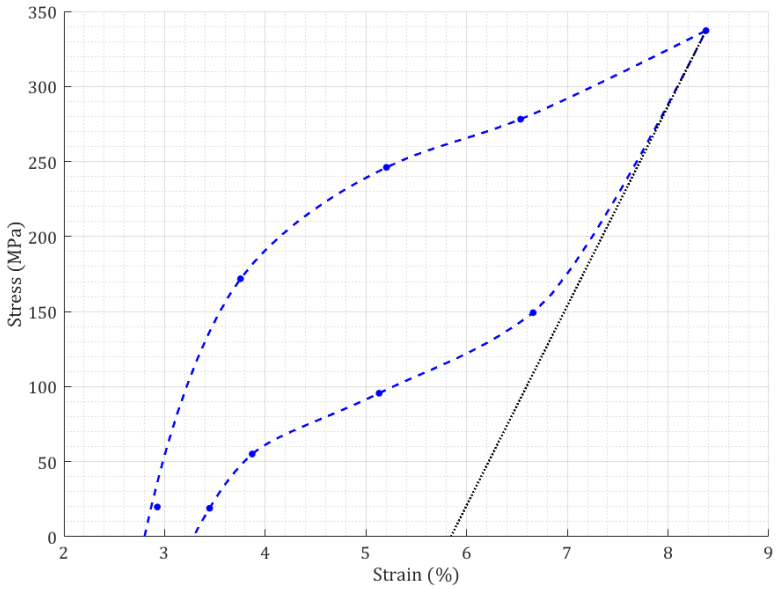

Figure 5-17 - Mechanical 5th cycle collected with laser sensor and load cell installed on the tensile system, sample 600C

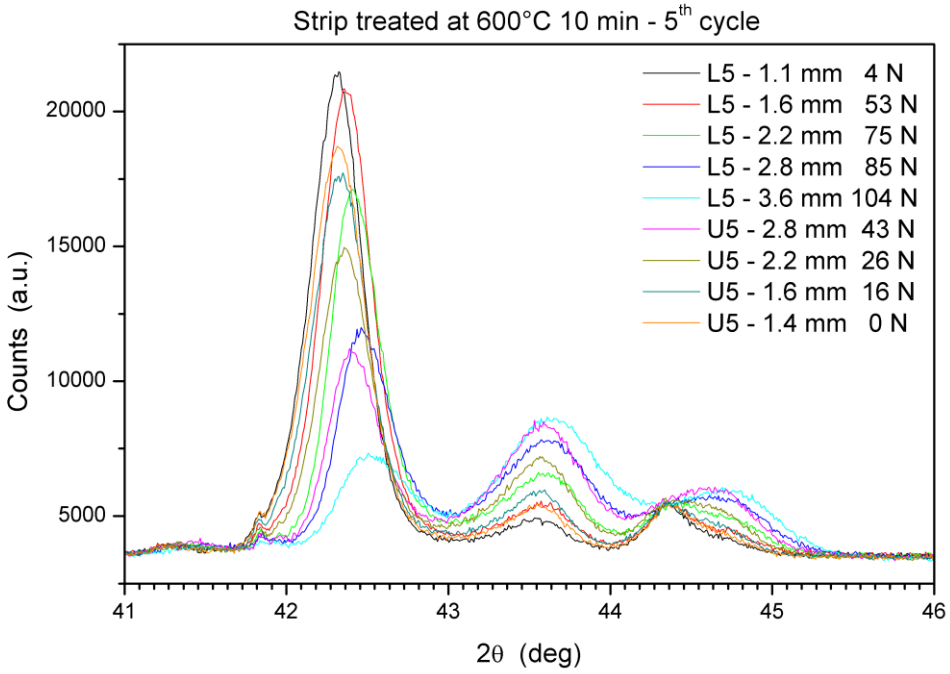

Figure 5-18 - XRD patterns collected during the 5th cycle, sample 600C

The 5th cycle displays a higher stability of the solutions of the patterns refinements. The Rwp values result almost constant for all the analyses and its absolute value suggests a lack of precision in the obtained solution: this is mainly due to the fit of the peak corresponding to the B19' (110) reflection. Indeed, the refinement process matches the peak position but miss significantly its shape in terms of symmetry and broadening and this inaccuracy can affect also the quantitative values obtained for the Martensitic fraction. The fit of the Austenite peaks is always correct in terms of scale, position and shape, so the quantitative analyses suffer mainly of Martensitic phase determination. This aspect is common to all the patterns analyzed for 5th cycle. Increasing the number of cycles, the effect should be reduced thanks to the mechanical stabilization of the material.

Looking at the results of the 5th cycle in Table 5-6, another aspect evident is the reduction of the hysteresis: the difference between the fraction values at the same strain is lower with respect to the 1st cycle highlighting a lower hysteresis associated with the single mechanical cycle. Moreover, the rate of the transformation is symmetric with respect to the inversion point at maximum strain. Considering for example the values corresponding to 2.2 mm (around half way), they are close each other (Martensite fraction = 47% and 53.5%) and symmetric (53% of Austenite and 47% of martensite in loading becomes respectively 46.5% and 53.5% in unloading). Moreover, the increment of the residual Martensite for the single cycle is reduced (was 7% in 1st cycle and is 4% in 2nd cycle) indicating the material stabilization.

Another effect that can be observed in this cycle is the disappearance of the Lüders bands behavior of the Martensitic transformation. The martensite fraction changes gradually with loading and is always revealed by the XRD scan and this proves that transformation occurs in the whole material volume and do not start only in the parts near the clamps that are not illuminated. The stabilization of the material from the mechanical point of view is reflected by a homogenization of the Martensitic phase nucleation into the Austenitic starting matrix.

Table 5-6 - Results of XRD pattern analysis, sample 600C, cycle 5

Cycle step	Austenite	Martensite	Rwp
L5 – 1.1 mm 4 N	70±2%	30±2%	3.47
L5 – 1.6 mm 53 N	68±2%	32±2%	3.43
L5 – 2.2 mm 75 N	53±1%	47±1%	3.19
L5 – 2.8 mm 85 N	23±1%	77±1%	3.21
L5 – 3.6 mm 104 N	4.2±0.7%	95.8±0.7%	3.18
U5 – 2.8 mm 43 N	25±1%	75±1%	3.39
U5 – 2.2 mm 26 N	46.5±0.7%	53.5±0.7%	3.04
U5 – 1.6 mm 16 N	68±2%	32±2%	2.53
U5 – 1.45 mm 0 N	66±3%	34±3%	3.36

Strip 600C – 20th cycle

At the 20th cycle, the material has reached the mechanical regime condition. The data collected during the XRD experiment are reported in Figure 5-19. The residual strain after the cycling has become stable and the unloading curve goes back to the starting value of strain. The patterns are reported in Figure 5-20, followed by the table summarizing the results of the Rietveld refinements. It can be observed that the peaks intensity and the general quality of the patterns decrease with the material cycling (i.e. with respect to cycles 1st and 5th of the same sample). In fact, a gradual broadening of the peaks corresponding to the Austenitic phase can be seen and this can be attributed to the presence of the residual Martensite at low strain.

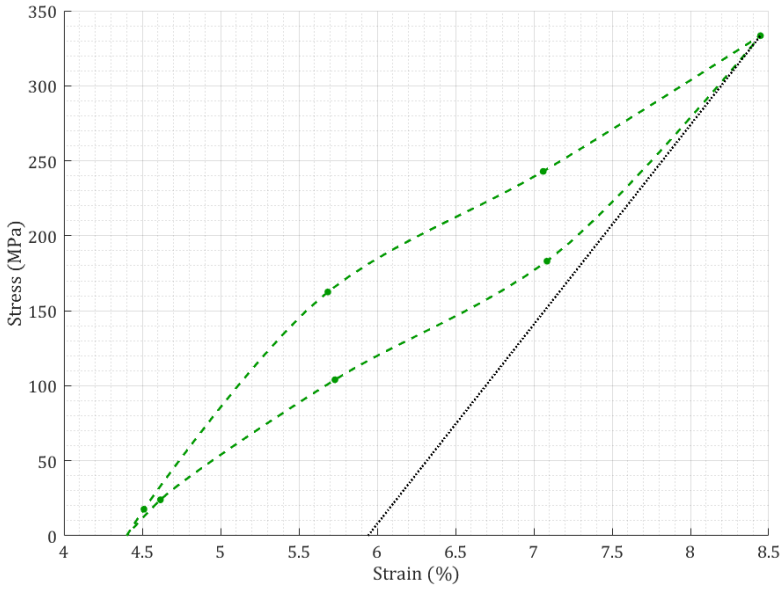

Figure 5-19- Mechanical 20th cycle collected with laser sensor and load cell installed on the tensile system, sample 600C

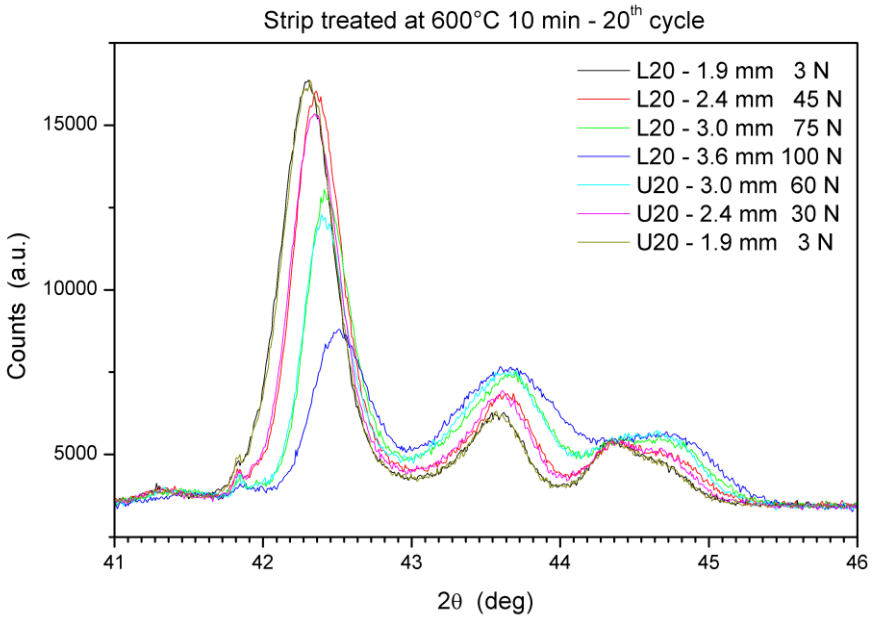

Figure 5-20 - XRD patterns collected during the 20th cycle, sample 600C

The Rietveld refinements related to this last experimental cycle seems to support this explanation (an increase of the Martensitic residual phase) for the broadening of the peaks. In addition, the structural refinement related to the Martensitic phase suggests a structural distortion of the basic cell for low stress indicated deformed (probably because restricted) martensite. The patterns refinement shows similar quality of the results obtained with similar Rwp. The highly symmetric behavior and little hysteresis observed on stress/strain curves finds a good agreement with the quantitative analyses of the patterns, similarly to what discussed for 5th cycle.

Table 5-7 - Results of XRD pattern analysis, sample 600C, cycle 20

Cycle step	Austenite	Martensite	Rwp
L20 – 1.9mm 3N	62±2%	38±2%	2.84
L20 – 2.4mm 45N	57±2%	43±2%	3.28
L20 – 3.0mm 75N	35±2%	65±2%	3.42
L20 – 3.6mm 100N	10±1%	90±1%	2.96
U20 – 3.0mm 60N	32±4%	68±4%	3.21
U20 – 2.4mm 30N	57±3%	43±3%	3.09
U20 – 1.9mm 3N	61±1%	39±1%	2.55

5.3 Stress-fraction relationship

Hereafter, the analysis on the Stress-fraction relationship is presented for each sample, firstly basing on Equations (5-4) and (5-5). The analytical expression is used to calculate the fraction starting from the stress-strain values for the complete mechanical cycles (using the data collected with the instruments of the tensile system) and for the acquisition points. These are displayed in the Figures of this section with dashed line and coloured circles, respectively. Colored circles correspond to the dots in the Figures of previous section and indicate where the XRD patterns were collected; then, also the experimental XRD results are available for these points and are indicated in the graph with colored squares with the linked confidence interval. To consider both the error interval of the fraction measured and the quality of the refinement, the confidence interval has been calculated as the product of these two quantities.

Strip 450C 1st and 2nd cycle

The start and finish points of the cycle, where analytic assumption foreseen none and complete martensitic fraction respectively, gives good agreement also in experimental results, even if the experimental measured fraction at the end of the cycle is not 100%.

For other points, with the exception of a light orange dot on the loading plateaux, experimental and analytical values are not fully in agreement. In particular, the experimental fraction values are higher than the analytical values for $\xi < 50\%$ whilst are lower for $\xi > 50\%$. This may be attributed to the fact that the measurements are made on the second cycle that may already include a residual martensitic content not covered by the analytical formula.

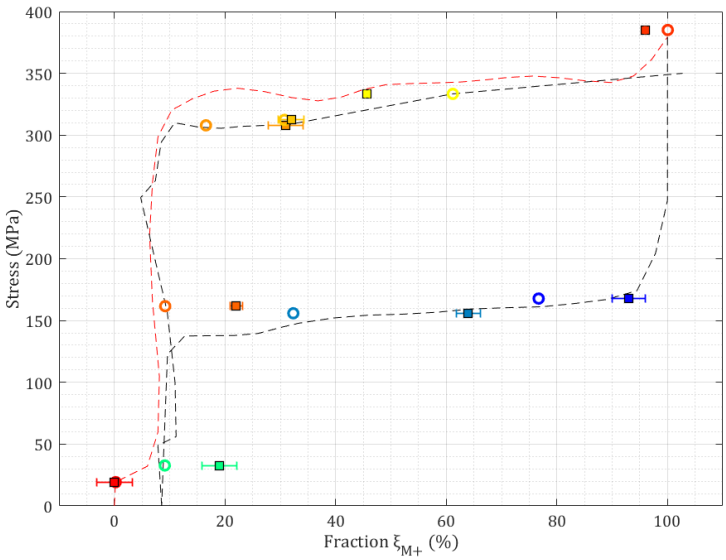

Figure 5-21 - Analytical (dashed lines and circles) and experimental (squares) comparison of the stress–fraction relationship. Sample 450C, cycles 1 and 2

Strip 600C – 1st cycle

In this sample, the problem aforementioned of Lüders bands can be recognized very well. The points in the elastic part, two in loading and one in unloading, are well represented by experimental measurements. On the contrary, when nucleation and initial propagation of martensite is identifiable through the mechanical triggering of the plateaux (the first three circles of the plateaux), the experimental measurement remains nearly constant. This means that the martensite is generating in the area of stress concentration outside from the illuminated area of diffraction. Then, when the transformation involves the illuminated area, the fraction measured suddenly reaches the analytically predicted values. Indeed, it is even higher than the foreseen fraction, whilst the opposite could have been expected, as a volume of transformed material is outside of the measuring area. In the final part, again the measured fraction is quite similar to the expected one, especially where it is near 100%, whilst the values are less accurate in the plateaux.

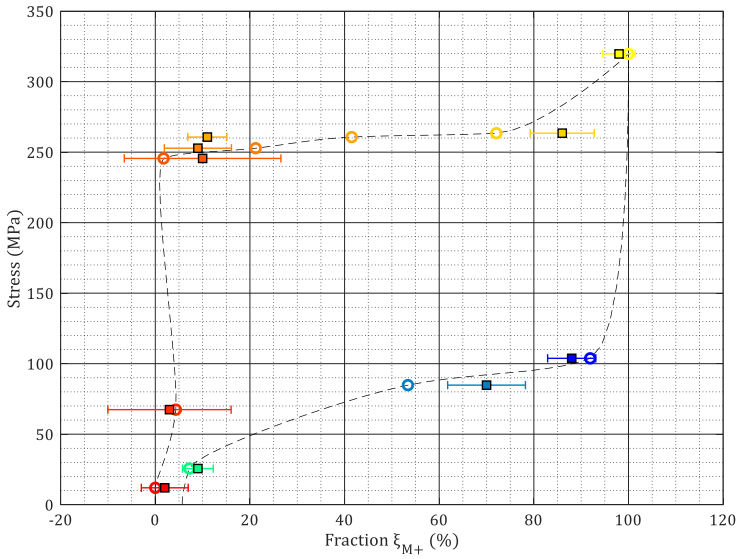

Figure 5-22 - Analytical (dashed lines and circles) and experimental (squares) comparison of the stress–fraction relationship. Sample 600C, cycle 1

Strip 600°C – 5th and 20th cycle

For subsequent cycles, the first question to be clarified is whether updating the values of elastic moduli and maximum strain according to the current cycle can serve to a more accurate prevision. I.e. if the characterization of these parameters has to be repeated (following the usual procedure, but applied to the actual hysteresis loop) or if the values obtained from the initial characterization of first cycle are still valid. This is easily verified, evaluating the analytical expression both with the original values of the first cycle and with the values recalculated at the current cycle. Results are reported in the following four figures.

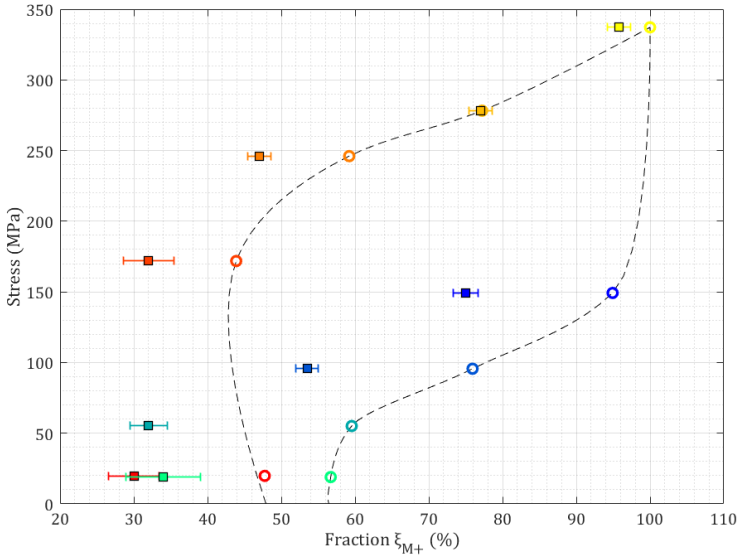

Figure 5-23 - Analytical (dashed lines and circles) and experimental (squares) comparison of the stress–fraction relationship. Sample 600C, cycle 5.
Values of E_A, E_M, ε_T updated at the current cycle.

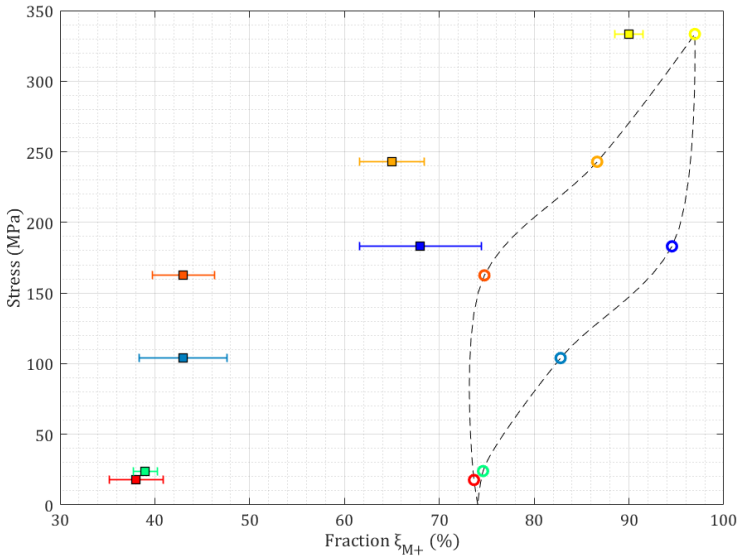

Figure 5-24 - Analytical (dashed lines and circles) and experimental (squares) comparison of the stress–fraction relationship. Sample 600C, cycle 20.
Values of E_A, E_M, ε_T updated at the current cycle.

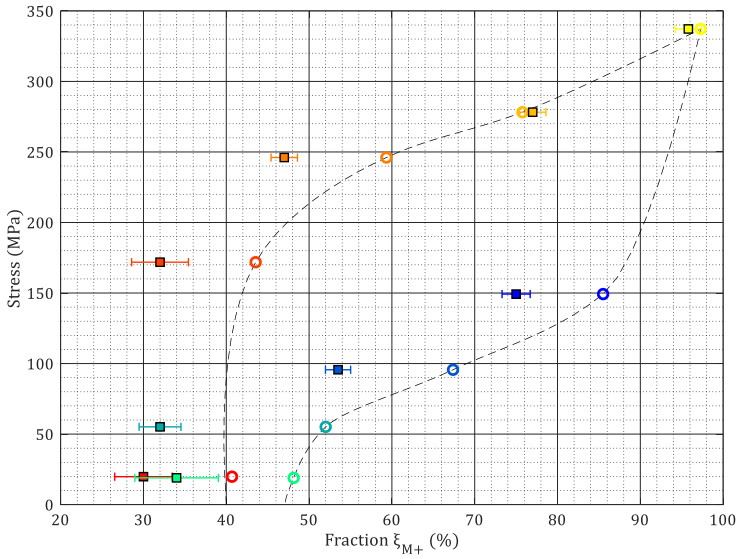

Figure 5-25 - Analytical (dashed lines and circles) and experimental (squares) comparison of the stress–fraction relationship. Sample 600C, cycle 5.
Values of E_A, E_M, ε_T maintained from the first cycle.

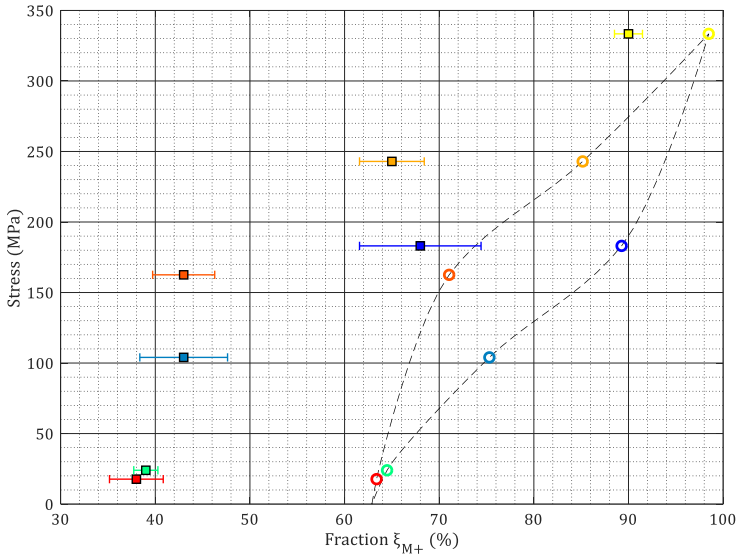

Figure 5-26 - Analytical (dashed lines and circles) and experimental (squares) comparison of the stress–fraction relationship. Sample 600C, cycle 20.
Values of E_A, E_M, ε_T maintained from the first cycle.

Figure 5-23 and Figure 5-24 shows, for cycle 5 and cycle 20 respectively, the results of the analytical calculation using values updated at the current cycle, compared to the experimentally derived martensitic fraction. Figure 5-25 and Figure 5-26 are the same, but using always the same values of the first cycle. In Table 5-8, the values used are listed. It is evident looking at these Figures, and especially Figure 5-24 and Figure 5-26 for cycle 20, that analytical forecasting improves much, especially at the beginning of the cycle, using the parameters obtained from the characterization of the first cycle. This is not only because the predicted values are closer to the experimental ones (moving to lower values), but mostly because their relative position, which creates the "shape" of the hysteresis cycle, is improved. This is indeed a proof of the physical character of these variables. The current elastic modulus is already calculated by weighing with

martensite fraction, and also the maximum transformation strain is a characteristic parameter of the lattice cell of the martensitic variant, so it is truthful that they are parameters of the material independent of the number of cycles underwent.

Table 5-8 - Values of physical parameter for the material, from the characterization of the mechanical cycles

	Cycle 1	Cycle 2	Cycle 3
E_A	27.211 GPa	15.477 GPa	15.925 GPa
E_M	21.350 GPa	13.305 GPa	12.321 GPa
ε_T	0.0700	0.0584	0.0594

The effect of Lüders bands is no longer visible: the fraction changes from the beginning of the mechanical cycle and is always detectable with XRD diffraction and this means that the transformation becomes homogeneous in the volume. This does not exclude that transformation proceeds by nucleation and propagation, but only that nucleation does not trigger only at the gripping due to stress concentration, propagating in a unique front, but that it starts all within the volume, probably because the residual (untransformed) martensite nuclei dispersed in volume serve by catalyst of the transformation.

To improve the analytical evaluation of the phase fraction for subsequent cycles, the idea to change the formula considering the plastic strain usually neglected. In this case, the strain (considering only the positive martensite variant) becomes:

$$\varepsilon = \xi_A \varepsilon_A + \xi_+ \varepsilon_+ + \varepsilon_{PL} = (1 - \xi_+)\varepsilon_A^{El} + \xi_+ \left(\varepsilon_+^{El} + \varepsilon_+^{Tr}\right) + \varepsilon_{PL} \tag{5-6}$$

Making explicit the elastic and the transformation parts of the austenitic and martensitic strain and reversing the formula to obtain martensitic fraction, Equation (5-8) is obtained.

$$\varepsilon = (1 - \xi_+)\frac{\sigma}{E_A} + \xi_+ \left(\frac{\sigma}{E_M} + \varepsilon_+^{Tr}\right) + \varepsilon_{PL} = \frac{\sigma}{E_A} + \xi_+ \left(\frac{\sigma}{E_M} - \frac{\sigma}{E_A} + \varepsilon_+^{Tr}\right) + \varepsilon_{PL} \tag{5-7}$$

$$\xi_+ = \frac{\varepsilon(t) - \frac{\sigma(t)}{E_A} - \varepsilon_{PL}}{\sigma(t)(1/E_M - 1/E_A) + \varepsilon_T} \tag{5-8}$$

The question is now evaluating the amount of plastic strain. The first attempt is to consider the whole residual strain as a plastic strain. The result of this try is reported in Figure 5-27 and Figure 5-28. Considering all the residual as plastic, the analytical curve is totally shifted to zero and this is by no means representative of the experimental result. Even in this case the justification lies in the physics of the material. The residual strain observed is not completely plastic strain, because even if a part of plasticity is induced by cycling, the material never reaches the true plastic region. Instead, it is neglected that there is a part of untransformed (retained, blocked) residual martensite, which is actually what happens.

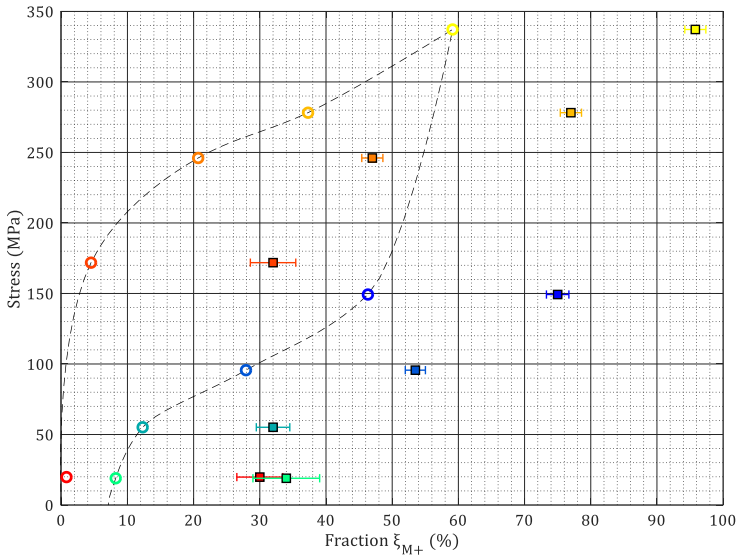

Figure 5-27 - Analytical (dashed lines and circles) and experimental (squares) comparison of the stress–fraction relationship. Sample 600C, cycle 5.
Correction with $\varepsilon_{Residual} = \varepsilon_{Plastic}$

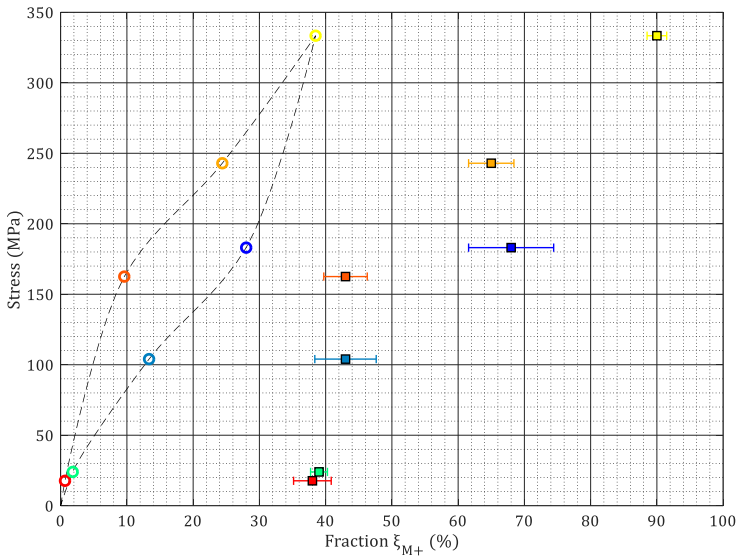

Figure 5-28 - Analytical (dashed lines and circles) and experimental (squares) comparison of the stress–fraction relationship. Sample 600C, cycle 20.
Correction with $\varepsilon_{Residual} = \varepsilon_{Plastic}$

To consider this aspect, can be assumed that the residual strain is the sum of a plastic contribution and of the retained martensite: ε_M^*.

$$\varepsilon_{residual} = \varepsilon_{PL} + \varepsilon_M^* \tag{5-9}$$

Assuming that this retained martensite is blocked in the full-detwinned condition, the strain ε_M^* can be calculated as the maximum transformation strain, multiplied by the fraction of retained martensite:

$$\varepsilon_M^* = \xi_M^* * \varepsilon_T \tag{5-10}$$

The fraction of retained martensite can be taken from the quantitative analysis of XRD diffraction in Table 5-6 and Table 5-7. The residual mechanical strain is given by mechanical tests in Figure 5-17 and Figure 5-19. From these values the strain due to retained martensite can be calculated using $\varepsilon_T = 0.07$ and then the plastic strain to be inserted in Equation (5-8). Results are shown in Figure 5-29 and Figure 5-30.

Table 5-9 - Values of strain due to retained martensite

	Cycle 5	Cycle 20
Retained martensite, measured ξ_M^*	30±2%	38±2%
Residual mechanical strain, measured $\varepsilon_{Residual}$	0.028	0.044
Retained martensite strain ε_M^*	0.021	0.0266
Plastic strain ε_{PL}	0.007	0.0174

The results are quite good. Especially the fraction values for low stress (at the beginning and finish of the cycle) are correctly resembled. The only inaccuracy is in the maximum fraction reached that is lower than the experimentally measured.

Despite this inaccuracy in the final part, knowing that the martensitic fraction reached at the end of the transformation will be underestimated, this approach can be used to obtain the stress–fraction relationship for the material, to be used as a parametric expression of the energy barrier stress. Formula (5-8) can be used to calculate the martensitic fraction from the stress–strain values of mechanical cycles and then the same stress used is taken as energy barrier stress linked to the fraction calculated. To validate this solution, the mechanical behavior of cycle 5 and 20 is simulated in the following section.

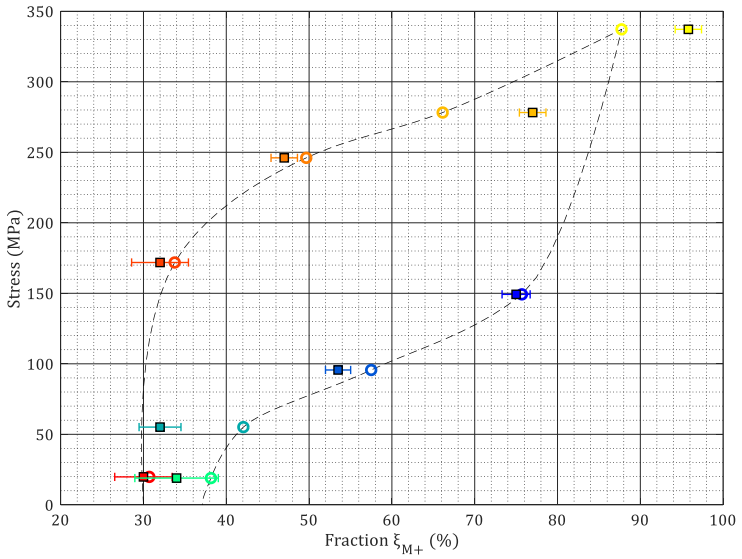

Figure 5-29 - Analytical (dashed lines and circles) and experimental (squares) comparison of the stress–fraction relationship. Sample 600C, cycle 5.
Correction with $\varepsilon_{Residual} = \varepsilon_{Plastic} + \varepsilon_{Retained}$

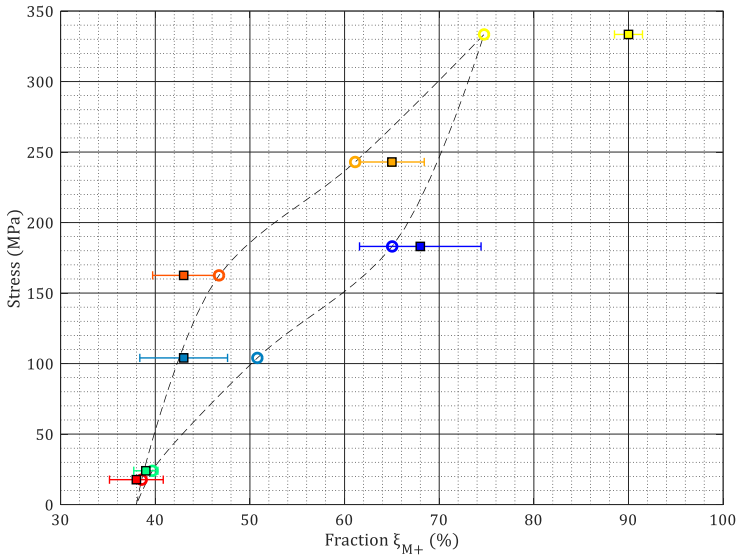

Figure 5-30 - Analytical (dashed lines and circles) and experimental (squares) comparison of the stress–fraction relationship. Sample 600C, cycle 20.
Correction with $\varepsilon_{Residual} = \varepsilon_{Plastic} + \varepsilon_{Retained}$

5.4 Numerical validation

To validate the expression obtained in previous section for the transformation stress as a function of the martensitic fraction, the same model used in Chapter 2 has been implemented, considering the parameters of sample 600C in the measured cycles 1, 5 and 20. The pseudoelastic tensile behavior obtained with the model is then compared to the experimental results.

Formula (5-8) with the values of Table 5-9 is used to calculate the energy barrier stress, which is then implemented as interpolation in Comsol. It is also necessary to modify the expressions of strain and stress variables in accordance with Equations:

$$\varepsilon = \frac{du}{dx} + \varepsilon_{PL} \tag{5-11}$$

$$\sigma = \frac{(\varepsilon - \varepsilon_T(\xi_+ - \xi_-) - \varepsilon_{PL})}{(\xi_+ + \xi_-)/E_M \; + \; \xi_A/E_A} \tag{5-12}$$

The following Figures shows the interpolated curves of the energy barrier stress as a function of the martensitic fraction for the three cycles (Figure 5-31, Figure 5-33 and Figure 5-35). The interpolation on the points directly from the experimental tests used in these simulations can be substituted by an analytical expression based on logarithms. The risk is to introduce coefficients and parameters not based on physics but motivated only by mathematics.

Figure 5-32 (cycle 1), Figure 5-34 (cycle 5) and Figure 5-36 (cycle 20) show the comparison between the experimental mechanical curves acquired during diffraction tests and the simulation results from Comsol. Even if the proposed formulation underestimates the martensitic fraction at the end of the transformation (i.e the maximum stress/strain point in the cycle is not reached at 100% martensitic fraction), the simulation results perfectly resemble the experimental curves. Then, further modifications to that formula are definitely desirable but not indispensable if only the macroscopic effect of the actuator is desired

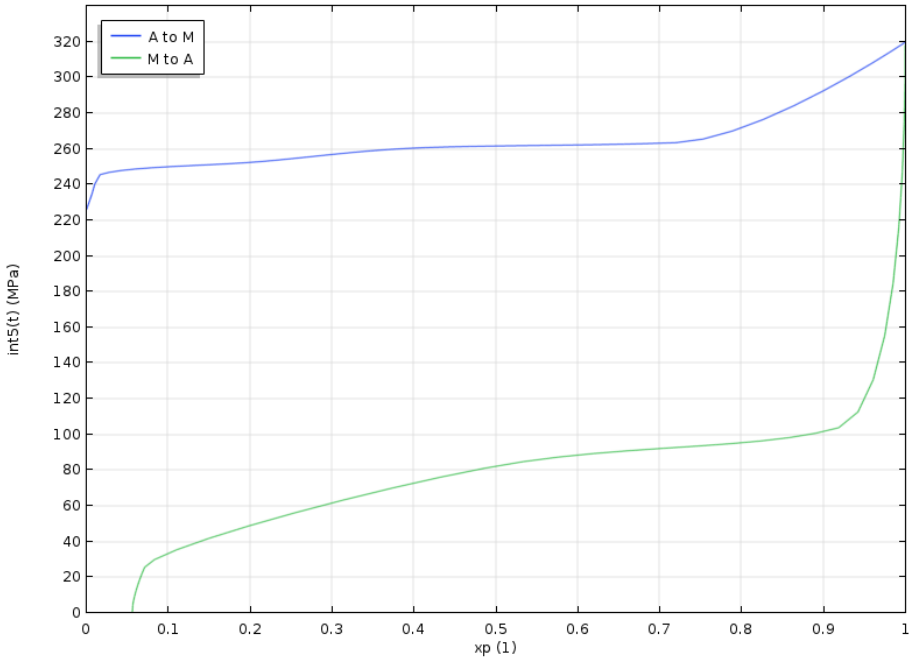

Figure 5-31 - Energy barrier stress as a function of the martensitic fraction, cycle 1

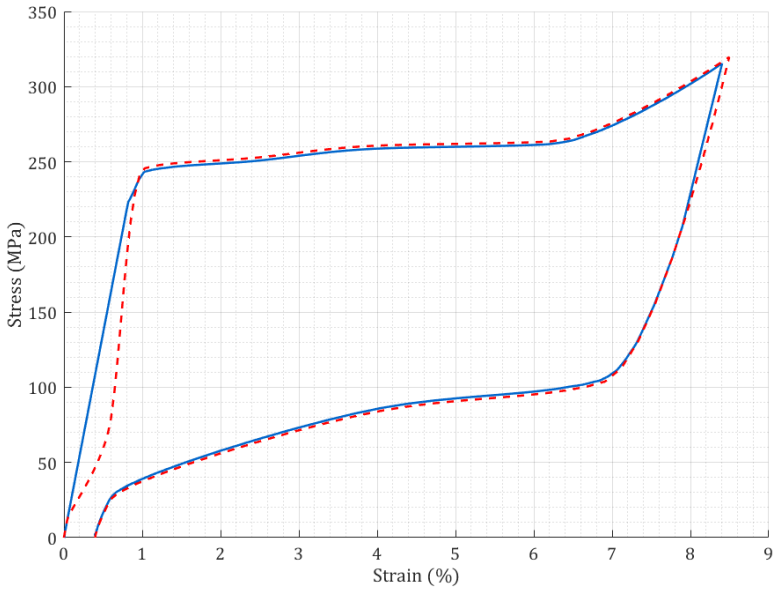

Figure 5-32 - Comparison between experimental curve (red dashed) and simulation result (blue solid), cycle 1

However, it is proven that the concept of effective transformation stress is effective and allows simulating with good confidence also the “leaf-shaped” mechanical behavior conditions without changing the order of the transformation. The transition from the flag–shape to the leave–shape is achieved only by considering that the micromechanical aspects lower the critical transformation stress. This can be applied both to a material with functional fatigue effects and to a material that already present the leaf–shaped cycle because of thermal treatment.

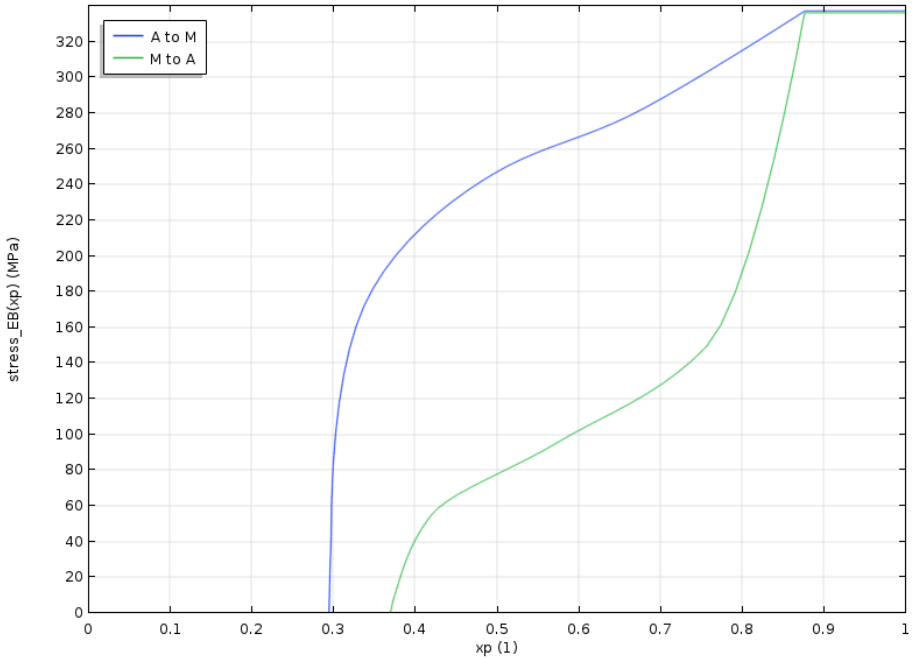

Figure 5-33 - Energy barrier stress as a function of the martensitic fraction, cycle 5

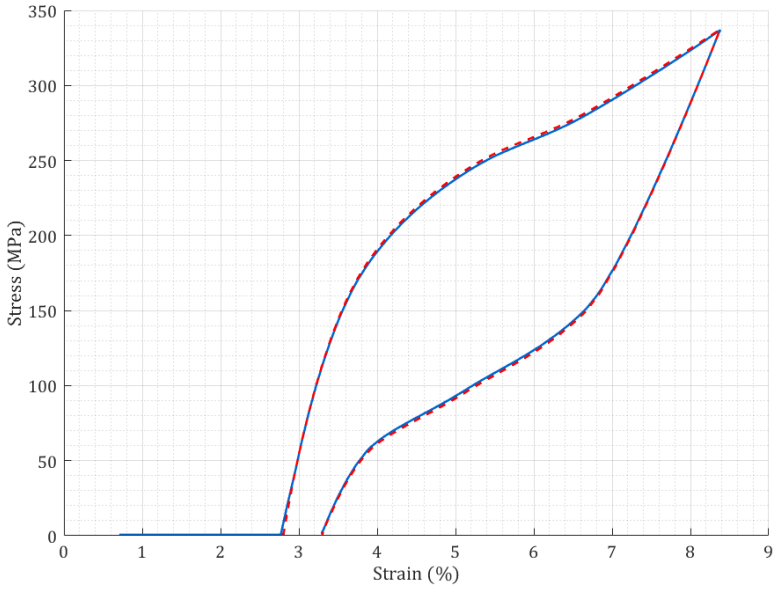

Figure 5-34 - Comparison between experimental curve (red dashed) and simulation result (blue solid), cycle 5

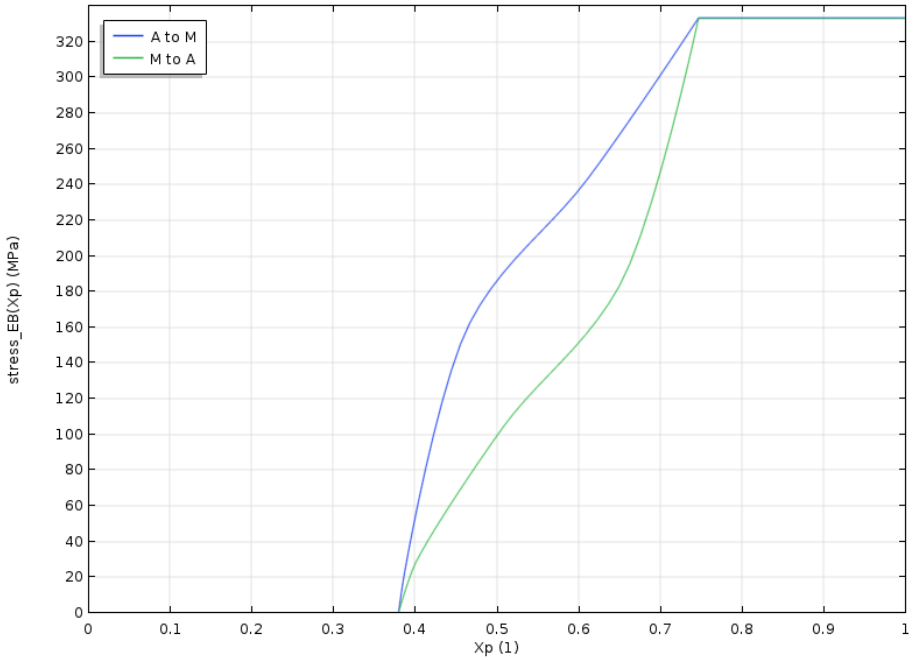

Figure 5-35 - Energy barrier stress as a function of the martensitic fraction, cycle 20

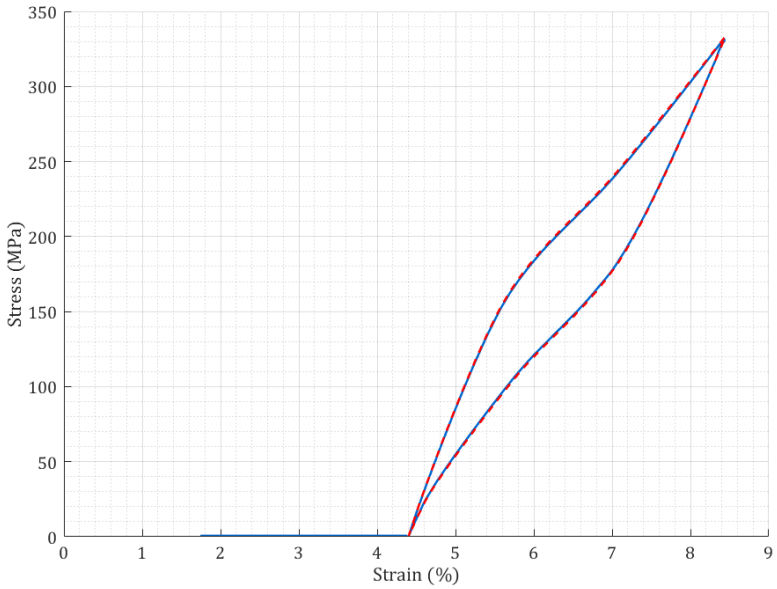

Figure 5-36 - Comparison between experimental curve (red dashed) and simulation result (blue solid), cycle 20

References

Fabrizio M., Pecoraro M., Tibullo V., 2016. A shape memory alloy model by a second order phase transition. Mech. Res. Commun. 74, 20–26. doi:10.1016/j.mechrescom.2016.03.005

Fall M.D., Hubert O., Taillard K.L., Maynadier A., Fall M.D., Hubert O., Taillard K.L., Diffrac- A.M.I.X., 2014. In-situ X-Rays Diffraction and Multiscale Modeling of Shape Memory Alloys To cite this version : HAL Id : hal-01021810.

Hall E.O., 1951. The Deformation and Ageing of Mild Steel: II Characteristics of the Lüders Deformation. Proc. Phys. Soc. Sect. B 64, 742–746.

Heintze O., 2004. A computationally efficient free energy model for shape memory alloys -- experiments and theory.

Heintze O., Seelecke S., 2008. A coupled thermomechanical model for shape memory alloys-From single crystal to polycrystal. Mater. Sci. Eng. A 481–482, 389–394. doi:10.1016/j.msea.2007.08.028

Kim K., Daly S., 2011. Martensite Strain Memory in the Shape Memory Alloy Nickel-Titanium Under Mechanical Cycling. Exp. Mech. 51, 641–652. doi:10.1007/s11340-010-9435-2

Liu Y., Houver I., Xiang H., Bataillard L., Miyazaki S., 1999. Strain dependence of pseudoelastic hysteresis of NiTi. Metall. Trans. A 30, 1275–1282. doi:10.1007/s11661-999-0276-5

Massad J.E., Smith R.C., 2003. A Homogenized Free Energy Model for Hysteresis in Thin- fi lm Shape Memory Alloys. J. Intell. Mater. Syst. Struct. 14, 455–471. doi:10.1177/104538903035235

Polatidis E., Zotov N., Bischoff E., Mittemeijer E.J., 2015. The effect of cyclic tensile loading on the stress-induced transformation mechanism in superelastic NiTi alloys: An in-situ X-ray diffraction study. Scr. Mater. 100, 59–62. doi:10.1016/j.scriptamat.2014.12.013

Sittner P., Liu Y., Novak V., 2005. On the origin of Luders-like deformation of NiTi shape memory alloys. J. Mech. Phys. Solids 53, 1719–1746. doi:10.1016/j.jmps.2005.03.005

Thayer T.A., Bagby M.D., Moore R.N., DeAngelis R.J., 1995. X-ray diffraction of nitinol orthodontic arch wires. Am. J. Orthod. Dentofac. Orthop. 107, 604–612. doi:10.1016/S0889-5406(95)70103-6

Zhigachev A.O., 2013. The effect of specimen surface curvature on x-ray diffraction peak profiles. Rev. Sci. Instrum. 84. doi:10.1063/1.4820444

Chapter 6
ACTUATION OF COMPOSITE SHELL STRUCTURES

Aeronautical research and development is increasingly interested in conceiving structures that can change their shape according to a specific need. For example, this can be the necessity to adapt to different flight conditions for an aerodynamic surfaces or the requirement to boost performance or reduce noise for components of jet engines. In general, for whatever purpose it is applied, the ability of a structure to perform smooth and progressive shape change can be referred as "morphing". Although there is no general agreement on the adjective, as the short for meta-morphose (Barbarino et al., 2011), this term is widely adopted.

The use of morphing –structural or aerodynamic – components can therefore be an alternative to more heavy surfaces control systems already existing that increase weight and fuel consumption. Moreover, morphing concept takes advantage of continuous surfaces, eliminating another source of fuel consumption that is the increased aerodynamic resistance due to discontinuity between wing and mobile surfaces.

A possible classification of morphing structures is according to physical dimension of its action. Large-scale morphing applies to global shape/surface variations, wingspan or camber angle; medium-scale when shape variation affects wing profile (chord, curvature and warping) and small-scale when only local changes are pursued to modify, for example, local aerodynamic flow. Recent reviews have presented a large number of morphing solutions (Sofla et al., 2010). It can also be observed that some are passive solutions, which do not require actuation but own intrinsic properties to adapt their shape to the external aerodynamic condition (Airoldi et al., 2012; Bornengo et al., 2005).

From the structural point of view, three are the basic aspects of the morphing smart system: the internal structure, the external flexible skin and the type of actuation. In addition to the morphing capability, the internal structure and the skin must satisfy a trade-off between adequate load carrying capability and strength and reduced stiffness opposing to the force generated by

actuation system. Therefore, compliance has to be maximized in the direction of shape change, but the system must be able to carry loads in other directions and shape change must be maintained against external forces, which are typically represented by aerodynamic loads.

In light of these considerations, aeronautical research has focused mainly on structural solutions that best meet the just mentioned characteristics. One solution, which appears to be very interesting, is the use of corrugated geometries applied to composite materials, for the design of morphing skins. These structures ensure excellent mechanical characteristics, good deformability, very low weight and the ability to embed actuation systems. This type of solution is under development at the Department of Aerospace Sciences and Technologies of the Polytechnic University of Milan, regarding a project called "morphing sail". The objective is to design and realize a wing able to adapt to the flight condition by varying its profile curvature with the aim of increasing the lifting coefficient. Initially, morphing passive behavior was studied (Airoldi et al., 2015a, 2015b, 2013; Bettini et al., 2010), while actuating SMA wires are now being developed.

6.1 Corrugated composite laminates

A first fundamental component of any type of morphing structure is constituted by the skin, which must collect the aerodynamic loads and transfer them to the main structure. Moreover, an efficient morphing skin may also perform additional structural roles. Such considerations derive from the role of the skin in conventional aircraft stressed-skin constructions. Since morphing applications typically require shape changes only in some directions, a deformable skin with strongly anisotropic characteristic would be able to perform traditional structural roles in non-morphing directions, thus limiting the weight costs derived from the introduction of morphing capabilities in the structure.

Corrugated laminates can be considered promising solutions for supporting a morphing skin, since they are characterized by inherent anisotropy (Fournier, 2012; Thill et al., 2010; Yokozeki et al., 2006). However, they do not provide a smooth and continuous cover and this lead to detrimental effects in the aerodynamic performances, as it has been proved by recent works (Xia et al, 2014).

The concept of corrugated laminate can be extended to geometries that are more complex. In particular, for the project of the "morphing sail", the performance of corrugated geometries characterized by the presence of closed cells is being evaluated. Such geometries can exhibit mechanical properties more elaborate and improved performance than simple corrugates. In addition, the presence of closed cells is of particular interest because it allows the integration of various possible systems in a protected environment such as cables, sensors and actuation systems such as SMAs. This is simply accomplished by joining symmetrically two corrugated and bonding them on the horizontal pieces (twin configuration). The presence of the glue and the constraint between the horizontal pieces increase the stiffness of the structure in the horizontal plane in both directions, in particular in the direction of the chord. This is a limit because requires

greater actuation force, but it is also an advantage contributing to the increase of the flexural rigidity along with the presence of the closed cells.

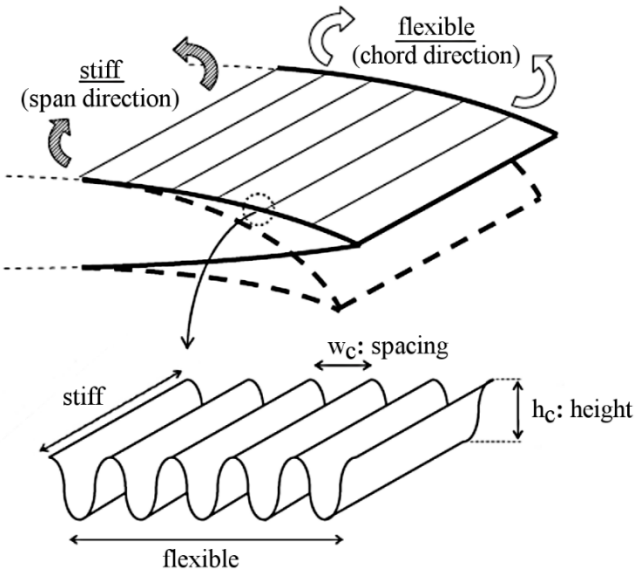

Figure 6-1 - Sketch of a corrugated geometry applied to an aeronautical structure

Some geometries have been presented and analyzed in(Fournier, 2012) and (Guaita, 2015). In particular, work has been focused on two geometries: a squared (Figure 6-2) and a trapezoidal (Figure 6-3). For the twin configuration both symmetric and non-symmetric solutions have been considered, obtained coupling respectively equal or different geometries for top and bottom corrugated (Figure 6-4).

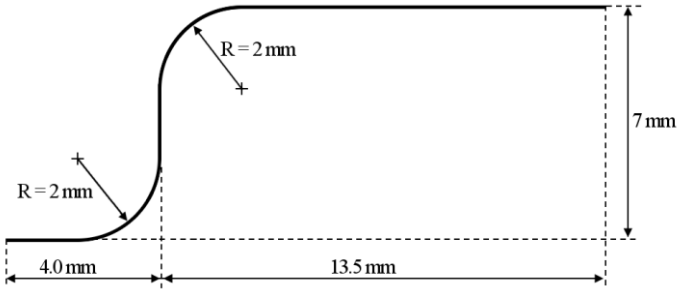

Figure 6-2 - Squared geometry of the corrugated laminate. Half-cell length, single configuration.

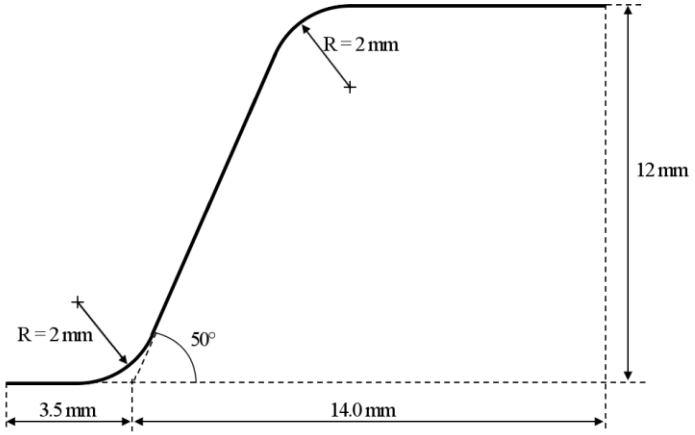

Figure 6-3 - Trapezoidal geometry of the corrugated laminate. Half-cell length, single configuration.

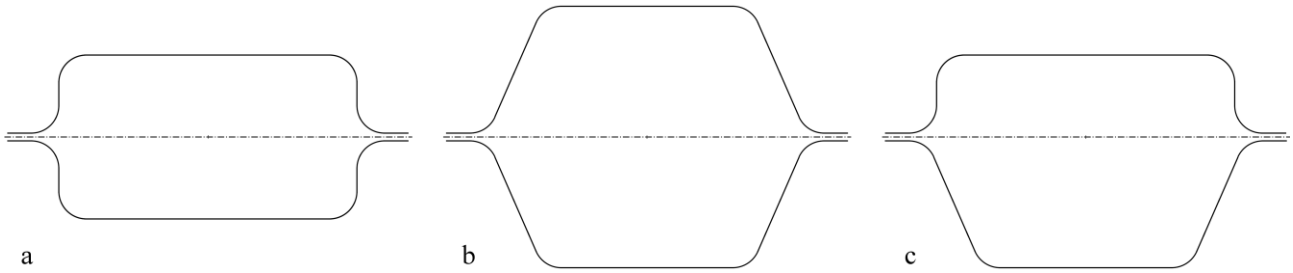

Figure 6-4 - Twin configurations, Single cell.
a) Symmetric squared, b) Symmetric trapezoidal, c) Non-symmetric mixed.

Figure 6-5 - Corrugated panel on the aluminum mold. Example of squared geometry.

Two different materials are used to realize laminate corrugate: carbon– and glass– fiber reinforced polymers (CFRP and GFRP). Both are fabric (FB) and are stacked with orientation 0/90°. The number of plies of the laminates (in the case of NiTi implementation) is two or three. The material properties of the single ply are listed in Table 6-1.

Table 6-1 - List of material parameters

Property	Symbol	CFRP FB	GFRP FB
Young Modulus	$E_{xx} = E_{yy}$	60 GPa	20 GPa
	E_{zz}	10 GPa	10 GPa
Shear Modulus	$G_{xy} = G_{xz} = G_{yz}$	4 GPa	4 GPa
Poisson's Ratio	ν_{xy}	0.05	0.1
	$\nu_{xz} = \nu_{yz}$	0.3	0.3
Density	ρ	1.705 kg/m^3	2.54 kg/m^3
Thickness of one ply	t	0.2 mm	0.2 mm

In this chapter, only the trapezoidal geometry in symmetric twin configuration is considered (Figure 6-6), with the wires embedded in the symmetry plane. Six cells are considered and then the total length of the corrugated laminate results 210 mm, which corresponds to the mounting length of the SMA wires.

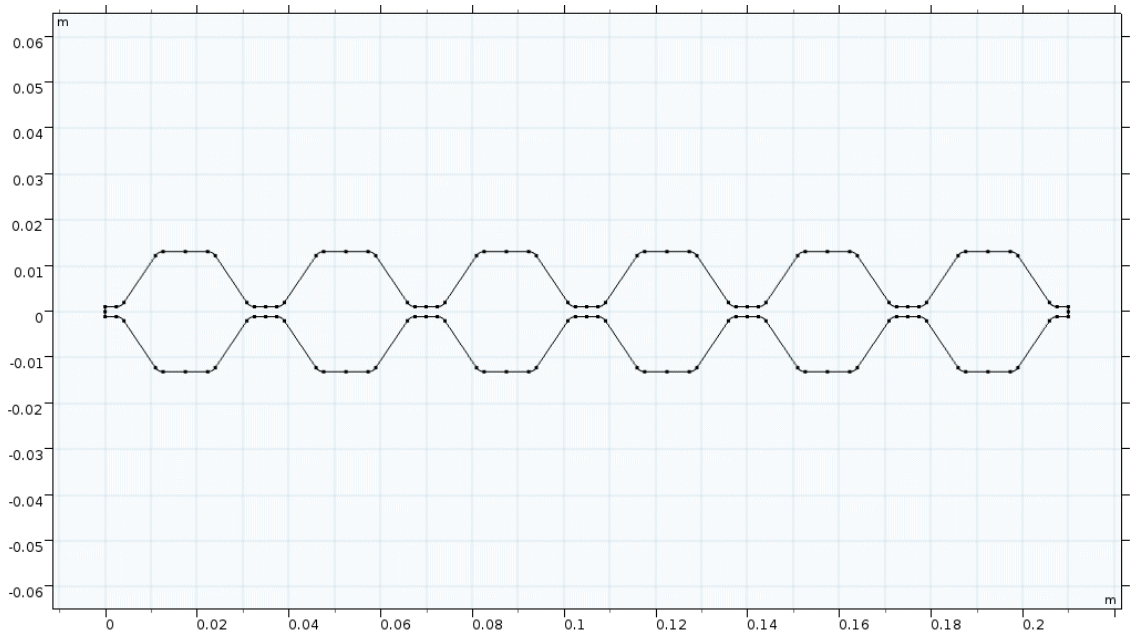

Figure 6-6 - Sketch of the work plane on which the geometry of the twin corrugated laminate with trapezoidal geometry is drawn

6.2 Numbers of wires

To obtain the number of wires needed to pull the corrugated twin laminate, the procedure described in (Concilio and Lecce, 2014) has been applied. This graphic method consists in drawing the mechanical cycles of the SMA wire at ambient (rearm) and high (actuation) temperature and then overlaying the linear curve corresponding to the stiffness of the compliant structure, as if it is a spring opposing to the SMA in series.

Through a sweep on the force applied to a side of the corrugated, the displacement in the direction of the wires is calculated. This serves to obtain the stiffness of the structure and then the linear coefficient to be overlaid to the SMA characteristic curves. The resulting stiffness is 52.1 kN/m.

The SMA wires considered for this application are the same SmartFflex NiTi wires used for the calibration of the model in Chapter 2. Their mechanical behavior at different temperatures is known experimentally only up to 115°C. Since the maximum stroke/force expressed by the SMA actuator is obtained when the stiffness line intersect the elastic part of the high–temperature curve, the elastic part of the curve at 115°C is used. The force of the parallel wires is the sum of the forces of the single wires, and then the number of wires to be used can be evaluated multiplying the force of the characteristic curves by the number of wires, which gives intersections with the stiffness line.

Considering a 5% mounting pre–strain and a 210 mm mounting deformed length, the Austenitic length of wire when cut results 200 mm and the mounting displacement 10 mm.

Figure 6-7 shows the result of the graphic method applied with 24 wires. The foreseen stroke is 5.4 mm and the total force 281.42 N corresponding to 11.7 N for each wire.

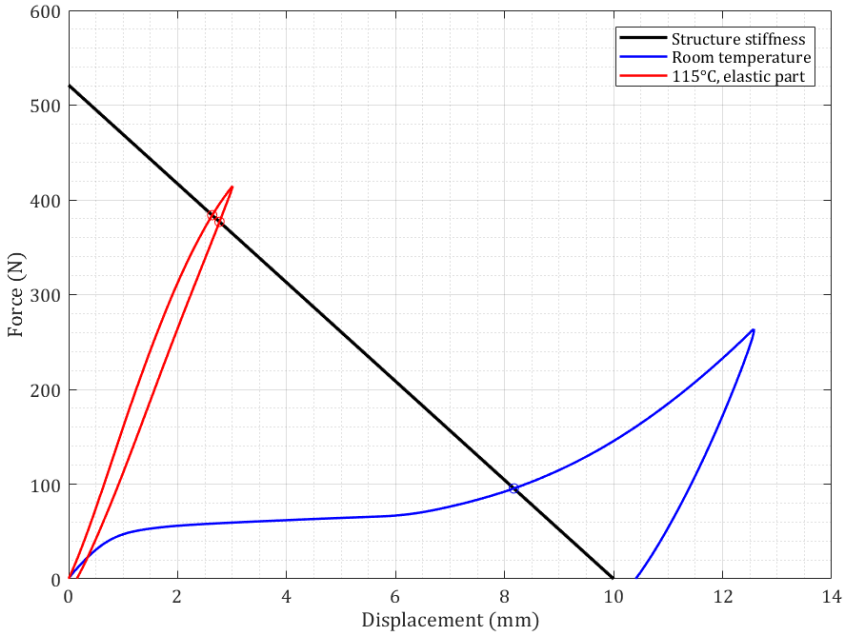

Figure 6-7 - Graphic method to evaluate force and stroke of a SMA wire acting against a structure.

6.3 COMSOL model

The geometry of the configuration A as modeled in COMSOL is given below. The width of the corrugated laminate is 300 mm. Since the designed number of wires is 24, then the geometry is extruded in the y-direction by 12.5 mm.

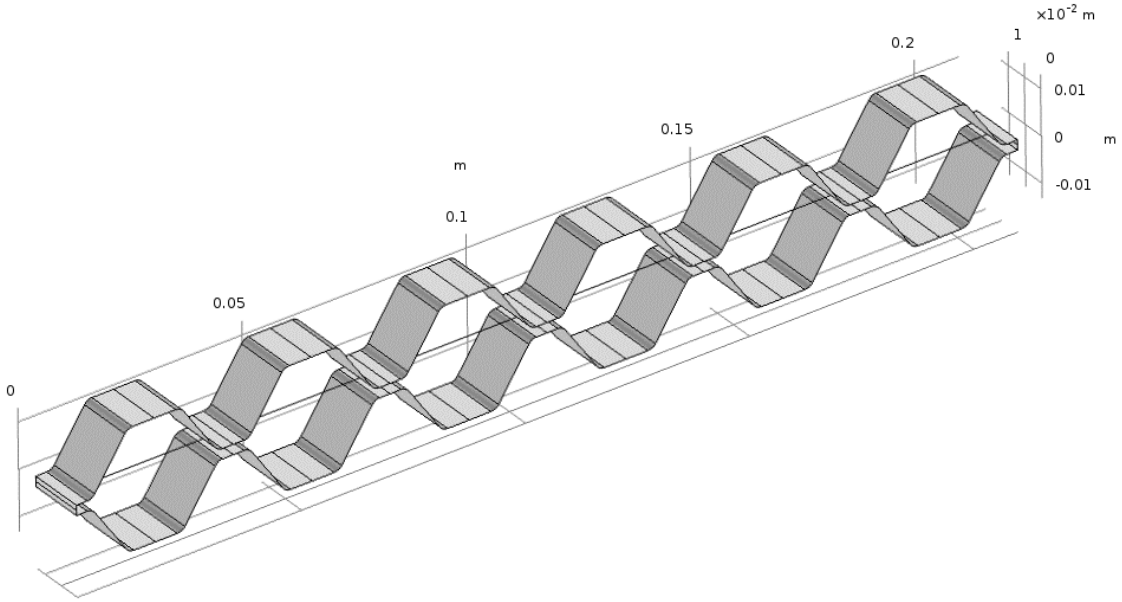

Figure 6-8 - Extruded 3D geometry of the corrugated laminate

The anisotropic material is applied in COMSOL defining directly its elasticity matrix. The laminate is composed by two CFRP fabric plies stacked with 0°/90° angles. The elasticity matrix, Q, of the laminate is computed using Classical Laminated Plate Theory and results:

$$Q = 1.0e{+}04 * \begin{vmatrix} 2.4365 & 0.1218 & 0 & 0 & 0 & 0 \\ 0.1218 & 0.4061 & 0 & 0 & 0 & 0 \\ 0 & 0 & 0.16 & 0 & 0 & 0 \\ 0 & 0 & 0 & 0.0325 & 0.0016 & 0 \\ 0 & 0 & 0 & 0.0016 & 0.0054 & 0 \\ 0 & 0 & 0 & 0 & 0 & 0.0021 \end{vmatrix}$$

Shell Interface is used to model the corrugated laminate. The Shell interface is used to model structural shells on 3D boundaries and the interface uses shell elements of the MITC type, which can be used for analyzing both thin (Kirchhoff theory) and thick (Mindlin theory) shells. The thickness of the shell element is the one of two plies (0.4 mm). To allow joining the wire in the middle plane to the structure, the composite properties are applied also to two vertical sides at the extremes of the corrugated.

The glue bounding the two sides of the twin laminate is not modeled. Instead, an identity on the boundary is applied to the surfaces in the grooves of the corrugated.

The SMA wire is modeled applying the procedure described in Chapter 3, but extended to the 3D case. A noticeable difference is that in this case a truss cannot be used to model the wire, because no connection between trusses and shells is possible in Comsol. The multiphysics implemented in version 5.3 allows directly couple shell and beams instead and then a beam is used to represent the wire. Another difference is that the model used in Chapter 3 was a single–crystal model. Here, instead, a parametric approach is used assuming as transformation stress the value derived from the characterization experimental curves and values presented in Chapter 2.

The extremes of the corrugated laminate are constrained with a Pin boundary condition on the left side and with a simply support on the right side. The y and z displacements along the edges are also constrained to avoid instability.

Figure 6-9 shows the deformed geometry of the structure. The contour reports the displacement of the nodes. The maximum displacement obtained at the free end is 9.1 mm, which is even higher than the 5.3 mm stroke designed, whilst the temperature reaches 120°C. In Figure 6-10 the strain distribution is reported, showing the concentration of deformation in the bounded areas.

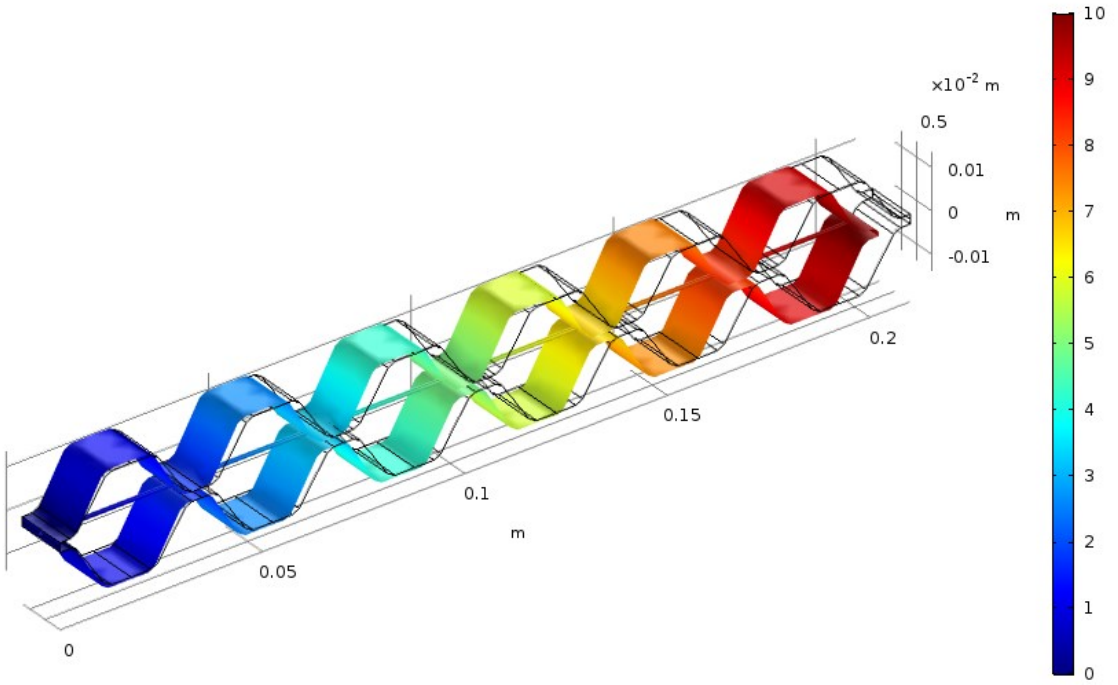

Figure 6-9 - Displacement distribution on the geometry

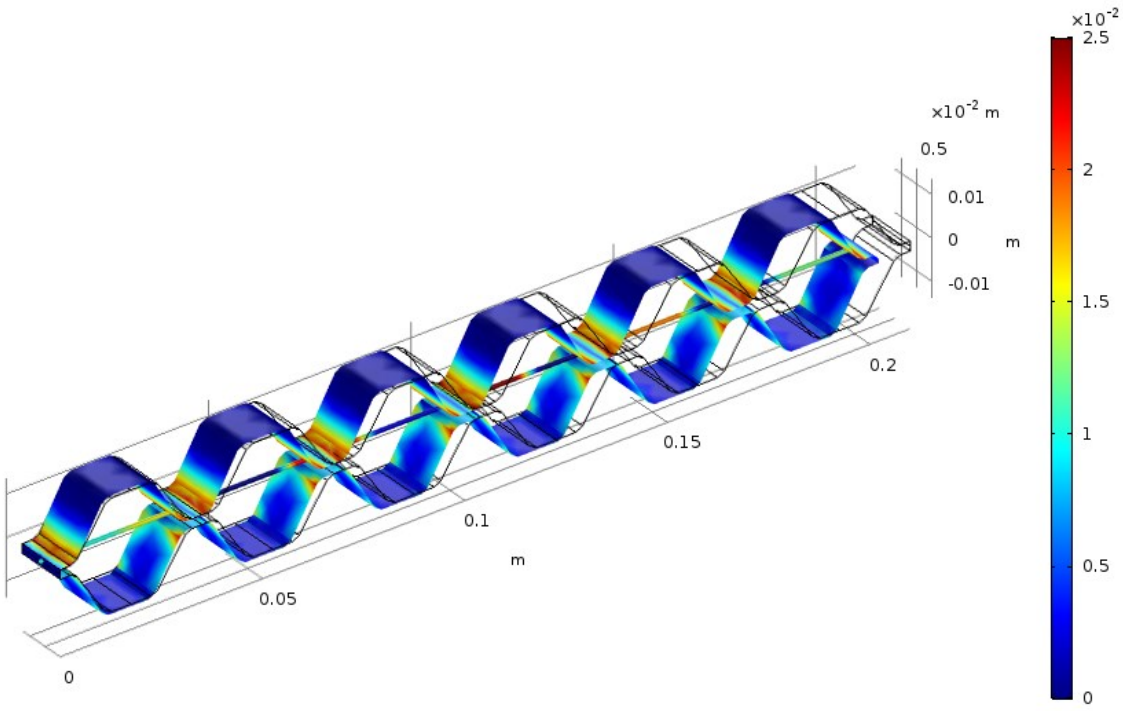

Figure 6-10 - Strain distribution on the geometry

In Figure 6-11 and Figure 6-12, the stress distribution can be seen. In the first figure the distribution in the whole geometry and in the second, the time–dependent stress in the points of the middle cell. The legend of the points of a cell on which stress is evaluated can be found in Figure 6-13. The maximum value reached within the composite is 50 MPa and is concentrated in the bounded areas.

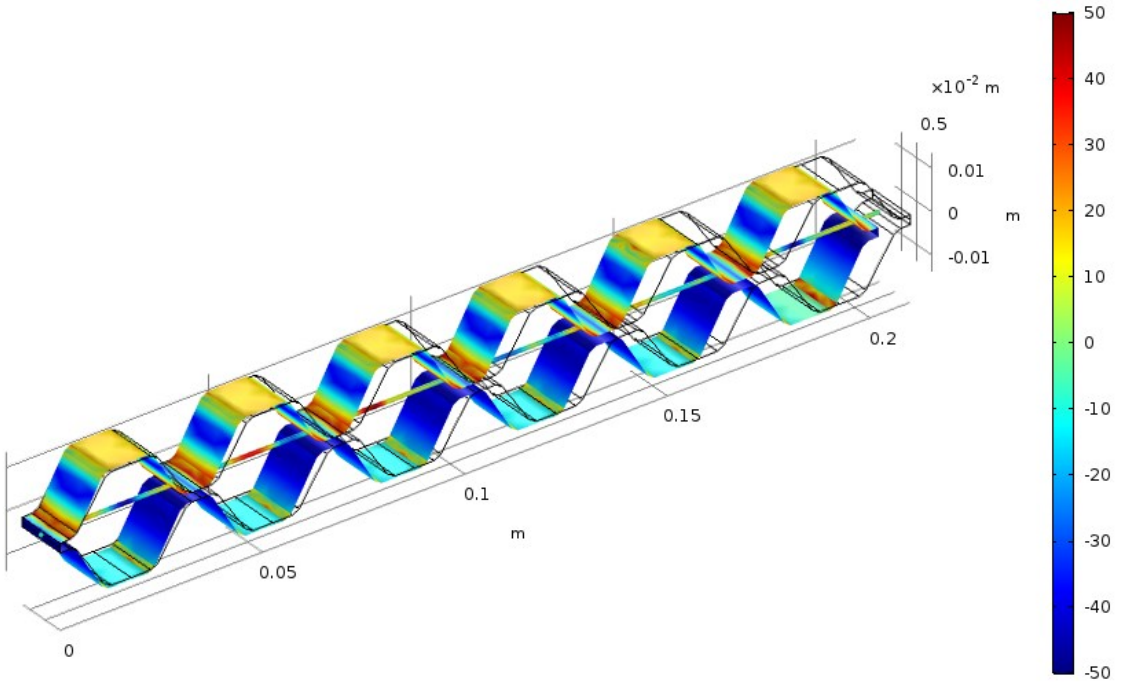

Figure 6-11 - Stress distribution on the geometry

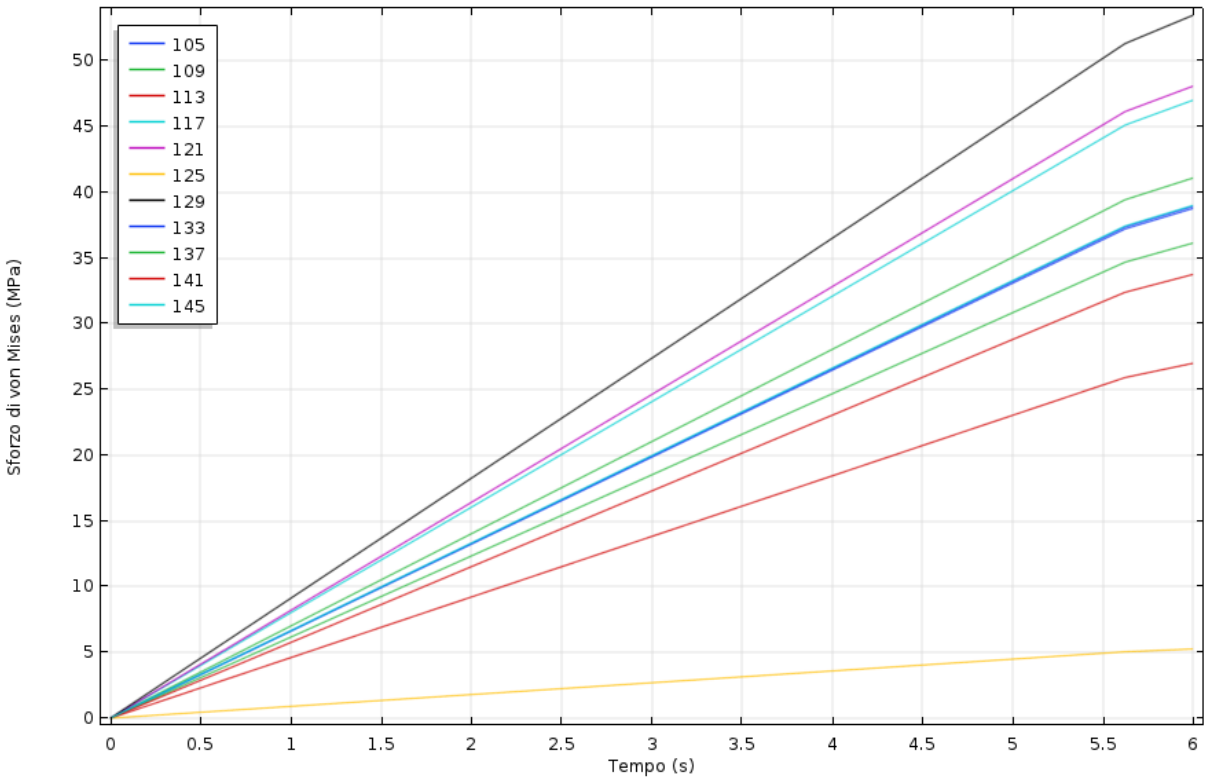

Figure 6-12 - Stress on the points of a cell

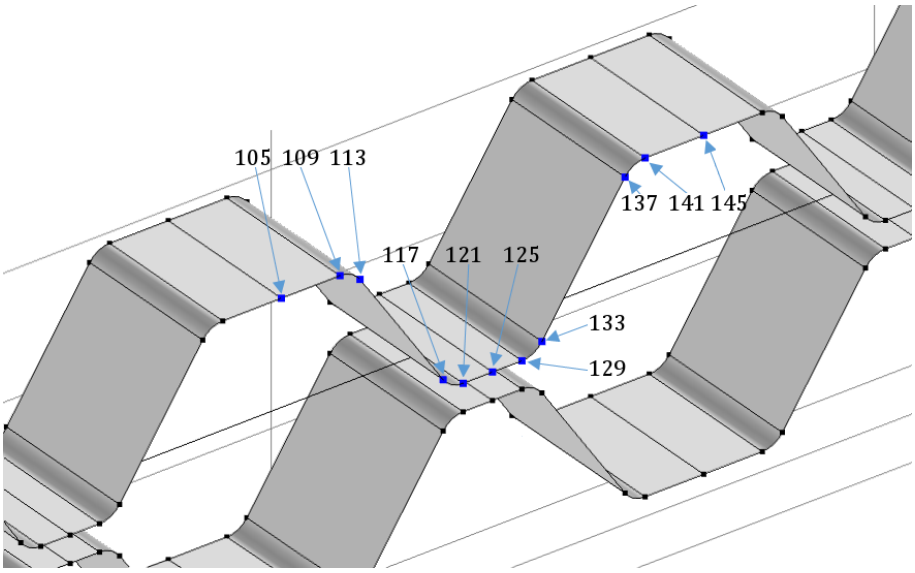

Figure 6-13 - Legend of the points of a cell on which stress is evaluated

From the SmartFlex brochure (SAES Group, n.d.), the reduction in stress–strain characteristics of the wire is known (Figure 6-14). Assuming a 1 % residual strain and a supposed retained martensitic fraction equal to the 10%, the strategy adopted in Chapter 5 is used to evaluate the loss in the performances of the actuator with cycling.

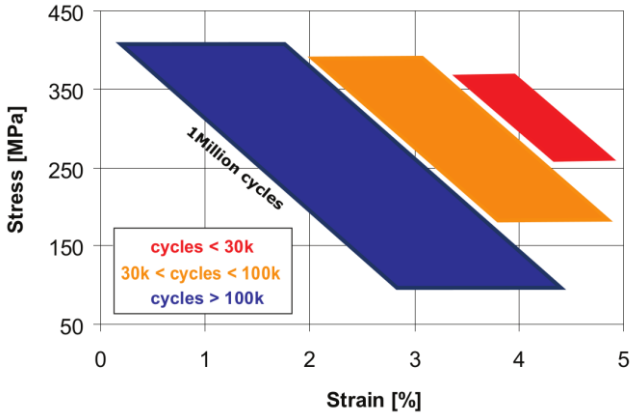

Figure 6-14 - Reduction in stress–strain characteristics of the wire with cycling

Figure 6-15 and Figure 6-16 show the deformed geometry of the structure with these modifications, with the contours of displacement and stress, respectively. The maximum displacement obtained at the free end is now reduced to 6.8 mm with respect to the previous displacement and the stress distribution also reduced.

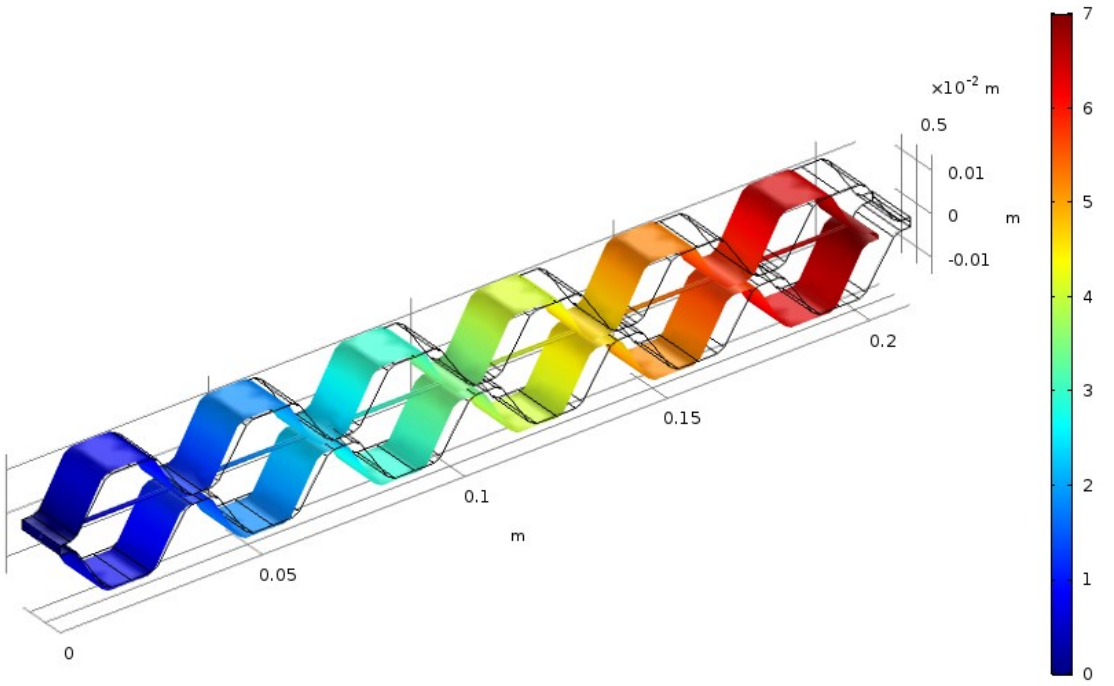

Figure 6-15 - Displacement distribution on the geometry

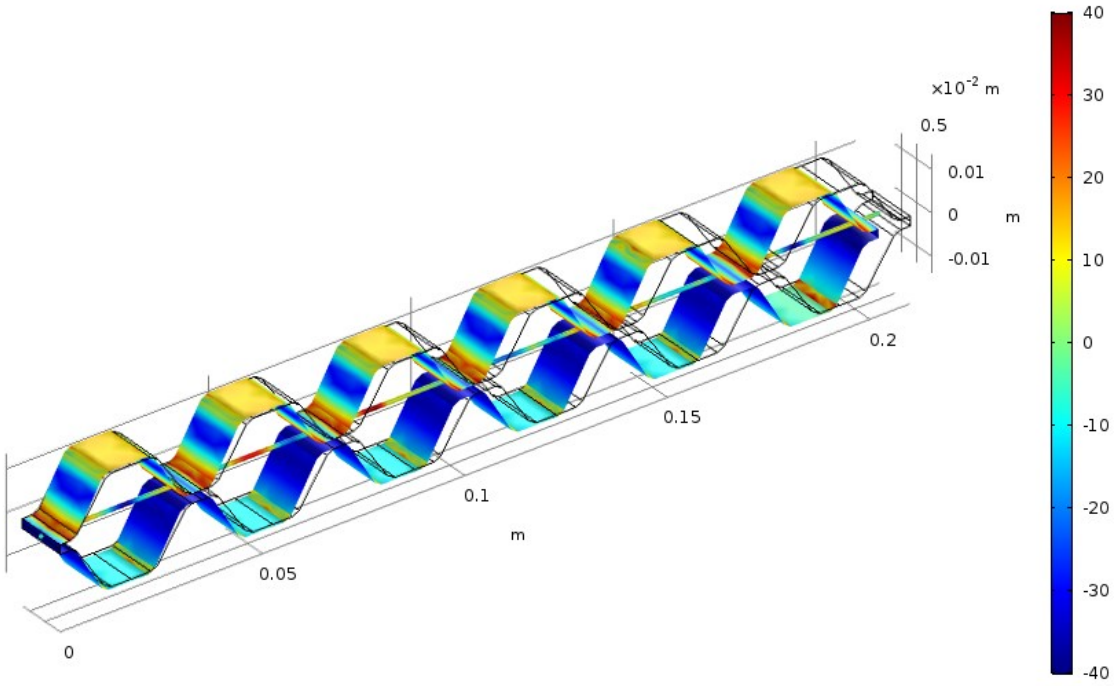

Figure 6-16 - Stress distribution on the geometry

References

Airoldi A., Bertoli S., Lanzi L., Sirna M., Sala G., 2012. Design of a motorcycle composite swing-arm by means of multi-objective optimisation. Appl. Compos. Mater. 19, 599–618. doi:10.1007/s10443-011-9227-6

Airoldi A., Bettini P., Panichelli P., Oktem M.F., Sala G., 2015a. Chiral topologies for composite morphing structures – Part I: Development of a chiral rib for deformable airfoils. Phys. Status Solidi Basic Res. 252, 1435–1445. doi:10.1002/pssb.201451689

Airoldi A., Bettini P., Panichelli P., Sala G., 2015b. Chiral topologies for composite morphing structures – Part II: Novel configurations and technological processes. Phys. Status Solidi Basic Res. 252, 1446–1454. doi:10.1002/pssb.201584263

Airoldi A., Quaranta G., Beltramin A., Sala G., 2013. Design of a Morphing Actuated Aileron With Chiral Composite Internal Structure. 6th ECCOMAS Conf. Smart Struct. Mater. 1, 24–26. doi:10.2514/1.C031486

Barbarino S., Bilgen O., Ajaj R.M., Friswell M.I., Inman D.J., 2011. A Review of Morphing Aircraft. J. Intell. Mater. Syst. Struct. 22, 823–877. doi:10.1177/1045389X11414084

Bettini P., Airoldi A., Sala G., Landro L. Di, Ruzzene M., Spadoni A., 2010. Composite chiral structures for morphing airfoils: Numerical analyses and development of a manufacturing process. Compos. Part B Eng. 41, 133–147. doi:10.1016/j.compositesb.2009.10.005

Bornengo D., Scarpa F., Remillat C., 2005. Evaluation of hexagonal chiral structure for morphing airfoil concept. Proc. Inst. Mech. Eng. Part G J. Aerosp. Eng. 219, 185–192. doi:10.1243/095441005X30216

Concilio A., Lecce L., 2014. Shape Memory Alloy Engineering: For Aerospace, Structural and Biomedical Applications. Elsevier Ltd. doi:10.1016/C2012-0-07151-7

Fournier S., 2012. Flexible Composite Frames for Morphing Structural Skins. Politecnico di Milano.

Guaita L., 2015. Attuazione di pannelli corrugati in composito con leghe a memoria di forma. Politecnico di Milano.

SAES Group, n.d. SmartFlex® Wire [Brochure]. Published by SAES Group. Printed in Italy. Retrieved from www.saesgroup.com

Sofla A.Y.N., Meguid S.A., Tan K.T., Yeo W.K., 2010. Shape Morphing of Aircraft Wings: Status and challenges. Mater. Des. doi:10.1016/j.matdes.2009.09.011

Thill C., Etches J.A., Bond I.P., Potter K.D., Weaver P.M., 2010. Composite corrugated structures for morphing wing skin applications. Smart Mater. Struct. 19, 124009. doi:10.1088/0964-1726/19/12/124009

Yokozeki T., Takeda S. ichi, Ogasawara T., Ishikawa T., 2006. Mechanical properties of corrugated composites for candidate materials of flexible wing structures. Compos. Part A Appl. Sci. Manuf. 37, 1578–1586. doi:10.1016/j.compositesa.2005.10.015

CONCLUSIONS

Objective of the PhD project was the improvement of a constitutive model to take into account the consequence of microstructural aspects on the mechanical behavior of a SMA actuator. This in terms both of functional fatigue and of tailoring of the characteristics through thermal treatment. Since the microstructural aspects involve very complex aspects of the material, the aim was to introduce the effect by specifying specific phenomenological parameters of a constitutive model.

Starting from the fundamental concepts regarding SMA historical background, material properties, and applications, the work moved on from a literature review on shape memory alloy constitutive modeling, in order to prepare the framework for the following study. From the literature review, three models were chosen to be probed, each interesting for different peculiarities. The first model selected is based on (Tanaka, 1986), modified using a sigmoidal function as transformation kinetics law; the second model considered is the well-known (Boyd and Lagoudas, 1996) macroscopic free energy model; the last model is also a free-energy model developed by Müller and Seelecke (2001). These models are calibrated and then validated on the experimental results of a uniaxial tensile test. Then, a qualitative comparison between the same models was based on more complex applications. The first model (Tanaka modified) was used to study the parallel system of NiTi pseudoelastic wires, developed in collaboration with CNR-ICMATE, to analyze the possibility of tailoring the absorbed mechanical energy, coupling different types of wires. The second one (Lagoudas phenomenological) was applied to the case of a device designed to shrink radially a compliant silicone pipe, by means of a single shape-memory NiTi wire bounded on its circumference. The last one (MAS model) was used to simulate a linear actuator consisting of a SMA wire bending a flexible beam to which is externally constrained with stiff aluminum stubs. This comparison lead to the selection of the third model as a constitutive basis, in the following referred with the acronym MAS. This model was used both in its Single Crystal formulation and in the Polycrystalline one, with the use of the concept of Effective Barrier Stress and Representative Crystal.

Because of the importance of experimental characterization in SMA wires, this was conducted on a typical SMA commercial wire for actuation, with the aim to calibrate some fundamental parameters of the MAS model. A detailed description an analysis was presented to define also to the recommended procedures for thermomechanical characterization. A significant parameter of the Polycrystalline parametric version of the MAS model is the Effective Barrier Stress and its dependence from the martensitic fraction. Then, the measurement of the transformation-triggering stress as a function of the fractional volume of martensite in different microstructural conditions is obtained thanks to in situ X-ray diffraction experiment performed during mechanical cycling. These experiments allowed investigating the effects of microstructural changes on the stress-induced phase transition mechanism in polycrystalline NiTi and then modifying the expression of the strain to take into account the retained martensitic fraction accumulating during cycling

Finally, the results of this characterization are used to simulate an aerospace application that consists in the use of SMA as actuators for an aerodynamic morphing skin based on corrugated shell geometries made by composite materials. This is simulated in two conditions of the wire one representing the properties at begin of life and the other after some cycles of shape modification, comparing the loss of performance.

ACKNOWLEDGEMENTS

I was in doubt if writing the acknowledgement section, but several people truly deserve to be thanked as they have sustained me during these years through their experience or support.

Firstly, I express my gratitude to my advisors, Prof. Giuseppe Sala and Dr. Elena Villa who gave me the opportunity to take up this path and reach this goal.

I am particularly grateful also to Prof. Stefan Seelecke for the edifying and fruitful experience I've lived in Saarbrücken and for the precious scientific discussions in the complex field of shape memory alloys.

I also wish to thank all Professors of the doctoral courses I've attended – Prof. Brunella, Prof. Miccoli, Prof. Matricciani and Prof. Tommasini – for their valuable teachings, both academic and personal: I have really learned a lot from their professional experience offered with genuine enthusiasm.

I sincerely thank Enrico and Giordano, who have patiently endured my difficulties and have provided their valuable and competent advice, so contributing to the XRD experimental part of this thesis.

Many thanks to my colleagues of the doctoral program at DAST, Alessia fistly. Chatting with them and finding in them the same troubles as mine, made me feel less misfit. Moreover, sometimes it's good to get distracted. Heartfelt thanks to Filomena and Gianluca who made me feel welcomed and at home in a foreign land.

My thanks also go to my mother, who always worries too much for me, but also always reminds me of the sight of who I have lost watching over me.

I thank Paolo with immense gratitude for having involved me in his activities as a professor and researcher. He gave me the chance to learn more than a lot, always showing the "human side of Polimi", with his thoughtful support and interest in my personal situation and uncertainty about the future, which have been immensely valuable to me.

Finally yet importantly, I would like to thank Carlo for his understanding, endless patience, encouragement and scientific... quarrel. He is my tower of strength and if I falter, he will sustain me. I know that this tenacious cliff will never fall.

A special thank goes also to Jennifer Walker. In the darkest moment, throwing the heart in the web, I found someone who I will never know, but who offered me the words to understand that I could handle this too. «It's common knowledge that getting a PhD is hard. It's meant to be. Some even say that if you're not up all night working or skipping meals, you're doing it wrong. But while PhD students are not so naive as to enter the program expecting an easy ride, there is a cost to the endeavor that no one talks about: a psychological one.» There's indeed an awful cost to getting a PhD. Candidates are not warned about the pressure, insecurity and loneliness that you can feel on the way. No one would be able to complete this journey alone and, fortunately, no one has to.